An Investigation of Immature Rib Fractures Resultant from both CPR and Abusive Scenarios

A thesis submitted to the University of Manchester for the degree of Doctor of Philosophy in the Faculty of Engineering and Physical Sciences

2014

Mark R. Johnson

School of Materials

Table of Contents

List of Figures....5
Index of Tables....9
Abstract....10
Declaration....11
Copyright Statement....11
Acknowledgements....12
1 Introduction....14
1.1 The Objectives of the Study....16
1.2 Thesis Structure....17
2 Literature Review....18
2.1 The Language of Anatomy for Humans and Quadrupeds....18
2.2 Bone Structure....21
2.2.1 Types of Bone....21
2.3 The Structure and Mechanical Behaviour of the Human Skeleton....25
2.3.1 Human Skeletal System....25
2.3.2 Human Thoracic Skeleton....25
2.3.3 Human Ribs....26
2.3.4 Human Sternum....27
2.3.5 Articulations of the ribs....28
2.3.6 Differences to the Infant Thorax....30
2.4 Diseases that can Effect or Influence the Structure, Mechanical Behaviour and Strength of Bones....32
2.5 Selection of a Suitable Surrogate Animal....34
2.6 Forces and Damage Inflicted on the Body During Infant CPR....38
2.7 Forces and Damage Associated with Abuse....42
2.8 Techniques: X-ray Radiograpy, X-ray Tomography, Nanoindentation, and FEA....47
3 Materials and Methods....54
3.1 Objective of the experiments....54
3.2 Test Programme to Model the Loads Associated with CPR and Abuse on Infants...55
3.2.1 Limitations and constraints of the experiment....55
3.3 The Load Rig and the Application of Loads to the Test Specimens....56
3.3.1 Choice of actuator....56
3.3.2 Concept for Rig....57
3.3.3 The Build....57
3.3.3.1 Upper Section....58
3.3.3.2 Bottom section....60
3.3.4 CPR Test Setup and Loading Regime....61
3.3.5 Abusive Squeezing Test Setup and Loading Regime....62
3.4 The Test Specimens....64
3.4.1 Piglet Rib Cage Assessment....64
3.5 X-Ray Radiography and Micro Tomography of the Specimens....66
3.5.1 Piglet Thoraxes Pre and Post Mechanical Testing....66
3.5.2 Piglet Thorax XMT Reconstruction and Data Conversion....67
3.6 Protocol for Classification of Fractures....68
3.6.1 Radiograph Assessment....68
3.6.2 X-ray Microtomography Assessment....68
3.7 Rib Bone Mechanical Behaviour....70
3.7.1 Mature Pig Ribs....70
3.7.1.1 Specimens....70
3.7.1.2 Mature Rib Tomography & Reconstruction....70
3.7.1.3 Mature Rib Mechanical Testing....71
3.7.1.4 Nanoindentation....71

3.7.2 Immature Piglet Ribs....72
3.7.2.1 Specimens....72
3.7.2.2 Sample Preparation....72
3.7.2.3 5mm Sections for Compression Tests....72
3.7.2.4 Full Ribs for Anterior-Posterior Loading....72
3.7.2.5 Immature Rib Tomography & Reconstruction....72
3.7.2.6 Nanoindentation....72
3.7.2.7 Mechanical Testing....73
3.8 FE Modelling....74
3.8.1 Mature Pig Rib....74
3.8.1.1 FE Model Generation....74
3.8.1.2 FE Analysis....74
3.8.1.3 Sensitivity Analysis of Model to Meshing....76
3.8.2 Immature Piglet Rib....77
3.8.2.1 FE model generation....77
3.8.2.2 FE analysis....77
4 Results of the Experiments....79
4.1 Load Testing Results of Piglet Thoracic Cages....79
4.1.1 CPR Scenario....79
4.1.2 Summary of CPR Mechanical Tests on Piglets....85
4.1.3 Abusive Scenario....86
4.1.4 Summary of Abusive Mechanical Tests on Piglets....92
4.2 Classification of Fractures Using X-ray Radiography and Tomography....94
4.2.1 Summary of CPR Related Fractures Identified with Radiography....94
4.2.2 CT Scan Assessment Following CPR Scenario....95
4.2.3 Summary of CPR Related Fractures Identified with CT scans....99
4.2.4 Summary of Abuse Related Fractures Identified with Radiography....100
4.2.5 CT Scan Assessment Following Abusive Scenario....101
4.2.6 Summary of Abuse Related Fractures Identified with CT scans....107
4.2.7 3D Visualisation of Ribs From CT Scan Data....108
4.3 Rib Bone Mechanical Behaviour....110
4.3.1 Mature Pig Ribs....110
4.3.1.1 Tomography....110
4.3.1.2 Mechanical Testing....110
4.3.1.3 Nanoindentation....111
4.3.2 Immature Piglet Ribs....113
4.3.2.1 Tomography....113
4.3.2.2 Mechanical Testing....113
4.3.2.3 Nanoindentation....114
4.3.2.4 Radiography Following Mechanical Testing....115
4.4 FE Modelling....116
4.4.1 Mature Pig Ribs....116
4.4.1.1 Finite Element mesh for mature bone section....116
4.4.1.2 Finite Element simulations for mature bone section....116
4.4.2 Meshing Sensitivity Analysis for Mature Bone Section....118
4.4.3 Immature Piglet Ribs....121
5 Discussion....122
5.1 Thorax Tests....123
5.1.1 CPR....123
5.1.1.1 Individual Assessment of Thoraxes Receiving Simulated CPR....123
5.1.1.2 Collective Assessment of Thoraxes Receiving Simulated CPR....124
5.1.1.3 Conclusions from Thoraxes Receiving Simulated CPR....126
5.1.2 Abuse....127

5.1.2.1 Individual Assessment of Abusively Squeezed Thoraxes....127
5.1.2.2 Collective Assessment of Abusively Squeezed Thoraxes....130
5.1.2.3 Conclusions from Abusively Squeezed Thoraxes....131
5.1.3 Comparison between CPR and abusive squeezing scenarios....133
5.2 Rib Bone Mechanical Behaviour....134
5.2.1 Cross sectional pieces....134
5.2.2 Individual rib tests....136
5.3 FE Modelling....137
5.3.1 Rib cross sections....137
5.3.2 Isolated individual ribs....140
5.4 Critical discussion of testing methods....141
5.4.1 Use of surrogate animal....141
5.4.2 Testing method....141
5.4.3 Radiography and CT fracture characterisation....142
6 Conclusions....143
7 References....145

List of Figures

Figure 1. The anatomical position (a) and anatomic terminology describing body orientation and direction (b) 18
Figure 2: Anatomic terminology describing body orientation and direction of four-legged animal 19
Figure 3. Planes of the body http://commons.wikimedia.org/wiki/File:Human_anatomy_planes.svg (Accessed 15/09/2013).....20
Figure 4. Types of bone tissue on the macroscopic scale (A) cortical bone (B) cancellous bone.....21
Figure 5. The hierarchical arrangement of bone.....24
Figure 6. The Axial and Appendicular Skeleton (OpenStax College, 2013).....25
Figure 7: The human thoracic cage (Gray's Anatomy).....26
Figure 8: The geometry and landmarks of a "typical"rib (a) and the landmarks and features of the posterior extremity of a 'typical' rib (b) (Gray's Anatomy).....27
Figure 9. The human sternum (a) anterior view (b) left lateral aspect.....28
Figure 10: Posterior rib articulation with thoracic vertebrae (a) oblique aspect (b) superior aspect.....28
Figure 11. Anterior rib articulation with sternum (Gray's Anatomy).....29
Figure 12. Development of the infant skeleton (a) The infant skeleton, light blue areas are cartilaginous (b) ossification of the sternum.....31
Figure 13. Fetal pig skeletal system.....35
Figure 14. Transverse plane cross-section of 20-25 kg pig (Steen et al., 2002) (a) uncompressed anteroposterior diameter ~ 19.5 cm (b) simulated chest compression 36
Figure 15. Cross-sectional drawing of the adult human and adult pig thorax (Adapted from Huelke et al., 1986).....36
Figure 16. Infant CPR showing the two-finger technique (a) and the revised recommendation for CPR using two thumbs (b) (Images from Matshes and Lew, 2010)...39
Figure 17. Chest compression during two-thumb CPR (Images from Matshes and Lew, 2010).....39
Figure 18. Typical fracture sites in the infant thorax following abusive anteroposterior compression (Kleinman, 1998).....44
Figure 19. Anterior grip of an infant in abusive squeezing (a) and the posterior grip of an infant in abusive squeezing (b) (Images from Matshes and Lew, 2010).....45
Figure 20. X-ray microtomography experimental setup.....48
Figure 21. Characteristic load-displacement curve for nanoindentation. Adapted from (Oliver and Pharr, 1992).....49
Figure 22. Instron® 5569 schematic.....57
Figure 23. Schematic image of the rig used in the tests to simulate the forces on the ribs due to CPR (A) and abusive squeezing (B). The commissioned load rig with dummy infant inserted is shown in (C) and (D).....58
Figure 24. Plastic knob dimensions (http://uk.rs-online.com/web/p/knobs/2670825/).....59
Figure 25. Upper section of test rig for coupling to load cell of Instron.....59
Figure 26. Demonstration of range of motion for plastic "thumbs" when attached adapter for load cell coupling 60
Figure 27. Plastic knob position for CPR scenario.....61
Figure 28. Diagram of displacement amplitude against time for CPR scenario loading regime.....62
Figure 29. Plastic knob position for abusive scenario.....62
Figure 30. Diagram of displacement amplitude against time for abusive scenario loading regime.....63
Figure 31. Typical thorax of a piglet on which the tests were performed (a) when unsupported (scale marker in cm) (b) in-situ within the testing rig.....64

Figure 32. Immature rib whilst in test rig (picture courtesy of Tom Howard).....73
Figure 33. Selected cross-sectional volume from mature rib section.....75
Figure 34. Calculated linear-elastic (stress-strain) behaviour of mature rib section.....76
Figure 35. Graph of force-displacement curves for first 5 compressions during CPR simulation on Pig 4.....79
Figure 36. Graph of peak force during each compression throughout CPR simulation for Pig 4.....80
Figure 37. Graph of force-displacement curves for first 5 compressions during CPR simulation on Pig 5.....81
Figure 38. Graph of maximum force during each compression during CPR simulation for Pig 5.....81
Figure 39. Photographs of Pig 5 thorax during CPR scenario mechanical test (a) internal view with spine inferior to sternum: red arrowhead indicating fracture to left rib 4, left circle damage to sternal end of left rib 5 (b) exterior view: red circle denotes a bleed from left rib 5 (c) exterior view: red circle highlighting bleed to right rib 4, red oval indicating two bleeds eminating from right rib 5.....82
Figure 40. Graph of force-displacement curves for first 5 compressions during CPR simulation on Pig 6.....83
Figure 41. Graph of maximum force during each compression during CPR simulation for Pig 6.....84
Figure 42. Photographs of Pig 6 thorax during CPR scenario mechanical test (a) internal view with spine inferior to sternum: red oval indicating multiple lateral fractures to sternal end of right rib 4 (b) external view: red arrowhead highlighting costochondral failure to left rib 5.....84
Figure 43: Load against displacement graph for mechanical test on Pig 2.....86
Figure 44. Photograph of external of Pig 2 thorax following abusive scenario mechanical test: red circle indicating costochondral failure to right rib 5.....87
Figure 45: Load against displacement graph for mechanical test on Pig 3.....88
Figure 46. Photographs of Pig 3 thorax during abusive scenario mechanical test (a) external view with spine inferior to sternum: red arrows indicating bleeds from anterior rib fractures (b) external view: red circle highlighting complete rib fracture to right rib 6.....88
Figure 47: Load against displacement graph for mechanical test on Pig 7.....89
Figure 48. Photograph of internal of Pig 7 thorax during abusive scenario mechanical test (red arrowheads indicate bleeds from posterior rib fractures, red oval highlighting damage to right rib 5).....89
Figure 49: Load against displacement graph for mechanical test on Pig 8.....90
Figure 50. Photograph of internal of Pig 8 thorax during abusive scenario mechanical test (red arrowheads indicating apparent fractures to posterior of left ribs 7 and 8, red oval highlighting heavily distorted right rib 5, and blue oval indicating left rib 6).....91
Figure 51: Load against displacement graph for mechanical test on Pig 9.....91
Figure 52. Photograph of internal of Pig 9 during abusive scenario mechanical test (red arrows indicate bleeds from anterior rib fractures).....92
Figure 53. CT slices through transverse and coronal planes of Pig 4 following CPR scenario mechanical test. See text for annotation detail.....95
Figure 54. CT slice through transverse plane of Pig 4 at level of the posterior of the 6th ribs following CPR scenario mechanical test. Annotation detail within accompanying text.....96
Figure 55. CT slices of Pig 5 following CPR scenario mechanical test (a) transverse plane (b) coronal plane. Explanation of annotations within text.....96
Figure 56. CT slice through transverse plane of Pig 5 at the posterior level of the 5th rib pair following CPR scenario mechanical test. Annotation detail within text.....97
Figure 57. CT slices of Pig 6 following CPR scenario mechanical test (a) transverse plane (b) coronal plane. See text for annotation details.....98

Figure 58. CT slices of Pig 2 following abusive scenario mechanical test (a) transverse plane (b) coronal plane. Annotation detail within text.....101
Figure 59. Coronal plane CT slice of Pig 2 taken through posterior of ribs subsequent to abusive scenario mechanical test. See text for annotation detail.....102
Figure 60. CT slices of Pig 3 following abusive scenario mechanical test (a) transverse plane (b) coronal plane. Annotation detail within text.....102
Figure 61. CT slices detailing lateral fractures following abusive scenario mechanical test on Pig 3 (a) transverse plane (b) coronal plane. Annotation detail within main body text. 103
Figure 62. CT slices of Pig 7 following abusive scenario mechanical test (a) transverse plane (b) coronal plane. See text for annotation detail.....103
Figure 63. CT slices of Pig 7 following abusive scenario mechanical test (a) transverse plane (b) coronal plane. Annotation detail within text.....104
Figure 64. CT slices through transverse plane of Pig 8 following abusive scenario mechanical test (a) taken level with anterior of 5th rib pair (b) taken level with anterior of 6th rib pair. Annotation details within text.....105
Figure 65. CT slices of Pig 9 following abusive scenario mechanical test (a) transverse plane (b) coronal plane. See text for annotation details.....105
Figure 66. CT slice through coronal plane of Pig 9 following abusive scenario mechanical test. Annotation detail within accompanying text.....106
Figure 67. Anterior region of characteristic piglet rib before mechanical testing (a) superior view of sternal end of rib (area of lower density bone highlighted) (b) oblique view of sternal end of rib (pink highlights bone collar).....108
Figure 68. 3D visualisation from CT data of a characteristic costochondral junction fracture (red oval highlights the separated rim of rib bone).....109
Figure 69. 3D rendering from CT data of a characteristic rib showing posterior foramen. 109
Figure 70. 3D rendering from X-ray Tomography scan of mature rib rib section taken before mechanical testing.....110
Figure 71. Load-displacement curve for 6.2 mm section of mature rib under compression. 110
Figure 72. Mature rib section under compression.....111
Figure 73. Load-displacement curve for a nanoindentation test on mature porcine rib.....112
Figure 74. Microtomography reconstructions of immature bone mechanical assessment samples; (a) 5mm sections, (b) entire rib.....113
Figure 75. Force-displacement curves for immature rib sections.....114
Figure 76. (a) Immature rib whilst in test rig, just after buckling (b) permanent deformation of rib after compression test.....114
Figure 77. Typical load-displacement curve from nanoindentation of immature porcine rib 115
Figure 78. Radiographs of immature full rib bones following mechanical testing (a) cropped region at sight of buckling, posterior to sternal end of rib (b) same region viewed at 90 degrees to first radiograph.....115
Figure 79. 25% resolution mesh of mature rib section.....116
Figure 80. Force displacement curve with mechanical experimental data and FE simulation data for mature rib section.....117
Figure 81. Longitudinal section through simulated stress distribution for mature rib section at 0.75 percent strain with Young's modulus of 5.3 GPa.....117
Figure 82 Transverse cross-section through mature rib section (a) X-ray CT image data (b) applied segmentation of the model mask.....118
Figure 83. Graph of model element count against model resolution for All tetrahedra Adaptive Meshing -50cc.....120

Figure 84. Graph of reaction force against model resolution for simulations using All tetrahedra Adaptive Meshing -50cc, Young's modulus = 12 GPa.....120
Figure 85. FE simulations of mechanical assessment tests for immature ribs (a) 5mm section (b) entire rib.....121

Index of Tables

Table 1: Anatomical Directional Terms and their Corresponding Axes and Longitudinal Planes.....20
Table 2. Incidence of rib fractures in abused infants and their relative distribution along the length of the rib.....43
Table 3. Calculated stress-strain values for mature rib section.....76
Table 4. Peak forces and displacements for mechanical CPR simulations on pig rib cages 4-6.....85
Table 5. Summary of abusive scenario mechanical tests.....93
Table 6. Summary of CPR Fractures (N= no fracture; Y=fracture; P= possible fracture….94
Table 7. Summary of CPR Fractures (N= no fracture; Y=fracture; P= possible fracture….99
Table 8. Summary of abusive fractures identified using radiography (N= no fracture; Y=fracture; P= possible fracture).....100
Table 9. Summary of Abusive Fractures (N= no fracture; Y=fracture; P= possible fracture 107
Table 10. Force measured from experimental work within the elastic region.....111
Table 11. Young's modulus and hardness obtained from nanoindentation tests on mature porcine rib.....112
Table 12. Loads calculated from finite element with Young's modulus of 12 GPa 116
Table 13. Loads calculated from finite element with Young's modulus of 5.3 GPa 116
Table 14 Details of mature bone simulations run with all tetrahedra +FE Grid mesh (1x1x1), and Young's modulus of 12 GPa.....118
Table 15 Details of mature bone simulations run with all tetrahedra adaptive meshing 0cc, and Young's modulus of 12 GPa.....119
Table 16 Details of mature bone simulations run with all tetrahedra adaptive meshing -50cc, and Young's modulus of 12 GPa.....119
Table 17 Details of mature bone simulations run with all tetrahedra adaptive meshing -50cc, and Young's modulus of 11 GPa.....120

Abstract

The presence of rib fractures in deceased infants is generally considered to be highly specific of non-accidental injury, with some pathologists considering them to be evidence of abuse. Although rib fractures may occur during resuscitative efforts in adults, the general consensus is that such injuries are exceptional in infants owing to inherent plasticity within the thoracic region. The recommendation for cardiopulmonary resuscitation (CPR) of infants since the year 2000 has been for the use of the "two-thumb" technique. However, there has been limited biomechanical investigation to what injuries may occur subsequent to this specific form of CPR. The overall aim of this thesis was to determine if two-thumb CPR can cause similar rib injuries to those seen in abusive squeezing cases. In particular, whether or not this CPR technique allows for over excessive levering of the posterior rib over the transverse process of the spine. To this end, physical experimentation simulating both two-thumb CPR and abusive squeezing was performed on an immature swine model of the infant thorax. The results of these tests did not show any significant difference in the force required to compress the thorax by one third its original anterior-posterior diameter in the two scenarios. One third being the recommended depth for CPR compressions. Fractures resultant from the testing were assessed with radiography and computed tomography, techniques commonly used by post-mortem pathologists. The type and nature of the injuries observed were remarkably similar in both scenarios. Rib injuries were primarily seen in the anterior part of the thoracic cage in both CPR and abusive specimens. The specific site of rib fracture was typically close to or within the costochondral joints. There was however an apparent absence of posterior rib fractures in the abusively tested cohort. This is in part due to the slight difference in profile of the neck and head areas within the ribs of the surrogate model. This acts to reduce the mechanical advantage offered by levering over the transverse processes of the spine.

This study has shown anterior fractures of the ribs result from two-thumb CPR, challenging the long held belief that CPR cannot produce rib fractures. X-ray CT offered a significant improvement on the ability to detect costochondral junction injuries. This would offer further support to the routine use of X-ray CT in post-mortem examinations of infants where the cause of death is unknown. This has the potential to offer differential interpretation to the cause of rib injuries, especially in cases of sudden unexpected deaths in infancy, where otherwise child abuse may be diagnosed.

Declaration

No portion of the work referred to in this thesis has been submitted in support of an application for another degree or qualification of this or any other university or other institute of learning.

Copyright Statement

i. The author of this thesis (including any appendices and/or schedules to this thesis) owns certain copyright or related rights in it (the “Copyright”) and s/he has given The University of Manchester certain rights to use such Copyright, including for administrative purposes.

ii. Copies of this thesis, either in full or in extracts and whether in hard or electronic copy, may be made only in accordance with the Copyright, Designs and Patents Act 1988 (as amended) and regulations issued under it or, where appropriate, in accordance with licensing agreements which the University has from time to time. This page must form part of any such copies made.

iii. The ownership of certain Copyright, patents, designs, trade marks and other intellectual property (the “Intellectual Property”) and any reproductions of copyright works in the thesis, for example graphs and tables (“Reproductions”), which may be described in this thesis, may not be owned by the author and may be owned by third parties. Such Intellectual Property and Reproductions cannot and must not be made available for use without the prior written permission of the owner(s) of the relevant Intellectual Property and/or Reproductions.

iv. Further information on the conditions under which disclosure, publication and commercialisation of this thesis, the Copyright and any Intellectual Property and/or Reproductions described in it may take place is available in the University IP Policy (see http://www.campus.manchester.ac.uk/medialibrary/policies/intellectual-property.pdf), in any relevant Thesis restriction declarations deposited in the University Library, The University Library's regulations (see http://www.manchester.ac.uk/library/aboutus/regulations) and in The University's policy on presentation of Theses

Acknowledgements

The author would firstly like to thank my supervisors, Professor Paul Mummery and Dr Lee Margetts, for their conversations and guidance during the course of my thesis studies. A special thanks goes to Dr Andy Hodgkins who mentored me through the final stages of my thesis; his time, expertise, guidance, and comments on the manuscript were invaluable.

I am grateful to all the technical staff at the Materials Science Centre and the Biological Services Facility for their time, valuable advice, and assistance regarding the experiments conducted for this thesis.

The author would like to thank the EPSRC for funding my project through the doctoral training account, and Professor Tony Freemont for the financial support he provided during my PhD.

I would also like to thank my friends and colleagues, too numerous to mention, for their advice, encouragement and keeping me sane (for the most part).

Finally, I offer my thanks and appreciation to my parents, Janice and Peter Johnson, for their continued support and for being a constant source of encouragement, without which this thesis would not have been possible.

"N*ever give in. Never give in. Never, never, never, never– in nothing, great or small, large or petty– never give in except to convictions of honour and good sense. Never yield to force; never yield to the apparently overwhelming might of the enemy.*"
– Sir Winston Churchill (British politician, 1874 - 1965)

CHAPTER ONE

1 Introduction

The objective of this thesis is to look for differences and/or similarities in fracture type and location of infant rib fractures resulting from simulated cardiopulmonary resuscitation (CPR) and abusive trauma.

Recognition and correct differentiation of CPR-related fractures from fractures due to abuse could have medicolegal implications (Plunkett, 2006). A study to determine whether two-thumb CPR in infants can cause similar rib fractures to those seen in abusive squeezing is clearly timely. This information should help to inform the decisions of front line medical professionals, pathologists, and expert witnesses in legal cases, enabling them to provide more appropriate and consistent diagnoses.

In the United Kingdom, sudden unexpected deaths in infancy (SUDI) automatically prompt a post-mortem by a pathologist (Kennedy, 2004). All SUDI post-mortem examinations include a radiological skeletal survey to be undertaken prior to the autopsy to detect bony injuries that may be associated with non-accidental injury (NAI) (Kennedy, 2004). The usefulness of post-mortem radiographic examinations has been shown, whereas important diagnostic information may be missed when only clinical examination and autopsy alone are performed (McGraw *et al*., 2002).

Fractures amongst infants (children < 2 years old) are judged to be one of the most indicative injuries of child abuse (Kemp *et al*., 2008). Accidental injuries are less likely to be seen in infants due to their low independent mobility, and low mass (Maguire, 2010). In addition, the inherent plasticity of their skeletal system requires a great deal of force to cause a fracture (Matshes and Lew, 2010). When all other explanations for a fracture are eliminated, such as disease, trauma during a difficult birth, accidental injury such as a fall or road traffic accident, the fracture is adjudged to be the result of NAI, i.e. deliberate child abuse.

Of all bony injuries, the general consensus is that rib fractures amongst infants are seen as being highly indicative of child abuse. Thus when they are detected it usually requires an immediate investigation into their cause. Suspicion is immediately placed upon the child's carers (parents, family members, child minders), with the default position both legally and clinically being that abuse has taken place until proven otherwise, or there is insufficient and/or inconclusive evidence.

On occasion, CPR has been offered as a defence against allegations of child abuse. Individuals accused of inflicting fatal injuries on infants will attribute the cause of the injuries found at autopsy to their "untrained" resuscitative efforts, rather than gross maltreatment. Historically, this "CPR defence" was widely discredited following research into fractures caused by single hand two-finger CPR, as rib fractures of young children were infrequently observed following CPR (Cadzow and Armstrong, 2000; Matshes and Lew, 2010).

Of instances when paediatric rib fractures have been shown to be resultant from CPR, they were located anterolaterally within the rib cage (Betz and Liebhardt, 1994; Bush *et al*., 1996; Weber *et al*., 2009).

Shaken baby syndrome (SBS) is characterised by certain injuries, including rib fractures. Their discovery infers child abuse, with medical professionals strongly suspecting intentional shaking as the mechanism of injury. Components of this mechanism are anterior-posterior compression of the thorax, with the child held out in front of the aggressor, the hands of the aggressor gripped around the chest, and violent back-and-forth shaking of the infant. The squeezing of the thorax along with the unsupported nature of the posterior rib elements, is thought to cause excessive levering of the rib over the vertebral transverse process (Kleinman and Schlesinger, 1997), thus causing posterior rib fracture at or near the costotransverse process articulation.

The year 2000 saw a change to the International Guidelines for infant CPR (*Circulation*, 2000), with two-handed, two-thumbed sternal compression with both hands encircling the torso being recommended as the preferred methodology. This CPR technique positions the hands in a way not dissimilar to that theorised to cause rib fractures during abusive squeezing and shaking of an infant. The traumatic nature of the CPR procedure also provides the necessary anterior-posterior compression to the upper thorax. Matshes and Lew (2010) highlighted this as a potential area of investigation, but hypothesised that the forces involved in CPR would not be sufficient to cause posterior rib fractures. More recently, Reyes *et al*. (2011) highlighted an increase in frequency of CPR-associated rib fractures following the change in recommendation to infant CPR technique.

Biomechanical analysis of traumatic injury is increasingly being used to evaluate or explain how many injuries may have occurred (Freeman and Kohles, 2010). For instance, data derived from experimentally produced forces acting on a given tissue may be used to explain the cause of injury (Hayes *et al*., 2007).

Considerable research has been conducted on the biomechanics of bone (e.g. Ascenzi *et al*., 1990; Yaszemski *et al*., 1996) together with the specific biomechanical testing of ribs (e.g. Shultz *et al*., 1974; Malone, 1986; Daegling *et al*., 2008; Weller, 2011). Notwithstanding, it is known that partially mineralised immature bone does not behave in the same way as adult bone (Ogden, 2000). While the toughening mechanisms of adult bone are well understood (Ritchie *et al*., 2009; Diab and Vashishth, 2007), there is a paucity of data regarding the biomechanical behaviour of young bone, especially within infant rib tissue.

Biomechanical analysis into the effects of these two types of trauma (squeezing and two-thumb CPR) on the ribs of the infant thorax, will give a better insight to any potential similarities or differences. This should reduce uncertainty in the diagnosis of abuse in cases where the "CPR defence" has been offered, ultimately diminishing the current subjectivity when interpreting infant rib fractures.

In line with the most common diagnostic technique available to pathologists, principle rib fracture and damage characterisation within this study will be undertaken using X-ray radiography. Frequently, rib fractures may be the only skeletal evidence of trauma, but they have been shown to be difficult to visualise with radiography (Kleinman, *et al*., 1988). Acute non-displaced rib fractures resultant from trauma at, or just prior to death, are particularly difficult to visualise as there is no time for the typical bone tissue healing response to be exhibited (e.g. fracture calluses) (Kleinman *et al*., 1988).

X-ray computed tomography (CT) has been reported to have an increased sensitivity for detecting rib fractures (Renton *et al*., 2003; Wootton-Gorges *et al*., 2008; Hong *et al*., 2011), and is a methodology readily available to pathologists. To this end, X-ray CT will be used to provide more information within this study, as 3D visualisation offers more precise fracture characterisation in terms of location and type.

1.1 The Objectives of the Study

The primary aim of this thesis is to examine the biomechanical behaviour of juvenile ribs in an experimental animal, under conditions that mimic both abusive squeezing and two-thumb CPR.

Specific objectives and questions that will be addressed are:-

- Selection of a suitable experimental animal for simulating the human infant thorax.
- Improved understanding of the damage mechanisms associated with two-thumb CPR and abusive squeezing.

- Can two-thumb CPR cause similar injuries to those seen in abusive squeezing?
- Specifically, can two-thumb CPR cause excessive levering of the ribs over the vertebral transverse processes?
- An enhancement of the volume and quality of the data available for informing diagnoses of child abuse.

1.2 Thesis Structure

The structure and content of the thesis is outlined below:-

Chapter 2 contains a literature review. In this section consideration will be given to a detailed examination of the human skeleton with emphasis on the thoracic structure. The comparison between the human thoracic structure and that of potential surrogate animals is also considered in chapter 2 along with an examination of the grip, or contact associated with CPR and abusive squeezing. Finally, the types of loading introduced by CPR and that associated with abusive squeezing are explored; the information is used to plan the experimental programme.

Chapter 3 describes the experimental methodology used in this study. It contains a full description of the load rig, the load configurations used and the techniques used to observe the effects of loading on the test specimens.

Chapter 4 presents the results of the experiments.

Chapter 5 has a discussion of the experimental programme and the results. Here the emphasis is placed on the differences observed due to the different 'gripping' modes and load regimes and how these differences may help to provide evidence to differentiate between the two.

Chapter 6 summarises the main conclusions of this thesis.

CHAPTER TWO

2 Literature Review

The intention of this chapter is to provide a general introduction to the area of research investigated within this thesis, along with fundamental knowledge central to the previously outlined research goals.

2.1 The Language of Anatomy for Humans and Quadrupeds

For the assistance of readers that are not familar with formal anatomical terminology, the most important terms are now summarised for both humans and quadrupeds. Knowledge and understanding of these will allow body structures to be located and indentified with a minimum of words and a high degree of clarity. These terms will be used to describe and discuss the biomechanics of CPR and abuse.

Specific areas of the human body are discussed in reference to a universally accepted standard position known as the anatomical position. In the anatomic position the human body is erect, with the arms hanging at the side with palms facing forward, feet together, head and toes pointed forward (Figure 1a).

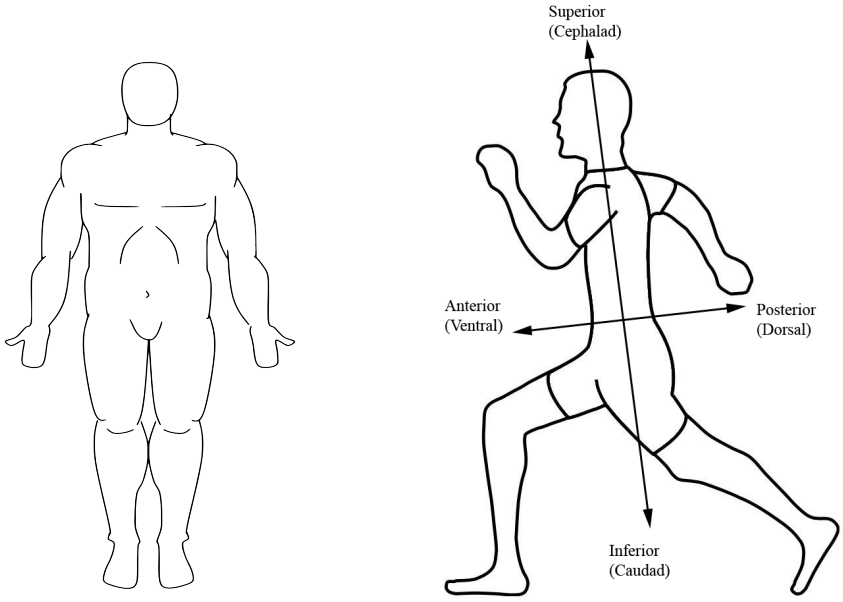

(a) (b)

Figure 1. The anatomical position (a) and anatomic terminology describing body orientation and direction (b)

(a) http://commons.wikimedia.org/wiki/File:Anatomical_Position.png (Accessed 28/02/2013)
(b) http://www.edupics.com/coloring-page-to-run-i19311.html (Accessed 06/03/2013)

The following terms of position described are dependent on an assumption of the anatomical position. Superior and inferior refer to the placement of an anatomical structure

relative to the vertical axis of the body; superior structures are above inferior ones e.g. the eyes are superior to the mouth.

Anterior and posterior relate to the front and back of an organism respectively. Medial structures are closer to the midline of an organism whereas lateral structures are further away e.g. the breastbone is medial to the ribs.

The next series of terms are more absolute; that is, their applicability is not dependent on being in a particular body position, and they consistently have the same meaning in all vertebrate animals (Figure 1b and Figure 2).

Cephalad and caudal are directional terms, meaning toward the head and toward the posterior end of the body/the tail of the spinal cord. In humans, caudal is towards the feet, whereas in quadrupeds it is toward the tail.

Dorsal is toward, on, in, or near the back of an animal, whilst ventral always refers to the bellyside of the animal.

When a structure is proximal, it is next to or nearest where it joins the body/situated toward the centre of the body, this is in contrast to something that is distal i.e. further away from the trunk or point of attachment e.g. the knee is proximal to the toes.

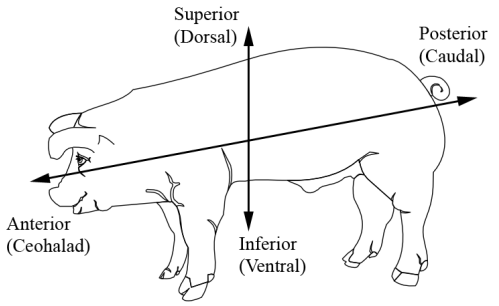

Figure 2: Anatomic terminology describing body orientation and direction of four-legged animal

Adapted from http://www.clker.com/clipart-pig-35.html (Accessed 08/09/2013)

Figure 3 shows the three commonly used planes, or sections, used by anatomists. These planes lie at right angles to one another, and are helpful when describing the orientation of a cut through an organ, or a section through the body wall.

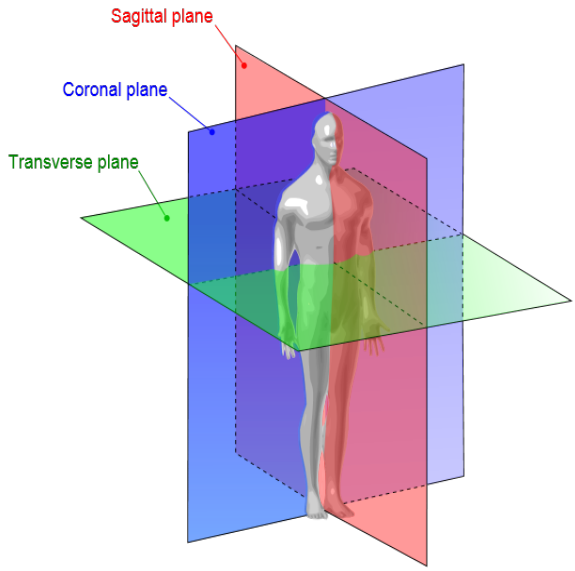

Figure 3. Planes of the body
http://commons.wikimedia.org/wiki/File:Human_anatomy_planes.svg (Accessed 15/09/2013)

When a cut along a longitudinal plane divides the body into right and left parts it is termed a sagittal section. When such a section divides the body into equal parts, i.e. exactly at the median plane of the body, it is called a midsagittal section.

A coronal section, sometimes called a frontal section, divides the body into anterior and posterior parts by a cut along the a longitudinal plane.

Division of the body into superior and inferior parts by a cut along a horizontal or transverse plane creates a transverse section, this is commonly called a cross section.

The relationship between the three sections described above and the main defined axes in vertebrate zoology are summarised in table 20.

Directional Term	***Defined Axis***	***Axis Runs***	***Corresponding Longitudinal Plane***
Anterior Posterior	Anteroposterior	From front to back	Coronal (frontal)
Superior Inferior	Superiorinferior	From top to bottom	Transverse (cross section)
Medial Lateral (left or right)	Mediolateral	From centre of organism to one or other side	Sagittal (longitudinal)

Table 1: Anatomical Directional Terms and their Corresponding Axes and Longitudinal Planes

2.2 Bone Structure

Bone is one of natures natural composites. A stiff skeletal material made principally of the fibrous protein collagen, impregnated with a mineral closely resembling calcium phosphate (Currey, 2006). Bones come in a variety of shapes and have a complex internal and external architecture.

Owing to its hierarchical structure, bone is a complicated structure, and its mechanical properties can be considered at different levels of its organisation. Tests can be performed on bone at multiple length scales, however it is difficult and sometimes impossible to extrapolate mechanical behaviour between different length scales based only on the results from one test (Morgan *et al*., 2008). For instance, a whole bone may be stronger wholly down to its larger size, not because the tissue itself is any stronger.

To truly understand a bone's mechanical properties, one must have a knowledge and understanding of its structure. When discussing the structures of bone I follow Currey's convention (2006) of using the word *bones* to refer to the whole anatomical bone, such as the humerus, and the word *bone* to mean the bone tissue.

2.2.1 Types of Bone

On the macroscopic scale bone consists of two main types of osseous tissue, cortical and cancellous, the difference between the two types is visible to the naked eye (Currey, 2006).

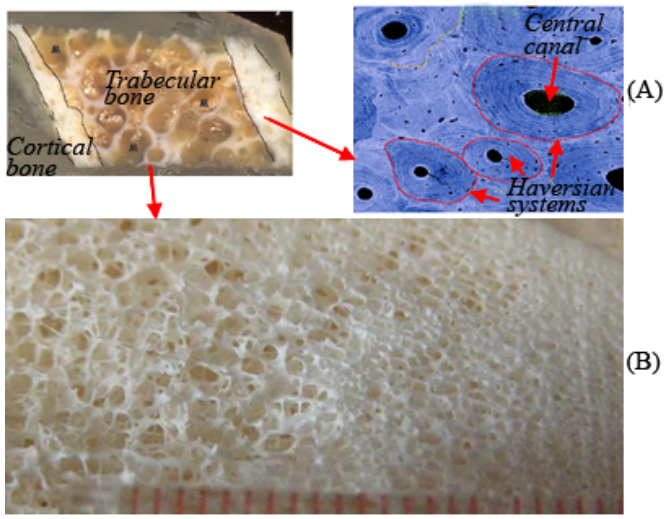

Figure 4. Types of bone tissue on the macroscopic scale (A) cortical bone (B) cancellous bone

(A) http://depts.washington.edu/bonebio/ASBMRed/structure.html.
(B) http://silver.neep.wisc.edu/~lakes/BoneTrab.html

Cortical bone

Cortical or compact bone is principally dense, with the only spaces being for canaliculi, osteocytes, blood vessels, and erosion cavities. Cortical bone is relatively stiff and strong when stressed parallel to the axis along which the osteons are aligned, and is typically found in regions where stresses arrive from a limited range of directions, for example the shafts of long bones.

First Level Cortical Bone Structure

At the microstructural level, cortical bone can be differentiated in to four different types of organisation; woven bone, primary bone, secondary bone, and plexiform bone (Martin and Burr, 1989; Currey, 2006). The different structural organisations are usually associated with either a specific age, species, or both, but still contain common second level entities such as lacunae and lamellae.

Woven-fibered cortical bone

Woven bone is the most disorganised bone tissue due to the circumstances in which it is formed. It is the only type of bone tissue that does not need to form on existing bone or cartilage tissue; it is therefore found in the developing skeleton of the young, and around fracture sites or diseased areas of the adult skeleton. Woven bone is usually laid down very rapidly, leading to a disorganised structure.

Primary bone

Osteonal bone is bone tissue in which blood vessels are surrounded by concentric rings of bone tissue. Specifically, an osteon is a structure including the central blood vessel and surrounding concentric bone tissue

Primary osteons are likely formed by mineralisation of cartilage, thus being formed where bone was not present. Therefore they do not contain as many lamellae. Additionally, vascular channels tend to be smaller than those in secondary osteons.

Secondary bone

Secondary osteons formed by replacement of existing bone. This remodeling process forms haversian canals. In addition to secondary osteons, secondary cortical bone tissue also contains interstitial bone.

Plexiform bone

Plexiform bone is rarely seen in human, and is therefore not discussed here.

Second Level Cortical Bone Structure

Four major matrix second level structural entities are lamellae, osteocyte, lacunae, osteocyte canaliculi, and cement lines.

Third Level Cortical Bone Structure

At this level there are two basic types; lamellar and woven. Both contain type I collagen/mineral composite. What differentiates these two structures is how the composite (primarily the collagen fibers) is organised.

In woven bone, the collagen fibers are randomly organised and very loosely packed. This is due to rapid manner in which this type of bone is laid down.

Lamellar bone, (found in primary osteonal, secondary osteonal bone, and plexiform bone) is laid down in a more organised fashion.

Cancellous bone

Cancellous or trabecular bone is often termed 'spongy bone'. This type of bone has a porous structure, constructed of interweaving threads of bone known as trabeculae that enclose large cavities containing red or yellow marrow.

Cancellous bone is much lighter than compact bone (per volume), typically being found in regions where bones are not greatly stressed, but also in regions where stresses arrive from different directions. The proximal epiphysis of the femur being an example where the stresses arrive from a range of directions; the trabeculae in this region are orientated along lines of stress, acting to transfer the force from the hip to the stiffer compact bone of the femoral shaft.

First Level Cancellous Bone Structure

The basic structural entity at first level of trabecular bone is the trabecula. Trabecula are most often characterised as rod or plate like structures. Trabeculae in general do not have a central canal with a blood vessel.

Second Level Cancellous Bone Structure

At this level cancellous bone displays the same entities as the second level structure of cortical bone, including lamellae, lacunae, canaliculi, and cement lines.

Third Level Cancellous Bone Structure

Cancellous bone tissue contains the same entities as those seen in the third level of cortical bone structure, namely the collagen fibril-mineral composite.

The hierarchical nature of bone

The figures below display the hierarchical nature of bone.

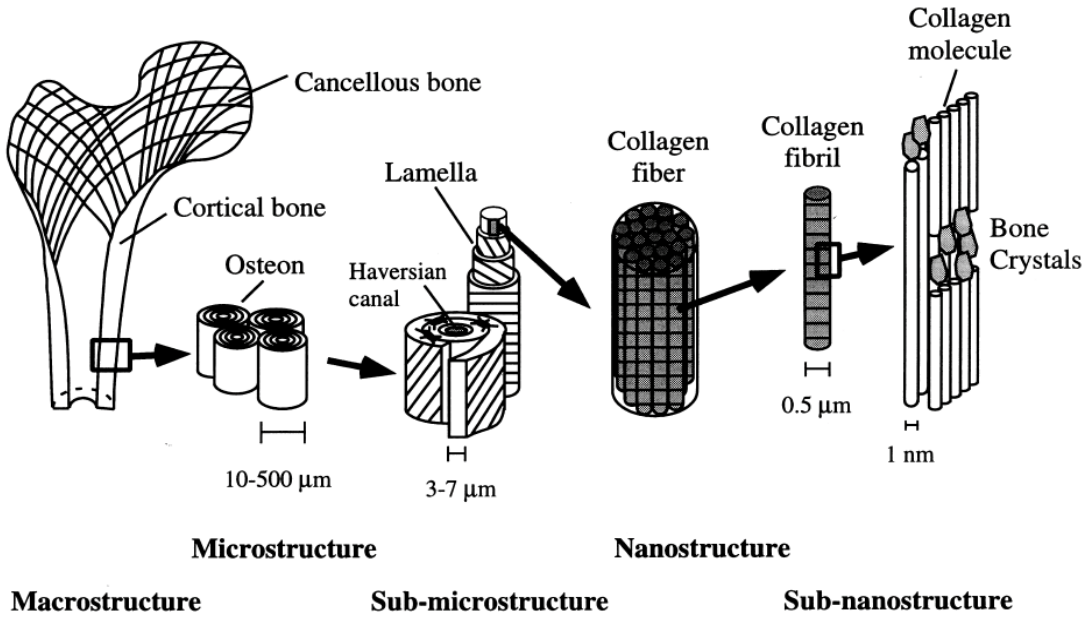

Figure 5. The hierarchical arrangement of bone

2.3 The Structure and Mechanical Behaviour of the Human Skeleton

2.3.1 Human Skeletal System

The skeletal system includes all the bones and joints in the body. It is composed of bones and cartilage. These components primarily act as a scaffold, providing support and protection for the soft tissues that make up the rest of the body. It also provides attachment points for the muscles, facilitating movement.

On a metabolic level, the skeleton performs several other functions, including, the storage of several minerals especially calcium and phosphorus, the production of blood cells in the red bone marrow of larger bones, and the storage of energy in the form of adipose cells within the yellow bone marrow.

The bones of the skeletal system are arranged into two major divisions: the axial skeleton and the appendicular skeleton (Figure 6). The axial skeleton is formed by the skull, vertebral column, and the rib cage, the later of which will now be discussed in greater detail.

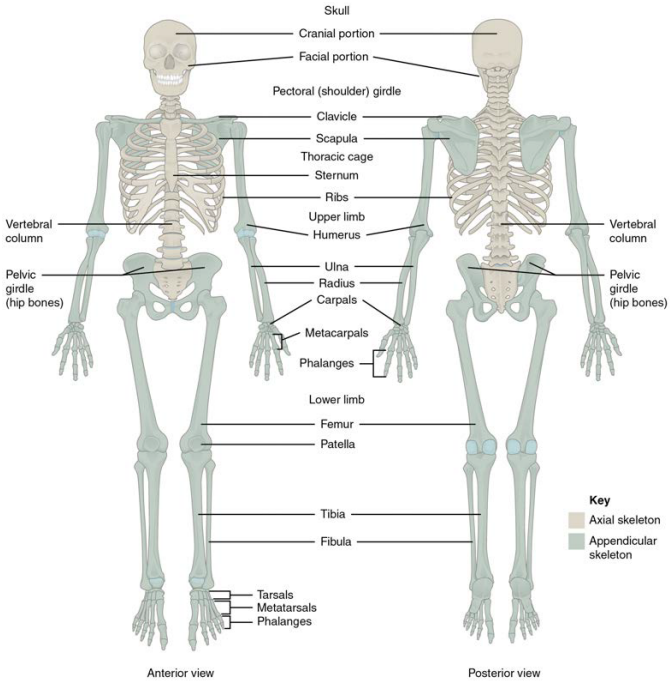

Figure 6. The Axial and Appendicular Skeleton (OpenStax College, 2013)

2.3.2 Human Thoracic Skeleton

A typical human thoracic skeleton, also referred to as the rib cage, comprises the ribs, the thoracic vertebrae, costal cartilages, and the sternum. It is these bony and cartilaginous structures, along with other associated soft tissues (muscles, ligaments, fascia, skin etc), that enclose the thoracic cavity.

The rib cage is an important structure within the human body as it provides protection for the underlying viscera, whilst also being a key component of the human respiratory system. It also affords attachments for the muscles aiding stability, support, and movement of the neck, back and upper abdomen.

Knowledge of the arrangement of various structural elements within the thoracic skeleton is essential in order to understand how they interact as a biomechanical system, and therefore where fracture injuries are likely.

Figure 7 illustrates the anatomical features of the adult human thoracic skeleton. It comprises the ribs, sternum, the twelve thoracic vertebrae and their intervening intervertebral discs, and hyaline cartilage.

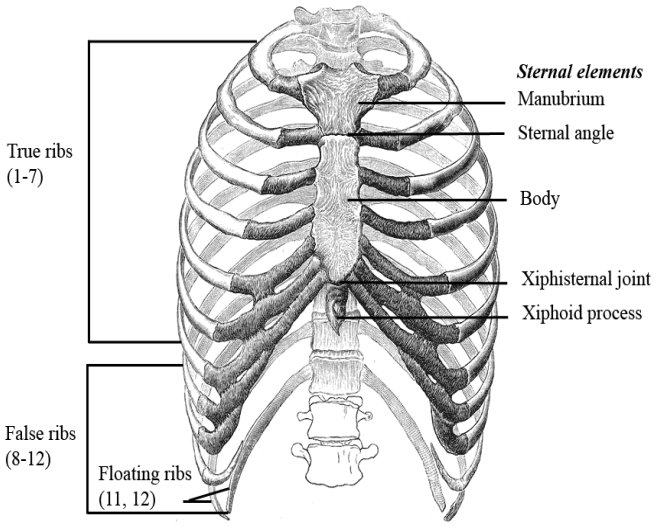

Figure 7: The human thoracic cage (Gray's Anatomy)

The human skeleton has twelve pairs of ribs, these can be classified in to two types, true ribs, and false ribs. Pairs 1-7 are termed true ribs as they directly attach to the sternum via costal cartilage. The false ribs are pairs 8-12; they are termed false ribs as they do not have a direct attachment to the sternum. Pairs 8-10 have an attachment to the sternum via the cartilage of the 7th rib. The anterior ends of the 11th and 12th pairs are free, having no attachment to the sternum, they are therefore commonly referred to as "floating ribs", and as such are only connected posteriorly to the vertebral column.

2.3.3 Human Ribs

The ribs are long curved bones sheathed with a periosteal layer. The anatomical features of a typical rib include both the anterior (or sternal) and posterior (or vertebral) extremities, and an intervening portion known as the body or shaft (Figure 6a). The body or shaft is thin and flat, with two surfaces, an external and an internal. The angle is the area of the shaft with the greatest curvature.

The posterior extremity is constructed of a head, neck, and tubercle (Figure 8b).

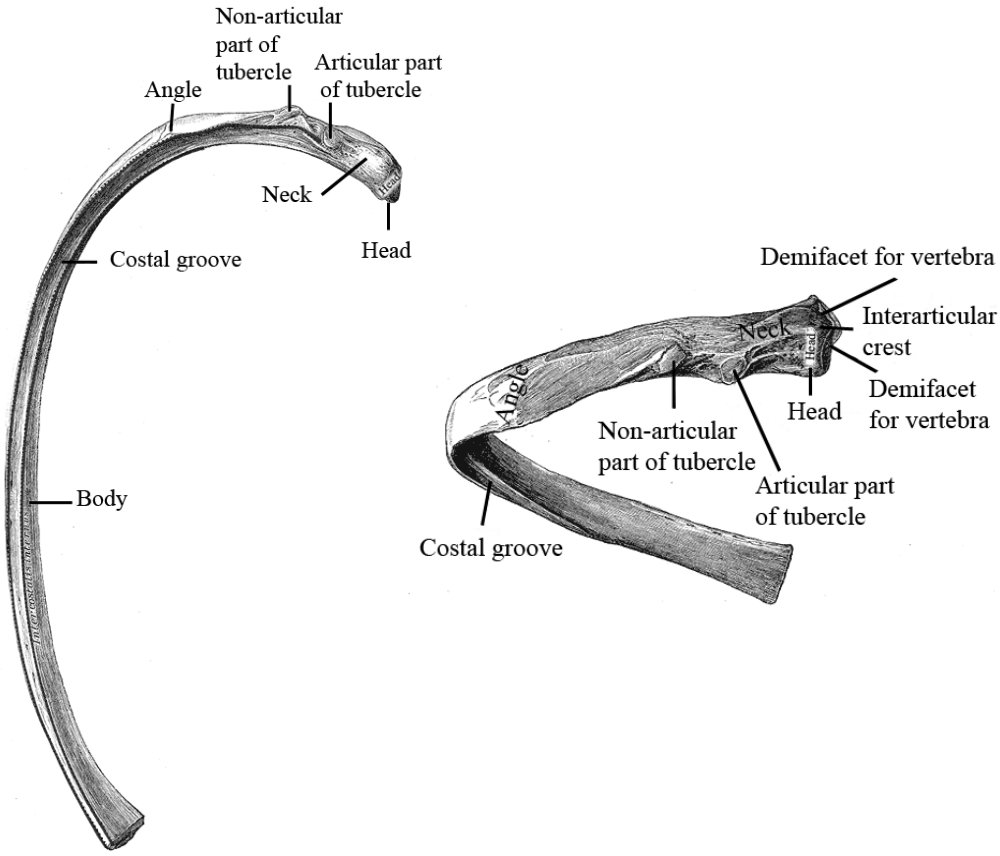

Figure 8: The geometry and landmarks of a "typical" rib (a) and the landmarks and features of the posterior extremity of a 'typical' rib (b) (Gray's Anatomy)

2.3.4 Human Sternum

The sternum is a bony structure that anchors the anterior of the thoracic cage. It consists of three parts (Figure 9): the manubrium is the superior part of the sternum, the body is located directly below and is the central, elongated portion of the sternum, and the xiphoid process is the inferior tip to the sternum.

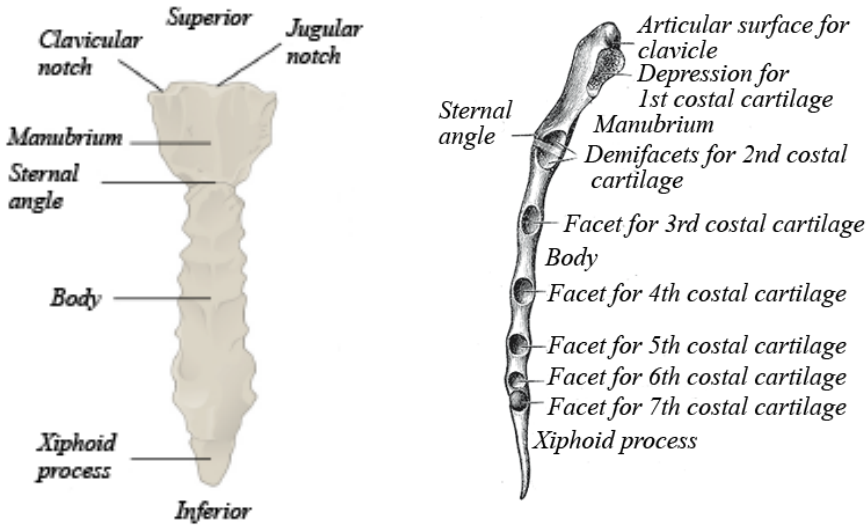

Figure 9. The human sternum (a) anterior view (b) left lateral aspect

(a) OpenStax College. 2013.
(b) Gray's Anatomy.

2.3.5 Articulations of the ribs

Generally, the ribs articulate ventrally to the sternum via costal cartilages, and dorsally with the vertebral column, however ribs 11 and 12 (floating ribs) have no ventral articulation.

Posterior rib articulations

The ribs articulate posteriorly with the thoracic vertebrae at two locations. At the costovertebral articulation the head of the rib articulates with the costal facets on the vertebrae Figure 10a.

The tubercle of the rib articulates with a facet located on the transverse process of the vertebrae, this is referred to as the costotransverse articulation (Figure 10b).

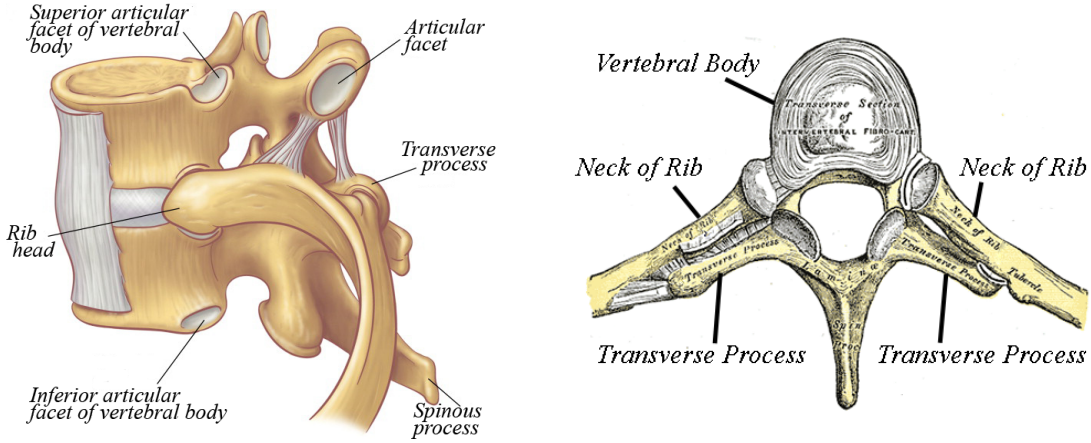

Figure 10: Posterior rib articulation with thoracic vertebrae (a) oblique aspect (b) superior aspect

(a) via www.studyblue.com (Accessed 02/10/2013)
(b) Gray's Anatomy.

Anterior rib articulations

Most ribs articulate anteriorly via their costal cartilages to the sternum (Figure 11). The articulation between the rib and the costal cartilage is known as the costochondral joint, whilst the sternocostal joint is between the costal cartilages and the sternum.

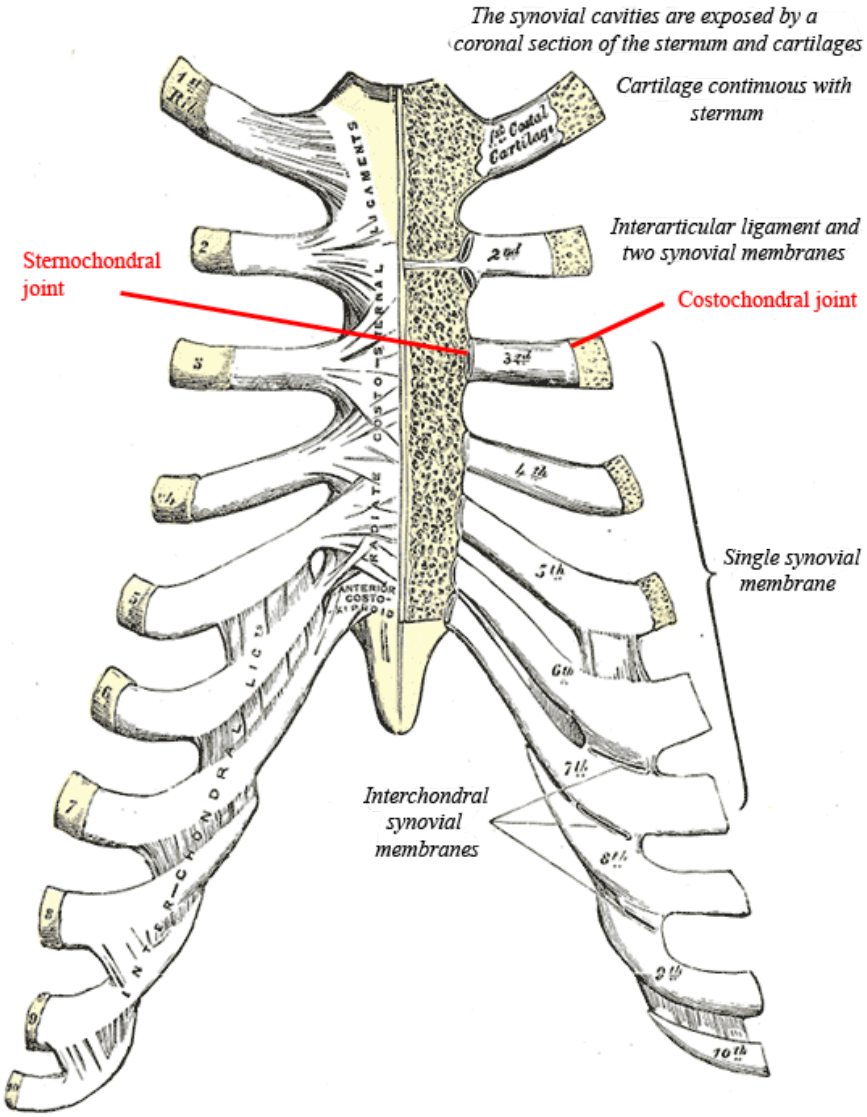

Figure 11. Anterior rib articulation with sternum (Gray's Anatomy)

2.3.6 Differences to the Infant Thorax

The thoracic cage undergoes numerous changes to its shape and material properties throughout life. At birth, the thoracic depth/thoracic width ratio is close to 1, appearing as roughly ovoid. At skeletal maturity, the thoracic depth/thoracic width ratio drops to lower that 1, with the thorax now displaying a broader and flatter elliptical cross-section (Canavese *et al*., 2013). This is the result of the pelvis becoming wider, permitting the abdominal contents to descend, coupled with the rib cage and sternum descending, the net result being a flatter thorax.

The descent of the sternum with respect to the spine following birth causes the ribs to move from an angle orientated close to the transverse plane to a more oblique, downward orientation (Hammer and Eber, 2005; Scheuer and Black, 2000).

Changes to the stiffness of the ribs and sternum take place as the skeleton becomes more ossified. At birth the ribs are relatively soft and flexible, becoming progressively more ossified and stiff with developmental age. The costal cartilage also calcifies with age.

In humans, the sternum is composed of six main bones. At birth the sternum is cartilaginous in nature, the different bones begin to appear and ossify at different stages of development. The superiorly postioned manubrium is first to appear, followed by sternebrae one through four, and the xiphoid process well into childhood (Figure 12).

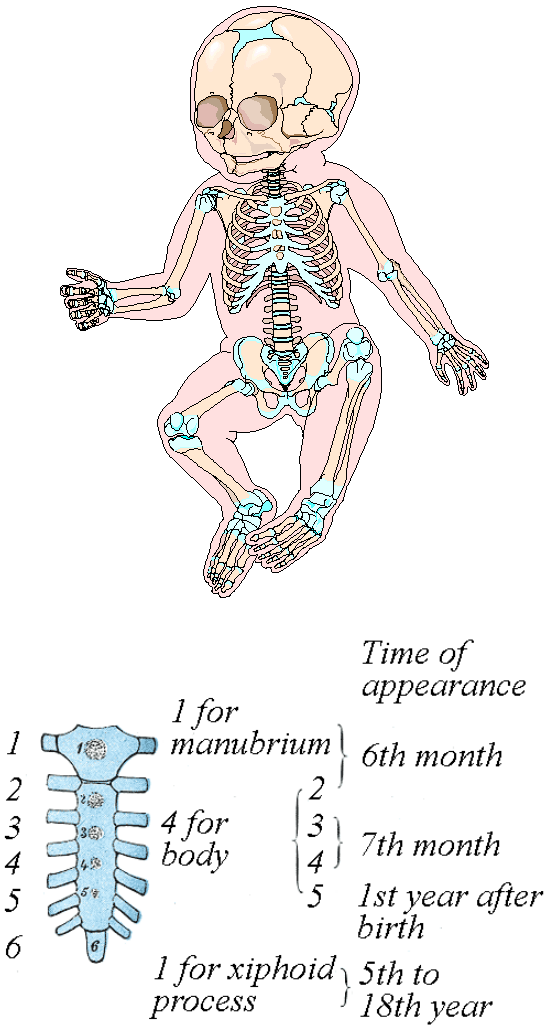

Figure 12. Development of the infant skeleton (a) The infant skeleton, light blue areas are cartilaginous (b) ossification of the sternum

(a) http://www.fotosearch.com/illustration/musculoskeletal-anatomy.html#comp.asp?recid=1540356&xtra= (Accessed 12/12/2013)
(b) Gray's Anatomy

2.4 Diseases that can Effect or Influence the Structure, Mechanical Behaviour and Strength of Bones

Although a complex process, the development of bone is generally successful, however there are diseases and other factors (such as historical breaks) that can lead to this process not being completed successfully. Knowledge of such conditions is important when providing a differential diagnosis of child abuse. Many of the conditions lead to a reduction in bone quality, often with the only visible presentation being multiple fractures in various stages of healing, usually this is seen as symptomatic of child abuse.

Rickets

Rickets is a condition that affects bone development in children and causes bones to become soft and weak, which can lead to bone deformities. Children can be born with a genetic form of rickets, though this is rare, far more commonly the cause of rickets is a lack of vitamin-D and calcium. The deficit of vitamin-D results in decreased serum calcium concentration and as a result the bone mineralisation process becomes defective (Khurana and Fitzpatrick, 2009). Ultimately this results in a loss of strength in the bone being formed and deformation to the epiphyseal plate.

Clinical signs of rickets include weakness, irritability, deformation such as bowed limbs, difficulty walking, stunted growth, and a prominent indentation of the lower rib cage (Khurana and Fitzpatrick, 2009). The extent of any fractures is dependent on the severity of the disorder and the age of the individual. The most common fractures are micro-fractures and even following healing deformities can be seen.

Osteomalacia

Osteomalacia is often referred to as the adult equivalent of rickets. However, in contrast to rickets, osteomalacia can be difficult to diagnose clinically due to the fact that no gross deformities are evident, whilst aches and pains can be attributed to other causal agents (Dent and Stamp, 1977). The lack of deformities or other obvious clinical identification markers, e.g. swelling of the epiphyseal ends, is a consequence of osteomalacia only affecting the new bone being laid onto an already normally formed skeleton (Dent and Stamp, 1977).

Osteogenesis imperfecta

Osteogenesis imperfecta (OI) also known as brittle bone disease, is a congenital bone disorder characterised by brittle bones that are prone to fracture. It is usually due to a deficiency of Type-I collagen that leads to people with the condition to be born with

defective connective tissue, or without the ability to make it (Rauch and Glorieux, 2004). Rather than being a single disease entity, there are eight different types of OI, all affecting collagen synthesis (Ojima *et al*., 1994).

As highlight in previous studies (Gahagan and Rimza, 1991; Ojima *et al*., 1994), OI can be mistaken for child abuse owing to the uncommon nature of frequent fractures in young children. As OI is relatively uncommon, it can be overlooked as a potential diagnosis, especially when the fractures observed are inconsistent to the reported trauma.

Osteopetrosis

Osteopetrosis, also known as Albers-Schönberg disease, is a extremely rare inherited disorder whereby the bones harden as a result of failed bone resorption, whilst bone formation persists. The resultant accumulation of excessive bone reduces the space available for bone marrow, and as a consequence there is a decline in hematopoiesis, or even a complete failure of the bone marrow (Key and Ries, 2002). This leads to the sufferers bones becoming dense and having substandard blood cell production as well as poor vascularisation, leaving them prone to fracture as well as necrosis and infection (Key and Ries, 2002).

The disease can take several forms, ranging in severity from a fatal infantile malignant form present at birth causing the individual to typically die within the first decade of life, to a mild adult form with long term survival (Key and Ries, 2002).

Osteoporosis

Osteoporosis is a disease characterised by too little bone formation, excessive bone loss, or a combination of the two. People with the condition have bones with a low mass and density, leading them to have an increased risk of fractures. Although most common in older people, in rare cases it can occur in children and is known as juvenile osteoporosis. It occurs when bones lose minerals, such as calcium, quicker than the body can replace them.

Typically it is caused by a underlying medical disorder, however in secondary osteoporosis the it is caused by medications or therapy used to treat another primary disorder. Lifestyle factors such as poor diet and a lack of exercise can also be a cause. With idiopathic osteoporosis the sufferer has no identifiable cause for the condition.

2.5 Selection of a Suitable Surrogate Animal

Mechanical testing on human infant cadavers has strong ethical constraints. The handling and testing of human tissue is tightly regulated. Further obstacles include obtaining post-mortem infants without any underlying disease or trauma, and being able to observe numerous subjects over a relatively short time frame for comparative purposes. As a consequence alternative approaches have to be explored.

Development of a computational model to simulate human infant thoracic mechanical behaviour is currently not possible as there is insufficient reliable and accurate input data to inform such models.

Physical experimental studies on a suitable animal surrogate can be used to increase understanding of the biomechanical behaviour of the thorax and the fracture mechanics of immature bone. Data from experiments can be used to inform and validate computational models of the surrogate, aiding in the development of thoracic cage models. Developing such computational models will further knowledge and understanding of biomechanical modelling of the thorax structure. This knowledge can be used to better inform the development of suitable human infant thorax models, ultimately leading to a better understanding of their trauma biomechanics.

Comparison of bone composition across various species identified canine bone as most closely resembling human bone (Aerssens *et al*., 1998). Porcine bone was also shown to have close similarities in bone mineral density and bone mineral concentration to human bone (Aerssens *et al*., 1998).

With regard to bone anatomy, morphology, healing and remodelling, the pig is considered to be closely representative of human bone and therefore a suitable species of choice (Thorwarth *et al*., 2005).

The pig is described as having a lamellar bone structure which is similar to that of humans, however they exhibit a denser trabecular network (Mosekilde *et al*., 1987). Even so, pigs are reported as the subject of choice in a variety of studies including studies of osteonecrosis of the femoral head, fractures of cartilage and bone, bone ingrowth studies, and studies evaluating new dental implant designs (An and Friedman, 1999; Buser *et al*., 1991; Sun *et al*., 1999). Moreover, pig bones have previously been shown to be good models for human trauma analysis (Lyn and Fairgrieve, 2009; Kieser *et al*., 2011).

Domestic pigs are readily available and inexpensive because they are well established as a food source. This makes their use cost-effective in scientific studies. The similarity in size, anatomy, and physiology between pigs and adult humans make them frequently the

primary biomedical model for a number of diseases, for surgical research, and for organ transplantation (Swanson *et al*., 2004).

Across various breeds, the thorax of the pig has a total 13-17 pairs of ribs. All pig breeds have seven pairs of sternal ribs, identical to the number of sternal ribs in humans. The pig has a total of six sternabrae. The ribs of the pig have the same anterior and posterior articulations as their human counterparts. This gives the pig a thorax that is directly comparable to humans (Figure 13).

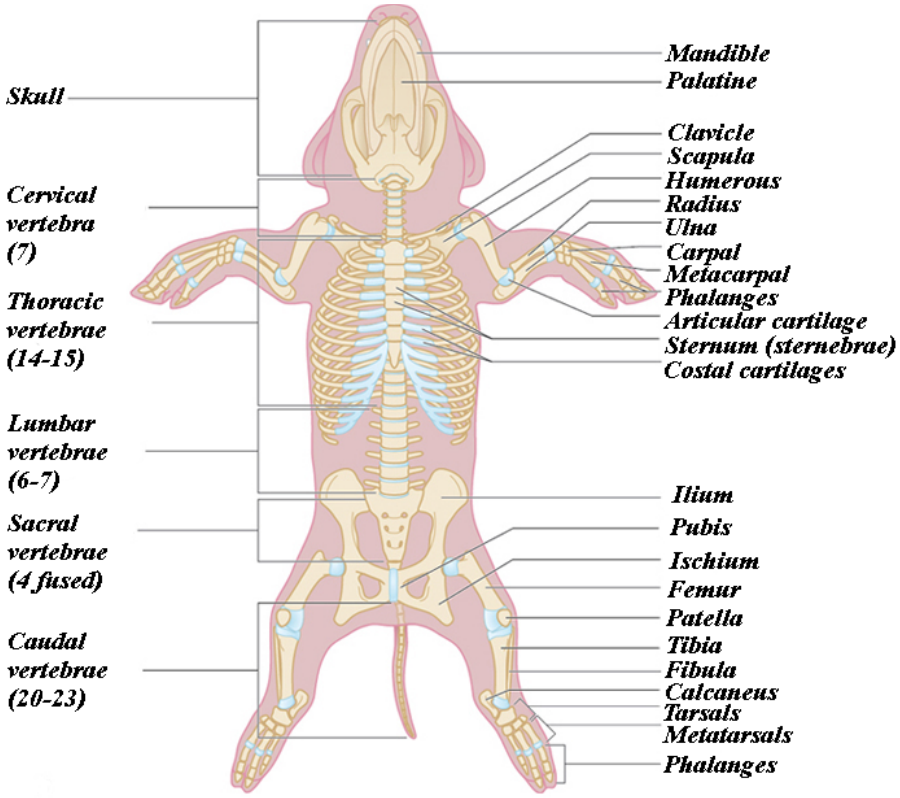

Figure 13. Fetal pig skeletal system

Libby Lamb Medical Illustation. http://libbylamb.com/fetalpig.html (Accessed 02/12/2013)

Domestic pigs (Sus scrofa domesticus) weighing 20-25 kg are recommended as having a similar anteroposterior diameter as adult humans (Idris *et al*., 1996). Pigs in this weight range have been selected for use in resuscitation studies relating to adult humans (Steen *et al*., 2002; Liao *et al*., 2010). Figure 14 displays a cross-section through the thorax of a pig specimen tested in the Steen *et al.* (2002) study.

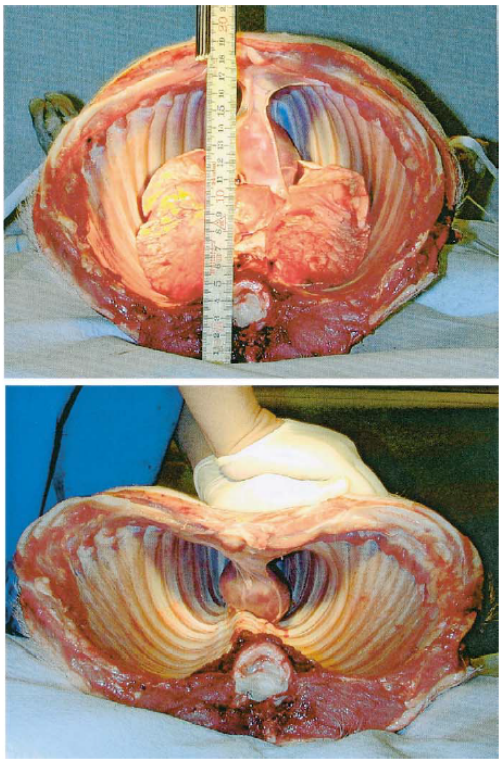

Figure 14. Transverse plane cross-section of 20-25 kg pig (Steen et al., 2002) (a) uncompressed anteroposterior diameter ~ 19.5 cm (b) simulated chest compression

At birth, the thoracic depth/thoracic width ratio of the infant pig is close to 1, appearing as roughly ovoid. This is the same ratio as seen in human infants, resulting in piglets and human infants having comparable thorax shape. However, it is relevant to note that throughout skeletal development of the pig, the thoracic depth/thoracic width ratio rises to higher than 1. The result being the thorax of the adult pig is roughly tear drop shaped and clearly different to that of an adult human (Figure 15). Therefore, comparison between adult pigs and humans should be undertaken with caution.

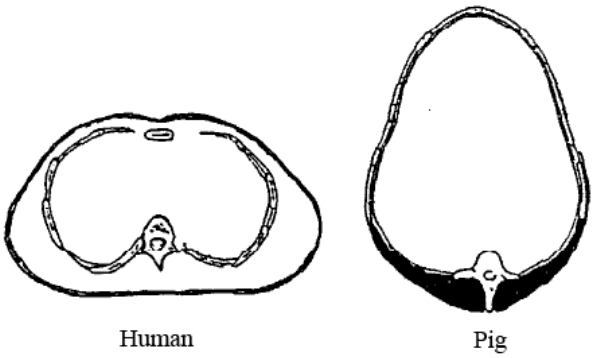

Figure 15. Cross-sectional drawing of the adult human and adult pig thorax (Adapted from Huelke et al., 1986)

Within large white pigs the newborn weighs around 1 kg, doubling in weight after one week, this compares to a body weight of 3 kg for a newborn human infants (Rendas *et al*., 1978). According to World Health Organisation (WHO) child growth guidelines human infants weight in the region of 7 kg at 6 months of age (Centres for Disease Control and Prevention, 2009).

The vertebral bone tissue of the pig appears consistent to that of humans when under X-ray radiological examination and has been shown as a suitable model (Teo et al., 2006). Cattaneo *et al*. (2006) used a piglet model to assess the sensitivity of autopsy and radiological examination in detecting bone fractures in the context of child abuse. These two studies demonstrate the suitability of a piglet model when assessing simulated abusive fractures with radiography and X-ray computed tomography.

2.6 Forces and Damage Inflicted on the Body During Infant CPR

CPR is an emergency procedure performed when a person is found to be unresponsive, likely suffering from cardiac arrest, with no, or irregular breathing. CPR by itself is unlikely to restart the heart, but it is recommended so as to manually restore flow of oxygenated blood to the brain. Even this partial flow of blood should delay tissue death, and thus preserve intact brain function. This procedure is purely aimed at extending the window of opportunity for other medical intervention (e.g. defibrillation) to be administered in order to restore a viable heart rhythm. CPR is typically persisted with until the subject regains return of spontaneous circulation, or is declared dead.

There are two recognised techniques for delivering chest compressions to infants, the two-finger, and the two-thumb methods. The procedure for two-finger CPR calls for the infant to be lying supine on a flat supportive surface. Two fingers are placed at approximately the midsternum at right angles to the chest, and a downward force is applied (Figure 16. (a)). The mechanics of this technique mean that only the ventral portion of the thorax can be compressed.

With two-handed CPR the infant is again in a supine position on a flat supportive surface, the thumbs are positioned anteriorly on the sternum, and they deliver the force to the chest, compressing it downwards (see Figure 16b). The second through fifth fingers are intended only as a simple brace to constrain lateral movement (Matshes and Lew, 2010), however depending on the vigorousness of the rescuers delivery of compressions, it is possible that the posterior of the thorax may be compressed (Figure 17.).

In both techniques the chest compressions should be coordinated with ventilations at a ratio of 3:1 and a rate of 120 events per minute to achieve approximately 90 compressions and 30 breaths per minute (International guidelines 2000). The compressions should be to a relative depth one third of the anterior-posterior depth of the chest, as opposed to an absolute depth (International guidelines 2000).

(a) (b)

Figure 16. Infant CPR showing the two-finger technique (a) and the revised recommendation for CPR using two thumbs (b) (Images from Matshes and Lew, 2010)

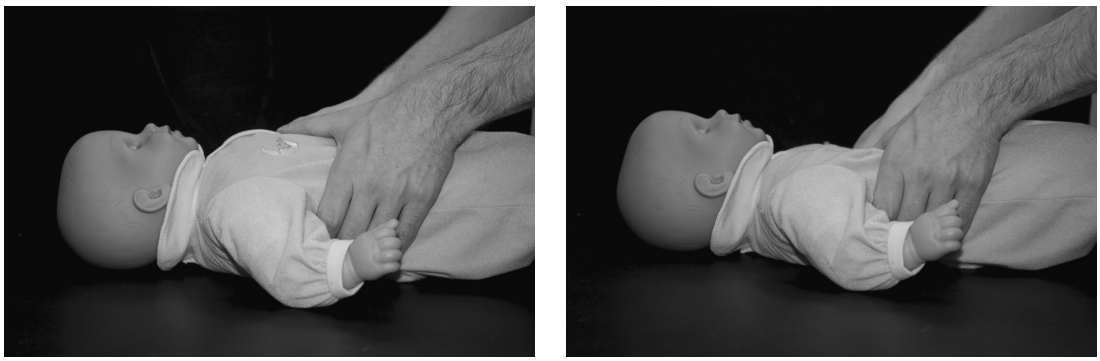

Figure 17. Chest compression during two-thumb CPR (Images from Matshes and Lew, 2010)

The issue of whether CPR in infants causes skeletal chest injuries has been a subject of contention. However it is clear the chest experiences significant compression and as a result strain is applied to the components of the thoracic cage.

Several studies concluded that rib fractures secondary to CPR in children are extremely rare (Bush *et al.*, 1996; Spevak *et al.*, 1994; Feldman and Brewer, 1984). Even when rib fractures were observed in children receiving CPR, they could not conclusively be shown as the sole result of CPR (Feldman and Brewer, 1984).

A retrospective study of rib fractures in infants <12 months old conducted by Bulloch *et al*. (2000) highlighted that of the two infants to receive CPR, neither infant sustained their

fractures during the resuscitation. Independently in 2000, Cadzow and Armstrong went further to state, “It is now recognized that even the mechanical forces used in cardiopulmonary resuscitation do not result in rib fractures in infants.” This lead to a general consensus that in the deficiency of massive trauma or underlying metabolic bone disease, even a single rib fracture must be considered to be indicative of abuse (Cadzow and Armstrong, 2000).

CPR is a traumatic procedure, that involves pressing on the sternum to compress the thorax. Amongst adults it is not uncommon for CPR to cause skeletal chest injuries; a review by Hoke and Chamberlain (2004) found a 13 to 97% incidence of rib fractures, and a 1 to 43% incidence of sternal fractures following conventional CPR amongst adults. Contrastingly, they found the incidence of fractures due to CPR in children to be extremely low, with no sternal fractures recorded, and a range of 0 to 2% for rib fractures.

Possible explanations by this author for the higher occurrence of fractures amongst adults compared with infants in Hoke and Chamberlain's review (2004) are; the greater degree of mineralisation of bone within adults, resulting in a stiffer, more brittle material, and the difference in CPR technique for adults versus infants (heel and palm of hand versus 2 fingers).

In discussing the clinical implications of the likelihood of CPR to cause skeletal chest injuries in infants and toddlers, Hoke and Chamberlain's (2004) conclude it to be extremely rare in children without bone abnormalities. This is due to the inherent elasticity of the normal infant ribcage. They recommend that any incidence of rib fractures in children should raise a strong suspicion of preceding child abuse, and must prompt a full investigation. Furthermore, amongst the studies they reviewed, they highlight that posterior or lateral rib fractures have never been seen in children after CPR, this is a significant statement when related to the possibility of child abuse when observing these injuries.

Maguire *et al*. (2006) reiterated the findings of Hoke and Chamberlain (2004), whilst adding that rib fractures amongst infants are rare when CPR is performed on a hard surface, whether by trained medical personnel or lay persons.

There have been studies that claim rib fractures in infants are the result of CPR, but these fractures were observed in the lateral and particularly ventral parts of the chest, and definitely not the dorsal area unless the bone is diseased or suffering from a preceding trauma (Saternus and Oehmichen, 1985; Betz and Liebhardt, 1994).

Thomas (1977) found rib fractures in posterior parts of infants dying of natural death who underwent resuscitation efforts. But the infants in question showed severe metabolic bone

diseases (bone dystrophy and osteomalazia of extreme premature infants or rickets) which in all likelihood explains the unusual posterior localisation of rib fractures following resuscitation.

A significant result of the Betz and Liebhardt (1994) study was that injuries following resuscitation attempts are, in the overwhelming majority of cases, caused by physicians, rather than non-medical persons. They suggested this as an argument against a possible claim by a suspect that rib fractures were caused by a panicked and inexpert resuscitation attempt by hypothesising that non-medical persons, particularly the parents, are more afraid of causing severe injuries, and are subsequently more cautious when performing CPR.

Prior to the year 2000, the recommended method of CPR for infants was to use the two-finger technique (The American Heart Association). The International Guidelines for Neonatal Resuscitation (2000) issued a change to the guidelines recommended for newly born infants, and older infants. Size permitting, compressions should be delivered using the two thumb-encircling hands technique. The change was motivated by research (David, 1988; Menegazzi *el al.,* 1993) that highlighted the superiority of the two thumb technique over the two finger technique in improving cardiac output and systemic blood pressures.

However, this change in recommendation led to the adoption of a technique that is biomechanically more similar to abusive squeezing,. Matshes and Lew (2010) highlighted the increased likelihood of rib fractures resultant from using the two-thumb technique instead of the two-finger technique.

All of the literature in Hoke and Chamberlain's (2004) review, leading them to dismiss CPR as a potential cause for rib fractures amongst infants, pre-dates the International Guidelines for Neonatal Resuscitation published in 2000.

To the authors knowledge there has been no detailed mechanical assessment, on either infants or a suitable surrogate, of the two-thumb techniques propensity to cause rib fractures in human infants. A mechanical assessment is clearly timely, and would provide valuable information such as the location, frequency, and type of rib fractures resultant from the two-thumb technique.

2.7 Forces and Damage Associated with Abuse

Non-accidental injury (NAI), also known as child abuse, is endemic of modern society. NAI is the result of deliberate and often repeated mistreatment or beating of a child, usually by an individual responsible for its welfare. Child maltreatment in contemporary society can take several forms: physical, psychological, sexual, or negligence. As rib injuries are the focus of this thesis, only a discussion of physical abuse will be presented.

Amongst abused children of all ages, after limb and skull fractures, rib fractures are the third most common type of skeletal trauma (Merten *et al*., 1983). Eliminating all other fractures and looking specifically at rib injuries, there presence within a child is held as a strong indicator of severe trauma. Multiple rib fractures, in the absence of a history of bone disease or major trauma, have been claimed to be highly specific of abuse (Worlock *et al*., 1986). Even a single rib fracture in a child who lacks a history of accidental trauma, unless as a consequence of metabolic bone disease, prompts investigation of abuse.

Rib fractures can be the result of varied methods of abusive trauma delivery, and their location is intrinsically linked to the force, the direction of strain and the type of insult that the child is exposed to. The studies of Cadzow and Armstrong (2000) and Barness *et al*. (2003) illustrate that rib fractures resultant from abuse can, and frequently occur at any location along the length of the rib.

The immature nature of infant bone results in it having a higher plasticity and resistance to fracture, so the forces and mechanical moments required to cause fracture are substantial. Infants under the age of 18 months have a significantly reduced ability for independent mobility (Maguire, 2010). Children in this age group are typically not yet walking abundantly, if at all, so they are far less likely to suffer accidents such as slips, trips and falls that have the potential to provide the necessary factors to initiate a fracture. Older children are more likely to be the victims of motor vehicle collisions, as well as playground or sporting accidents, resulting in fracture rates for accidental reasons providing a much higher percentage amongst older children compared with infants. Therefore the age of the child is one of many factors taken in to consideration when attempting to establish the cause of a skeletal injury.

As previously mentioned, a reasonable hypothesis would be that fractures amongst young children, especially infants, are uncommon due to the plasticity and inherent resistance to fracture of their immature skeleton. However, Leventhal *et al*. (1993) discovered fractures to be common amongst young child and infants, and of all the fractures seen in children less than 3 years old, 24.2% were attributed to abuse. Furthermore, the study by Leventhal

et al. (1993) established 39% of fractures in children younger than 12 months were caused by NAI, but only 8% of fractures amongst children older than 24 months were induced by NAI. This indicates that there is an increased likelihood for fractures seen in younger children to be the result of child abuse as opposed to an unexplained or unintentional trauma. The presence of rib fractures in infants less than 12 months old can go some way to indicating child abuse.

That is not to say that fractures in older children cannot be the result of abuse, indeed fractures due to abuse have been recorded amongst victims in their late teens (Nayak *et al*., 2006). But there is a much higher rate of fractures being the result of abuse amongst younger children, especially in children younger than 1 years of age (Maguire, 2010).

The study of Barness *et al.* (2003) found that rib fracture(s) were the only visible skeletal manifestation of NAI in 29% of the children seen. There have been numerous studies in to whether abused children display a preponderance for fractures in particular locations along the length of the rib (Betz and Liebhardt, 1994; Barsness *et al*., 2003; Cadzow and Armstrong, 2000; Carty, 1993; Kleinman, 1990; Kleinman *et al*., 1988; Kleinman *et al*., 1989; Kleinman *et al*., 1995; Worlock *et al*., 1986). One of the conclusions that all of these studies are in agreement on is that posterior rib fractures are frequently observed in child abuse victims.

However, there are conflicting observations of where else rib fractures due to NAI are frequently seen. Cadzow and Armstrong's (2000) study identifies anterior along with posterior fractures as the most commonplace, whilst Barness *et al*. (2003) document lateral and posterior fractures as the most frequent (see Table 2.).

Site of fracture	Cadzow & Armstrong Study (n=92) (%)	Barness *et al*. Study (n=303) (%)
Anterior	45 (41)	22 (66)
Lateral	13 (12)	35 (107)
Posterior	42 (39)	43 (130)

n=total number of fractures within the study, not number of victims

Table 2. Incidence of rib fractures in abused infants and their relative distribution along the length of the rib

It is clear that the statistical distribution of injuries will be highly dependant on the distribution of differing abusive scenarios within the study population. Carty (1993) observed that lateral and anterior rib fractures may also be result from direct trauma. With

causes such as kicking, stamping, punching or contact with a hard edge when the infant is forcibly thrown away.

Kleinman *et al*. (1988) concluded that most infant rib fractures near the costovertebral articulations occur during episodes of violent shaking with thoracic compression in the anterior-posterior plane.

To make any kind of meaningful analysis of rib fracture location resultant from child abuse it will be necessary to make comparison of victims injured in a broadly similar way. Additionally, greater understanding of rib fractures will be possible if the injury biomechanics are somewhat constrained as a function of the trauma method.

Manual compression of the thorax is generally considered to be the mechanism by which most infant rib fractures are inflicted (Betz and Liebhardt, 1994; Kleinman, 1990; Kleinman et al., 1996; Kleinman and Schlesinger, 1997; Reece, 1993, 2002, Worn and Jones, 2007).

As posterior fractures, especially those near the costovertebral articulations, are frequently seen in cases of child abuse, it makes sense to investigate an injury scenario where this type of fracture is characteristic.

Typically posterior rib fractures resultant from abusive anteroposterior compression of the thorax include fractures to the rib head, rib neck, and posterior arc of the rib (Kleinman *et al*., 1992; Kleinman *et al*., 1996; Kleinman and Schlesinger, 1997). Notwithstanding, fractures resultant from this type of inflicted injury may also occur in the lateral and anterior aspects of the ribs as shown in Figure 18 (Dolinak, 2007).

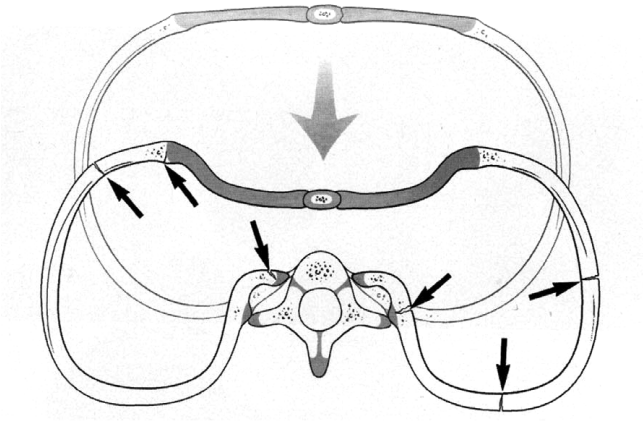

Figure 18. Typical fracture sites in the infant thorax following abusive anteroposterior compression (Kleinman, 1998)

Regarding the abuse of infants, the child is commonly gripped around the chest due to their small size (older, larger children are gripped by the extremities e.g. arms and legs). An adult perpetrator will typically use both hands, with the thumbs positioned on or near the sternum, and the fingers wrapped around the back of the child (Figure 19.). The child is held out in front of the adult, and therefore has no other back support. Regardless of whether the infant is having its torso squeezed, or it is being violently shaken, the thumbs might compress the anterior chest. The lack of additional back support also allows the remaining fingers to directly apply significant force to the posterior rib elements (Matshes and Lew, 2010).

(a) (b)

Figure 19. Anterior grip of an infant in abusive squeezing (a) and the posterior grip of an infant in abusive squeezing (b) (Images from Matshes and Lew, 2010)

If the child is violently shaken, the head oscillates, and the limbs move about in a whiplash movement (Kleinman, 1990). Older children, and infants that are vigorously shaken will display a wider range of injuries to other parts of the body, e.g. metaphyseal, scapular, and central nervous system injuries (Kleinman *et al*., 1988). Damage to the retina is common due to the severe acceleration and deceleration involved. An accumulation of varying injuries gives strong support to a diagnosis of child abuse. However, it is possible that child abuse has occurred even in the absence of multiple injury types, for instance if the infant is squeezed without being shaken vigorously.

The underlying nature of the thoracic anatomy allows for a mechanical theory to the preponderance of posterior rib fractures when the thorax is compressed, particularly fractures at or close to costrotransverse process articulations. As described by Kleinman *et al*. (1988) “Each rib articulates with the vertebral column at two points. The head of the rib articulates with the costal facet of the vertebra anteriorly, and the tubercle articulates with the transverse process posteriorly.”

Within this arrangement the articulation at the transverse process acts as a fulcrum, around which the rib can be levered. The rib can be thought of as a class 1 lever, with the effort being the displacement of the rib body, resulting in a load being generated at the rib head articulation. The rib head is tightly constrained by ligaments, preventing it from moving, with excessive levering of the rib over the transverse process the only way of transferring/dissipating the generated load is for a failure to occur, and the rib fractures at the head or neck.

Anterior-posterior compression applied during abusive gripping and squeezing would generate sufficient leverage to cause the rib to fail mechanically. Kleinman *et al*. (1988) observed that amongst a population of 16 abused infants "...a substantial majority of posterior rib fractures occurred at or medial to the costrotransverse process articulation."

Rigorous laboratory research that characterizes the type and magnitude of force required to cause infant rib fractures is lacking (Boal, 2008; Kleinman, 1990; Lonergan et al., 2003; Reece, 1993).

Without experiments on infants or a suitable surrogate with the ribs in their correct anatomical position within the body, and loaded in a biomechanically representative manner of abuse, it is difficult to categorically state a value for the magnitude of force required to fracture ribs in abusive squeezing. Without knowledge of a threshold limit, it remains subjective as to if an unreasonable amount of force has been applied.

2.8 Techniques: X-ray Radiograpy, X-ray Tomography, Nanoindentation, and FEA

X-ray Radiography

X-ray radiography is one of the oldest and most widely used methods of non-destructive testing. It is also heavily used in diagnostic medicine as it offers the ability to visualise the internal structure of the human body without the need for incision.

The imaging technique works by projecting a beam of X-rays produced by an X-ray generator towards the object of interest. Typically, the X-ray generator is an electron gun that uses a high voltage to accelerate electrons emitted from the cathode towards the target anode, causing the emission of X-rays. Upon arriving at the object, a certain amount of X-ray is absorbed by the object, which is dependent on the particular density and composition of that object. The X-rays that pass through the object are captured by a detector (either photographic film or a digital detector). The detector then collects the resultant 2D shadowgraph, providing a superimposed 2D representation of all the internal structures within the object.

The typical X-ray energies in industrial radiography range from 20 to several hundreds of kV. For medical radiography, the voltage energies range from 20 kV in mammography, up to 150 kV for chest radiography.

There are some limitations to X-ray radiography. Principally that it is not as effective at detecting flaws that are orientated in a planar direction with respect to the radiation source, making orientation of the sample or subject to be inspected key to successful inspection. Also, a radiograph is a projected image (i.e. a three-dimensional object is imaged on to a two-dimensional image) in which each point is a function of the x-rays attenuation through all the features which they have passed. The projected nature of the image results in a loss of depth information, making it impossible to precisely know the location of a particular feature.

These limitations result in the interpretation of radiographs to not be a simple process. Indeed, medical radiologists can only obtain valuable diagnostic information from a conventional radiograph with *a priori* knowledge of anatomy and the normal appearance of the particular anatomical location (Davis and Wong, 1996). The complex arrangement of structures within the human body often lead to regions of interest being obscured, and for a detailed assessment it may be necessary to take several radiographs from a range of angles.

In addition, as X-rays are a form of ionising radiation repeated exposure can pose health and safety risks.

X-ray Microtomography

X-ray microtomography allows the three-dimensional internal structure of a specimen to be determined via a non-invasive technique. X-ray computed tomography (CT) is an extension of conventional radiography. The technique uses X-rays to create cross-sections of a 3D-object that later can be used to recreate a virtual model without destroying the original object. The term *micro* is used to indicate that the pixel sizes of the cross-sections are in the micrometer range.

X-ray microtomography addresses some of the issues symptomatic of X-ray radiography. Specifically, the characteristics of the internal structure of an object including dimensions, shape, defects, and density are readily available from CT images. This makes interpretation of X-ray CT relatively more simple.

The cone-beam XMT system consists of the x-ray source, which produces a cone of x-rays that irradiate the specimen, a two-dimensional detector array to collect the set of projections, and a motorised turntable that rotates the specimen (Figure 20). The specimen is rotated through either 180° or 360° in steps of fixed angular increment.

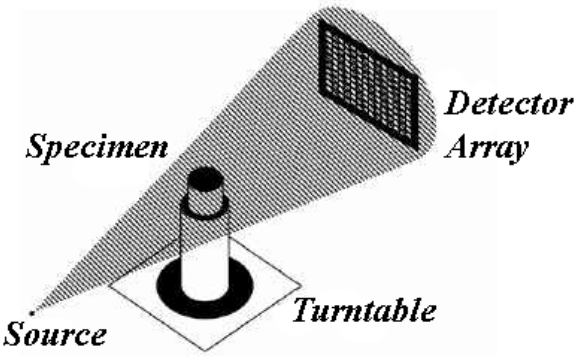

Figure 20. X-ray microtomography experimental setup

Each of the projections (or radiographs) correspond to a map of the transmitted intensities, these directly relate to the density of the different phases of which the sample is composed in accordance with the Beer-Lambert law (see equation below).

$I_x = I_o e^{-\mu x}$

where I_0 = intensity of incident x-ray beam, and I_x = intensity of transmitted beam after passing through a sample of thickness x. The linear absorption coefficient (μ) is dependent on the sample density and the wavelength of the x-rays (Callister, 2003).

By using an appropriate algorithm, such as a filtered back-projection algorithm (Feldkamp *et al.*, 1984; Kak and Slaney, 1987), a series of radiographs can be used to reconstruct the variation of absorption coefficients within the volume of the sample. In other words, creating a three dimensional (3D) map of the X-ray attenuation coefficient of the material (Marrow *et al.* 2004). The 3D map is constructed from cubic elements (called voxels that are analogous to pixels in a 2D image) representing the scanned matter. The grey-level of each voxel indicates the X-ray attenuation at that position within the 3D volume of the sample (Babout, 2006).

Non-laboratory based X-ray CT systems such as those used for medical diagnostics (e.g. CAT scanners), differ from XMT systems as the x-ray source and detector array move around the stationary patient. Despite this difference the two produce essentially indistinguishable data sets.

Nanoindentation

Nanoindentation is a variety of hardness test and a means of testing the mechanical properties of materials with very small volumes. It has evolved from conventional indentation techniques such as Vickers and Rockwell whereby the elastic modulus and hardness of a sample are determined by indenting with another material whose properties are known (Fischer-Cripps, 2002).

In nanoindentation an indenter with a geometry known to a high precision (commonly a Berkovich tip, which has a three-sided pyramid geometry) is used so its contact area can be calculated when it is pushed into the test material. The depth of penetration of the indenter into the specimen surface is recorded as a function of load, and the mechanical properties of the material can be extracted from these load-displacement curves.

Commonly the method proposed by Oliver-Pharr (1992) is used to determine the hardness and elastic modulus of the test specimen from the information obtained during one indentation cycle of loading and unloading (Figure 21).

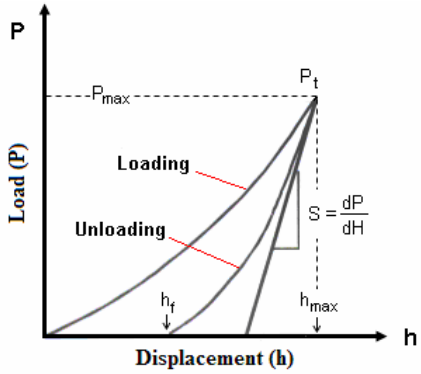

Figure 21. Characteristic load-displacement curve for nanoindentation. Adapted from (Oliver and Pharr, 1992)

The Oliver-Pharr method assumes that deformation of the specimen during loading is both elastic and plastic, whereas during unloading it is assumed that only the elastic part of the displacement is recovered. It is the elastic nature of the unloading curve on which the method is based.

From the load-displacement curves the maximum load (Pmax), maximum displacement (hmax), the final depth (hf), and the elastic unloading stiffness (S=dP/dh) are measured and then used to determine the hardness and elastic modulus of the specimen.

For hardness (H):

$H = Pmax/A$

where A is the contact area, and is determined by assuming the area function for a perfect indenter.

The elastic modulus (S) is measured using the equation below.

$S = dP/dh = (\beta / \sqrt{\pi}) Eeff \sqrt{A}$

Beta being a constant dependent on the geometry of the indenter, and Eeff is the effective modulus which accounts for deformation of both the indenter and the sample.

Finite Element Analysis

Finite element analysis (FEA) is a computational technique that can be used to predict the stress, strain, deformation, heat transfer, fluid flow, etc., of a theoretically loaded structure. Its methodology centres on the representation of a structure as a series of discrete problems that are readily solvable by mathematical analysis (Rayfield, 2007).

The foundations of the finite element method (FEM) lie in mathematical finite difference approximations (Richardson, 1910) and engineering elastic continuum problems (Turner *et al*., 1956). The three key components needed for FEA are computers, matrix method, and the element concept.

Numerous text books are available that explain the mathematical concepts of FEM (cf. Zienkiewicz *et al*., 2005), therefore an in-depth discussion of the theory and mathematical applications of finite elements will not be presented here. Both Richmond *et al*. (2005) and Rayfield (2007) provide thorough overviews of the various stages in the development and analysis of a finite element model. A summary and outline of the salient points now follows.

The underlying premise of the method is to approximate the behaviour of an entire structure or system when subjected to a set of predetermined conditions by subdividing the entire medium into a series of smaller regions, for which the differential equations can be approximately solved. Assembling the set of equations for each region determines the behaviour of the entire structure or system.

FEA comprises of four main steps: generating the model (preprocessing); analysis; visualisation and interpretation of the results (postprocessing); and finally the critical, but often overlooked step of validation.

Firstly a decision is made as to whether the structures geometry can be modelled in one-, two-, or three-dimensions depending on the complexity of the problem as well as the analysts' desire for accuracy and geometric precision. In situations where loading occurs mostly in a single plane, a 2-D model may suffice, and 2-D models have been employed with some success in orthopedic and paleontological problems (Carter et al., 1998; Rayfield, 2004, 2005a, 2007). However when the structure under analysis has a complex and irregular architecture it necessitates modelling in 3D to provide a valid representation of the real structures behaviour.

Once the geometry of the model has been determined it undergoes a process termed meshing, in which the model is split into large number of repetitive units, termed elements. This forms a contiguous mesh in which the elements are connected to each other at nodes. Typically, 3D elements are tetrahedral or hexahedral; the topic of preferred element type depending on the application is discussed by Grosland *et al*. (2009).

Once created, the mesh can be loaded into a physics-based simulation package e.g. Abaqus. Within such a package, material properties (e.g. Young's modulus, Poisson's ratio) determined either from literature or direct material testing are assigned to the element sets. For mechanical analyses boundary conditions are assigned to constrain the model against rigid body movements, and suitable loading scenarios are applied.

The completed model is solved to obtain the nodal displacements and then the resulting stresses and strains anywhere in the whole structure. Following the successful completion of an analysis, each field output is available for interpretation and the results can be displayed in graphs or visualised directly on the structure. This step is termed postprocessing.

Validation is the final, but often crucially overlooked step in FEA. Knowing how accurately the FE-results represent what is occurring in reality is crucial when inferring

any significance in the results. Precision and accuracy are the two chief issues of validation.

Precision is the closeness of the model's results to the exact solution of that biomechanical model (Richmond *et. al*., 2005). The precision of a particular FE model can be assessed through a convergence test in which the model is repeatedly calculated with increasingly finer meshes until the displacement magnitude of a chosen test area reaches a plateau, converging toward a precise solution of that model (Hart, 1989). Being able to use a model with lower mesh refinement, but that is still precise, is beneficial as it minimises computational demand.

However, no matter how finely the structure is meshed and how precisely the calculations are performed, the computed answer may still be wrong (Cook *et al*., 2001). This is down to accuracy, essentially this is how close the model's results are to reproducing the biological reality, and is dependent on the estimation of geometry, boundary conditions, and material properties used. A model would be precise but inaccurate if the mesh is very dense but the loading and boundary conditions are unrealistic.

Once an FE model is validated it is a powerful research tool. It's strengths are the greater ability for explorative research, for example the freedom to load the structure in any way wished and the ability to hold all other parameters constant to see the effect of changing each individual parameter. The methodology also allows for a high degree of repeatability, allowing researchers to quickly learn about a structure or systems behaviour.

Image-based modelling

Image-based modelling is a technique that involves creating computer models based on real geometries that are captured using any modality of imaging. Using particular imaging modalities, such as CT and magnetic resonance imaging (MRI), it is possible to non-destructively capture the internal as well as the external geometry of an object as a 3D dataset.

The image data within a 3D dataset can be transformed into 3D FE models by surface-based or voxel-based reconstruction techniques (van Rietbergen et al., 1995). Voxel-based reconstruction converts each individual voxel into a 3D finite element, generating highly geometrically accurate, but extremely large (in terms of the number of elements) FE models.

With large datasets, such as those generated from high resolution CT, mesh generation is computationally demanding. When meshing a full resolution mesh is not possible due to

computational constraints, steps can be taken in order to still generate a mesh of the structure.

Reducing the resolution of the image data by downsampling results in a dataset with fewer, larger voxels, causing a global reduction in the number of elements needed in the model. However, this can have a detrimental effect on the accuracy of the result if key fine parts of the architecture are lost, ultimately changing the mechanical behaviour of the whole structure. The aim is to strike a balance between the complexity of the model (number of elements), the accuracy of the model, and the speed of the analysis. Depending on the problem, a simple model may yield results not significantly different to a much more complicated model; however analysis times may differ from 5-10 minutes to several days on a desktop machine.

An alternative approach is to adaptively mesh the structure which utilises using elements of different size. For areas with small features, smaller elements are used so that the fine structure is retained. Whilst in bulk areas where the material is generally homogeneous, larger elements are used.

CHAPTER THREE

3 Materials and Methods

3.1 Objective of the experiments

The overarching research question driving this thesis is whether two-thumb CPR can produce the necessary mechanics and forces to produce rib fractures within human infants. If fractures are resultant from this CPR method, they need to be compared for how similar they are to rib fractures that are typically observed following child abuse.

Of specific interest is whether two-thumb CPR has the potential to cause posterior rib fractures amongst infants.

This chapter details a series of experiments to better understand the mechanical behaviour and damage mechanisms of immature ribs when loaded within the thorax as in two-thumb CPR and abusive squeezing. Testing on human tissue was not possible, so tests were performed on a suitable surrogate animal, namely an infant swine model.

This chapter provides an explanation and detailed account of the experimental techniques employed and has been split in to sections detailing:-

- the design and building of a rig to load thoraxes in simulated CPR and abusive squeezing scenarios.
- the preparation of piglet thoraxes for testing.
- X-ray radiography and micro tomography of piglet thoraxes before and after the tests.
- protocols used for classifying fractures with X-ray radiography and micro tomography.
- investigation of the mechanical behaviour of rib tissue and full ribs.
- finite element modelling of sections of rib and full ribs.

3.2 Test Programme to Model the Loads Associated with CPR and Abuse on Infants

Before undertaking a test programme to model and record the loads associated with two-thumb CPR and abusive squeezing, consideration must be given to the limitations and constraints of the experiment.

3.2.1 Limitations and constraints of the experiment

To load the piglet thoraxes in ways representative of both two-thumb CPR and abusive squeezing it is necessary to design an experimental rig. Design of such a rig comes with several limitations and constraints for the experimental method. The principal consideration is a way of supporting the thorax of a piglet so that it does not shift and slide throughout the duration of the test, and so that it is kept in a position in which anterior-posterior compression can be applied. This is made all the more difficult due to the irregular shape of the thorax (shown later in Figure 31) which makes it hard to support and grip with standard experimental fixtures. In addition, a number of thoraxes will be tested, and although piglets of a similar size and weight will be selected, there will inevitably be a degree of natural variability amongst a healthy population which will have to be accommodated.

One of the major differences highlighted between abusive squeezing and two-thumb CPR in the literature review was the difference in support to the posterior of the thorax, this necessitates a way of altering the posterior support provided between the two test scenarios.

Finally, the loads delivered to the thorax during two-thumb CPR and abusive squeezing are applied in different ways. For CPR, the load is administered cyclically, at a fixed frequency, with a specified maximum displacement amplitude. The loading profile for abuse is difficult to characterise due to the huge number of variables involved, so a simplification will be necessary. Anterior-posterior compression due to squeezing by the perpetrators hands is hypothesised as causing the mechanical advantage needed to cause fracture of infant posterior ribs. In its simplest form, this can be thought of as a ramped compression of the thorax upto a maximum displacement, followed by a static hold at this maximum displacement, followed by a release of the thorax.

3.3 The Load Rig and the Application of Loads to the Test Specimens

The load rig was designed to simulate the load configurations associated with CPR and abusive squeezing,

3.3.1 Choice of actuator

A Instron® 5569 materials testing machine was selected as the mechanical actuator to apply loads to the thoraxes. It consists primarily of two electrically driven ball screws which are threaded through a moving crosshead beam upon which is mounted a strain gauge load cell connected to a PC, the crosshead beam is laterally constrained by two guide columns (see Figure 22). This test equipment is designed to evaluate the mechanical properties of materials and components, recording force and displacement to a high level of precision. The ability to control the load application both cyclically, and non-cyclically, makes the equipment suitable for simulating both CPR and abusive squeezing. In addition, the system allows for load regimes to be pre-programmed, offering a high degree of repeatability between tests.

Although hydraulic and pneumatic systems allow for more dynamic load application and therefore offer higher strain rates consistent to those in CPR, the systems available to the author were designed for loading at a much higher range than required, and as such the systems were not able to record the force-displacement with the required sensitivity. The Instron® system has a series of interchangeable load cells which are specifically calibrated to work within different loading ranges, it therefore offers the required sensitivity for the anticipated forces involved.

The dimensions of the Instron® 5569 (Figure 22) offer a working range that is large enough to accommodate both the piglet thorax and a bespoke rig enabling representative loading. The construction and arrangement of the Instron® also allows for specimens to be tested hydrated.

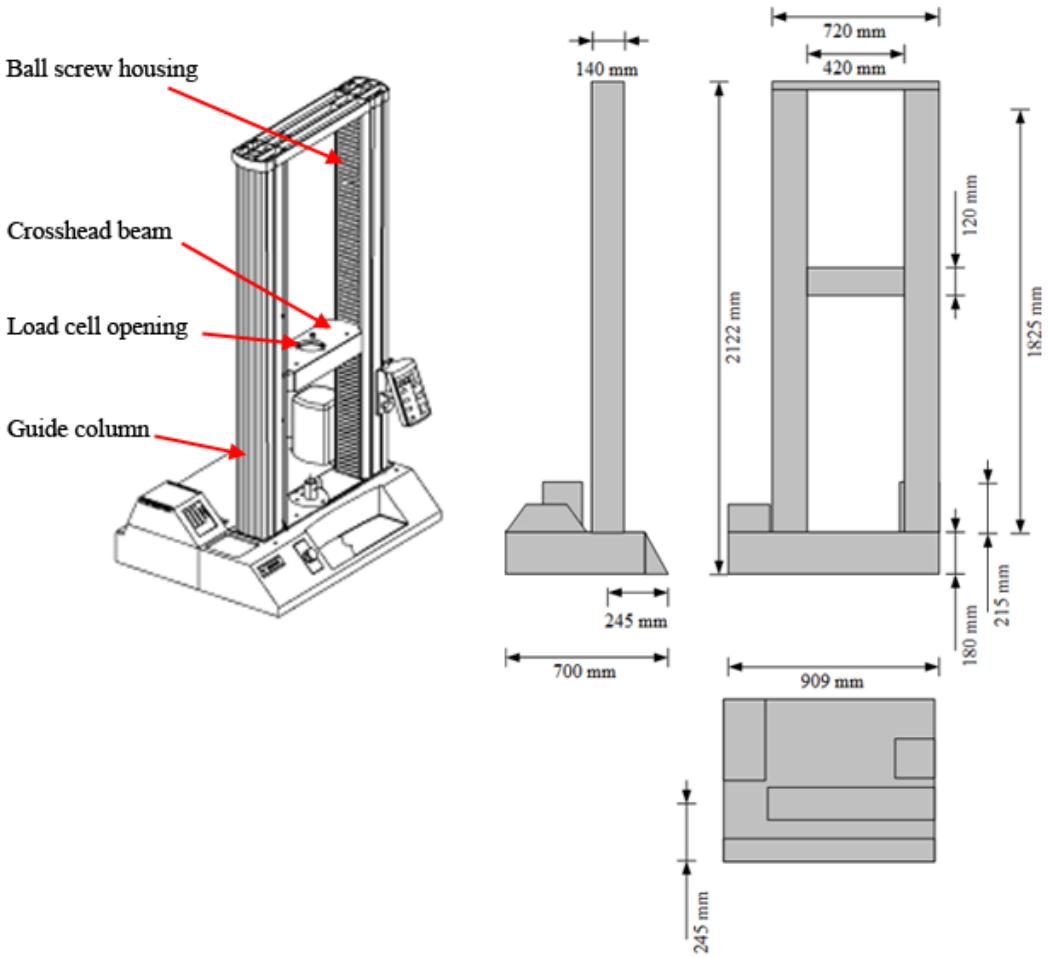

Figure 22. Instron® 5569 schematic

3.3.2 Concept for Rig

The key reason for building a bespoke rig is to allow piglet thoraxes to be loaded in a manner representative of both abusive squeezing and two-thumb CPR. Utilising an Instron system to accurately load and record the forces involved allows a greater degree of control over the testing, whilst also eliminating the variability that may arise from using humans. However, Instron systems are routinely used to perform mechanical tests on man-made materials, these typically having regular shapes and dimensions, and as a consequence the standard grips and fixtures for loading and constraining specimens would not be suitable for the desired tests. Therefore a rig was required that would fit onto the existing Instron system and be suitable for both loading scenarios.

3.3.3 The Build

The final design consists of two main sections to be integrated into the Instron system: an upper section to couple to the load cell, and a lower section to provide lateral constraint and appropriate posterior support to the piglet thoraxes in both loading scenarios. Details of how each of these were built are now provided.

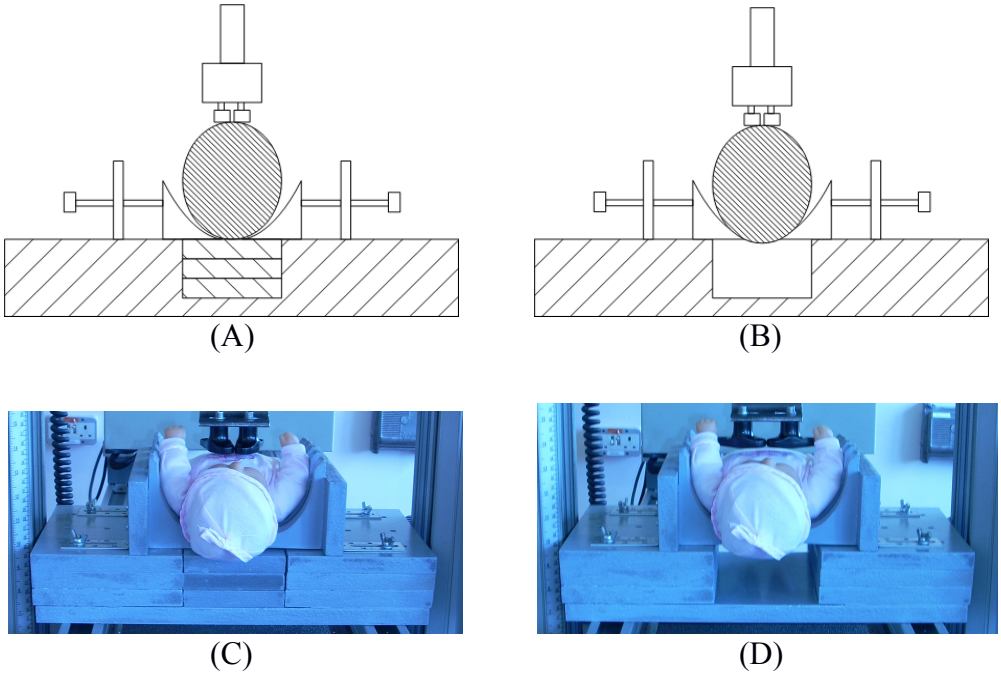

Figure 23. Schematic image of the rig used in the tests to simulate the forces on the ribs due to CPR (A) and abusive squeezing (B). The commissioned load rig with dummy infant inserted is shown in (C) and (D)

3.3.3.1 Upper Section

A portion of steel C-section was machined in the workshop to act as an adapter for a pre-existing coupling for the load cell of the Instron. A threaded hole was drilled in the upper lip of this C-section to receive the thread of the load cell coupling and two slots were routed into the lower lip. Two thermoplastic knobs (RS Component Ltd), with a surface area and shape approximately consistent with adult thumbs (Figure 24), were screwed to the lower lip of the C-section (Figure 25) using socket head cap screws (M6 thread). A rigid plastic was chosen for the "thumbs" so that forces recorded by the load cell were not adversely affected by their compliance.

Dimensions (mm)
A= 60
B= 30
C= 20
D= 25
With an M6 thread

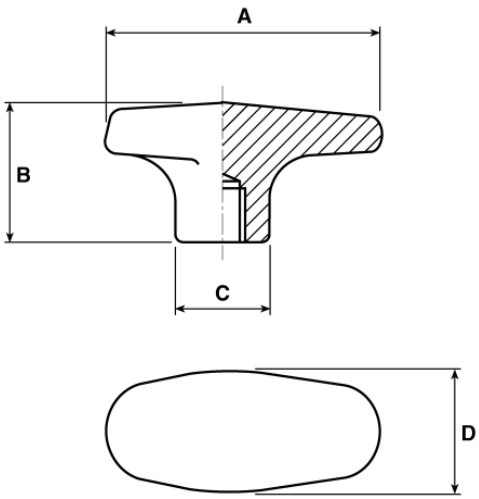

Figure 24. Plastic knob dimensions (http://uk.rs-online.com/web/p/knobs/2670825/)

The entire upper section is made of rigid materials (Figure 25) so that the force recorded from the thorax is transferred directly to the load cell with negligible compliance, therefore ensuring the recorded forces are representative of the force being applied directly to the thorax by the plastic knobs.

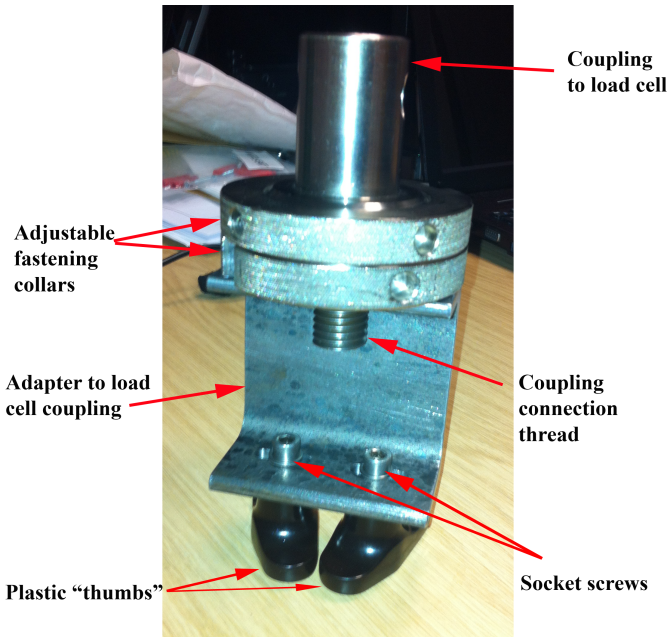

Figure 25. Upper section of test rig for coupling to load cell of Instron

The combination of the slots machined into the lower lip of the steel C-section and the use of socket screws permits the angle of the plastic knobs to be adjusted over a wide range (Figure 26). This allows the plastic knobs to be fixed at angles that are consistent with those in both abusive squeezing and CPR scenarios (see Figure 16b and Figure 19a).

Figure 26. Demonstration of range of motion for plastic "thumbs" when attached adapter for load cell coupling

3.3.3.2 Bottom section

The principle construction material used to build the bottom section of the rig was medium density fibreboard (MDF). Wood was selected as it offers a low cost and its ability to be readily shaped leads to an ease of construction when compared with metals. The elements of the lower section were designed to be principally in compression during testing, so the advantage of metal over wood is relatively slight in materials terms. Further to this, wood can be easily and progressively modified as necessary, allowing for fine adjustments to be made if needed. MDF was selected above other woods as it has an even and consistent density, whilst also having an absence of any grain.

Four identical pieces of MDF were used for construction of the main base for the bottom section. The centre sections of three of these pieces were cut out (and retained), whilst the remaining pieces were secured to the fourth piece with screws.

The moveable lateral constraints were each made of a main MDF piece, to which the MDF rib structures were glued and screwed on one side, and metallic brackets were screwed onto the other side. A template of the cross-section for the rib sections was used to mark up the MDF before it was cut with a circular saw.

Both the sliding parts were positioned on the main base of the bottom section, and marks for the positions of the screws were made. The top two sections either side of the gap were removed, and pilot holes were drilled, the lower of the two sections was countersunk underneath. Both pieces were screwed together from underneath using socket head cap screws, ensuring there was enough thread proud of the top section to act as a guide post for the metallic brackets. Both of the top two sections either side of the gap were then repositioned and re-secured with screws.

The sawn edges of the MDF were sealed with PVA glue before all the exposed MDF surfaces of the construction were spray painted with a waterproofing paint to ensure the

wood did not absorb any biological fluids during testing, thus preventing it from warping and splitting.

Once the elements were sufficiently waterproofed and dry, the brackets of the sliding parts were put on to the screw guide posts and butterfly washers used to secure them.

3.3.4 CPR Test Setup and Loading Regime

The angle between the two plastic knobs was fixed at 5° as shown in Figure 27, this gave a good approximation of the alongside-thumb position used in CPR. The upper section of the rig was then coupled to the 1 kN load cell and the fastening collars tightened.

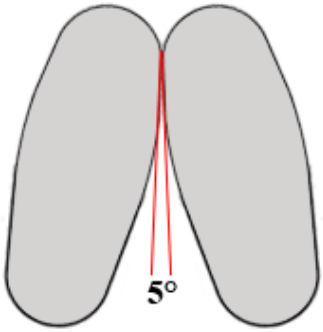

Figure 27. Plastic knob position for CPR scenario

The test setup for the CPR scenario had the wooden blocks in place (Figure 23C), providing the same sort of back support as recommended for infant CPR i.e. lying on a flat, firm surface. The piglet thorax was then positioned with the anterior side of the chest uppermost and the sternum vertically below the plastic "thumbs", ensuring the thumbs would engage with the bottom third of the sternum. When correctly aligned, the lateral constraints were pushed in so as to provide the minimal lateral support needed to keep the thorax in place, and they were then locked in position.

The recommendation for infant CPR is 90 compressions and 30 breaths per minute, giving a total of 120 events per minute i.e. a frequency of 0.5 seconds per event. A cyclic loading regime was created for the scenario using Bluehill® software on the Instron® control PC. This involved three consecutive series of 30 compressions each followed by a 5 second unloaded period, emulating the time taken for 10 breaths. The compressions were set to a depth 1/3 the original anterior-posterior depth of the piglet thorax undergoing testing. The strain rate for loading and unloading was set at the maximum permitted by the Instron®, this being 510mm/min (8.5mm/sec). Figure 28 summarises the key components of the CPR loading regime. Displacement, load, and time data were collected using the Bluehill® software on the Instron® control PC, and this raw data was exported to Microsoft® Excel.

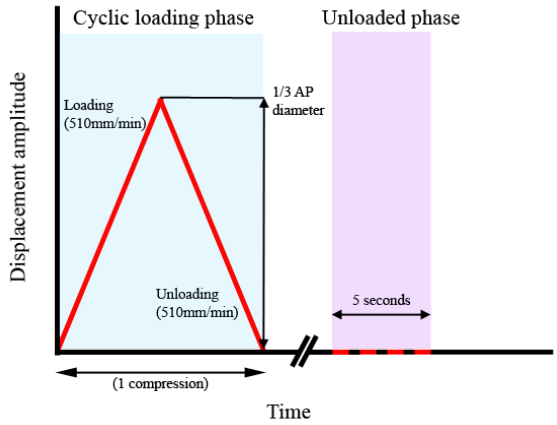

Figure 28. Diagram of displacement amplitude against time for CPR scenario loading regime

3.3.5 Abusive Squeezing Test Setup and Loading Regime

The two plastic "thumbs" were fixed at an angle of 45º for the abusive scenario as illustrated in Figure 29. This angle was chosen as it approximates the thumb position of a perpetrator when encircling and squeezing the chest anterior-posteriorly. Once connected to the 1 kN load cell, the fastening collars of the upper section were tightened to remove any play in the coupling between the two.

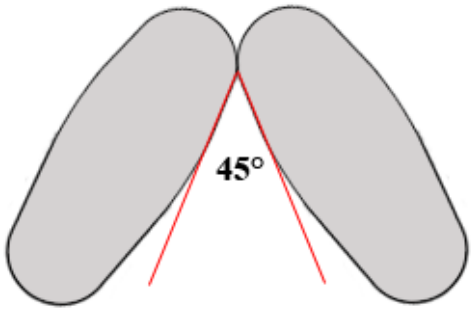

Figure 29. Plastic knob position for abusive scenario

For the abusive squeezing scenario test setup the wooden blocks were removed (Figure 23D) so that the only back support provided was from the wooden ribs of the lateral constraints. Once again the piglet thorax was placed to ensure anterior-posterior compression, with the plastic "thumbs" of the upper section directly above the sternum, the lateral constraints being brought in to provide posterior and lateral constraint to the thorax. Once positioned appropriately the lateral constraints were locked in place.

The depth of compression within abuse is subject to a wide variation dependent on the aggressor, it was decided that thorax would be compressed to the same depth as the CPR scenario so that a direct comparison could be made between the differing posterior constraints and resultant damage to the thorax.

A non-cyclic loading regime encompassing a holding phase was created on the Bluehill® software. This displaced the thorax at the maximum rate of 510mm/min (8.5mm/sec) up to a maximum displacement equivalent to 1/3 the anterior-posterior diameter of the thorax measured before the test started. Once the prescribed displacement was achieved the upper section was held static for a period of time to emulate the specimen being squeezed. Following this the thorax was unloaded at the maximum rate. The key components of the abusive loading regime are summarised in Figure 30. Displacement, load, and time data was logged using the Bluehill® software and then exported to Microsoft® Excel.

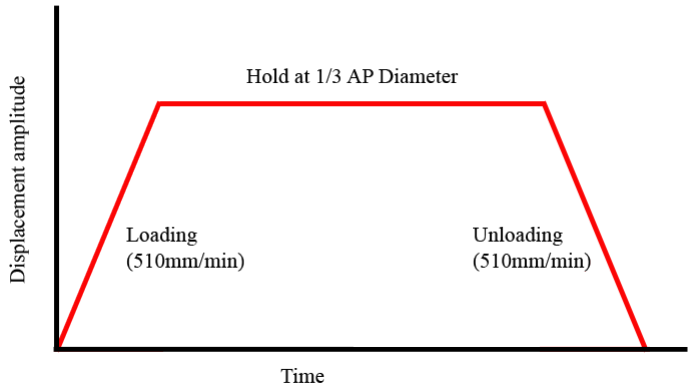

Figure 30. Diagram of displacement amplitude against time for abusive scenario loading regime

3.4 The Test Specimens

3.4.1 Piglet Rib Cage Assessment

Nine *Large White* piglets (*Sus scrofa domesticus*) weighing approximately 7 kg each were purchased from an abattoir specifically for this study. Piglets of this weight were selected as they were approximately six weeks old, making them equivalent to a human infant approximately six months old. All pigs were of good health and had been bred for human consumption. The pigs were sacrificed by abattoir staff using electric shock, they were then stuck (ensuring no damage to the thoraic cage), and bled out.

Delivery of the pigs were coordinated so that three animals per week were delivered over three consecutive weeks (total= 9). This was to ensure that piglets from the same litter were used for specific loading scenario tests, and that differences in condition, specifically bone tissue, were minimised to improve comparative analysis. Three pigs were assigned for CPR scenario testing, and six pigs were allocated to the abusive squeezing scenario.

Pigs were received on the day of slaughter at the Biomedical Services Unit (BSU), Stopford Building, University of Manchester. BSU staff assisted with dissection by removing the head, limbs, outer dermal layer, and the internal organs of the animals. Further dissection and preparation of the thoracic cage was undertaken immediately after by the author. Musculature and ligaments of the thorax were not removed so as to protect and not compromise further the anatomical geometry and biomechanical behaviour (Figure 31).

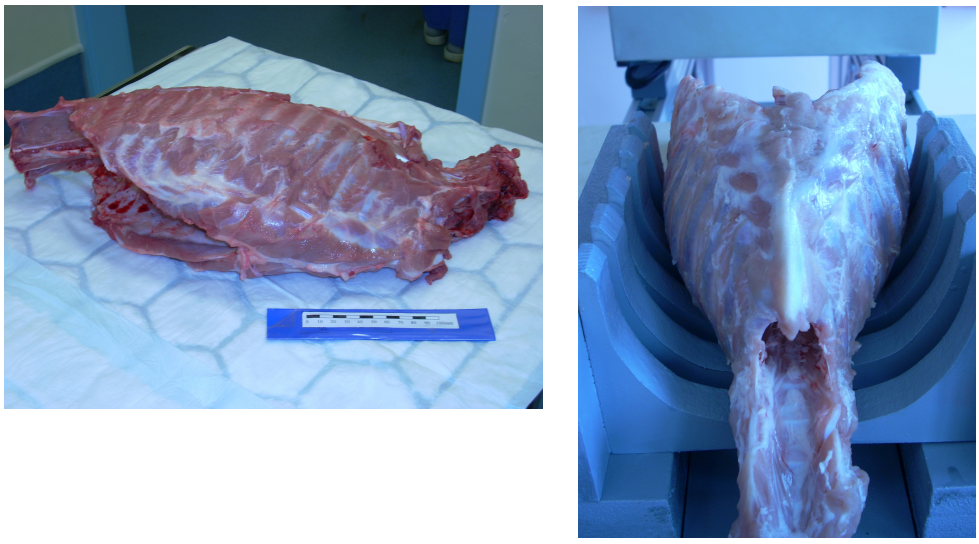

(a) (b)

Figure 31. Typical thorax of a piglet on which the tests were performed (a) when unsupported (scale marker in cm) (b) in-situ within the testing rig

Rib cages were placed individually in resealable plastic bags (ziploc) along with a small amount of simulated body solution (SBS/saline) to prevent tissue from drying out. To further reduce material degradation samples were refrigerated at 4°C when not being tested.

After conclusion of mechanical testing and x-ray imaging, rib cages were stored in a freezer (-20°C) within the BSU to allow for potential histological inspection and material characterisation at a latter date. Storage in this manner has been shown to have negligible effect on the mechanical behaviour of bone tissue (Linde and Sorensen, 1993).

3.5 X-Ray Radiography and Micro Tomography of the Specimens

A discussion of the theory and experimental setup for X-ray microtomography (XMT) were given in the preceding Literature Review chapter.

3.5.1 Piglet Thoraxes Pre and Post Mechanical Testing

Every piglet rib cage was CT scanned before mechanical testing so that any underlying damage was characterised and not wrongly attributed as resultant from the loading scenarios. Pigs were mounted so that their chests were vertically orientated with respect to the source and detector. Orientation of the sample in this way reduces the amount of material the X-ray beam has to pass through, ensuring a wider energy range of X-rays penetrate fully. The resultant improvement to the flux of X-rays reaching the detector allowed the acquisition time necessary for each projection to be reduced, ultimately shortening the length of each full CT scan.

All radiographs and CT acquisition were collected on a 225/320-kV custom lab-based x-ray microtomography system from Nikon Metrology (formerly Metris X-Tek Systems Ltd.). X-rays were generated using a copper target anode and settings were optimised for each specimen within a range of 120-135kV and 114-120 μA. A 0.25 Aluminium filter was used to filter out lower energy x-rays from the spectrum before they reached the sample, as x-rays of lower energy did not penetrate the sample, but did cause saturation of the detector in areas where their path was not interrupted by the sample.

In addition to each CT scan, digital plane radiographs were taken at the four standard angles used to assess the chest within a full skeletal survey of a child suspected to have suffered child abuse. The first of these being posteroanterior i.e. with the subjects chest closest to and perpendicular to the detector (designated as 0º), the second laterally i.e. 90º or 270º with respect to the first scan, and two oblique views positioned at 30º and 330º. Angles were set by using the electronic stage manipulator of the CT system.

All x-ray projections were collected using an exposure time of 708ms, binning set at 1x, a frame rate of 1.41 frames per second, digital gain and gain at 1x and 30dB respectively, and were saved as images in .tiff file format. For tomography scans the Nikon Metrology system usilises a “fast CT” acquisition method, this resulted in the total time for all 3142 projections collected during each individual scan to be just over 37 minutes. The voxel lengths varied in relation to the sample size dictating the source-sample-detector distances, but they were typically within a range of 85-110μm.

A Phantom (Micro-CT HA; QRM, Moehrendorf, Germany) housing five cylindrical inserts containing various densities of CaHA (calcium hydroxyapatite) was placed in the field of view CT during scans of the rib cages. The phantom acts as a reference object and can be used for bone density calibration purposes.

Subsequent to mechanical testing, plane radiographs were taken of each thorax at the standard angles as defined earlier, this was followed by a CT scan with the reference phantom in the field of view.

3.5.2 Piglet Thorax XMT Reconstruction and Data Conversion

Two-dimensional projection images were reconstructed to three-dimensional tomography volume datasets using proprietary software (CT-Pro and CT-Agent) that utilises the filtered back-projection reconstruction algorithm.

Following reconstruction, 3D volumes were imported and converted from 32-bit float data to 16-bit unsigned data using a voxel data visualisation and analysis program, namely VGStudio MAX 2.0 (Volume Graphics). This conversion step considerably reduces the file size (by half), whilst leading to no noticeable difference in image quality when viewed on a computer monitor. In addition, during the import step, the volume area was cropped tight to the specimen surface to further reduce file size. The lowest and highest grey scale values within the volumes histogram were optimised so as to remove background noise within the image, resulting in greater contrast between areas of differing bone density.

Volumes were exported as a stack of tiff images, this being a recognised import format for ImageJ, Avizo, and Simpleware software.

3.6 Protocol for Classification of Fractures

Radiographs and X-ray Microtomography scans for each of the thoraxes from both loading scenarios were inspected for fractures and/or damage to the 5th and 6th ribs, along with the sternal elements to which they attached. Each of the ribs were broadly divided into anterior, lateral, and posterior areas for evaluation.

3.6.1 Radiograph Assessment

The radiographs collected in digital .tiff file format were each imported in to photo editing software (Adobe® Photoshop® CS2 Version: 9.0), individual images were then rotated through 180° to orientate the top of the thorax to the top of the image, and the greyscale values inverted to give the radiograph an appearance in line with medical radiographs.

For each thorax, radiographs taken at the four angles from before the mechanical testing were inspected to check for abnormalities, the absence or presence then being recorded. The corresponding radiographs for each thorax were cross-referenced to help categorise the position of abnormalities into either anterior, lateral, or posterior regions of the ribs.

The same categorisation and recording protocol was used for the radiographs taken after the mechanical testing. These radiographs were first inspected in isolation of those from before mechanical testing, as in a medical setting the radiographer would only have radiographs taken from after any alleged incident. This ensured the classification of fractures was not unduly influenced.

Finally, a direct comparison was made between radiographs from before and after testing in an effort to ensure no fractures or damage had been missed.

3.6.2 X-ray Microtomography Assessment

All the thorax datasets were analysed within ImageJ (v1.47), utilising the ability to inspect the data in all three orthogonal planes. The scans from before mechanical testing were inspected first, with the presence or absence of damage or fractures to the ribs being recorded by location (anterior, lateral, or posterior).

Following this, the XMT scans from after mechanical testing were inspected and any fractures or possible damage categorised in the same manner, along with suitable screen shots being taken and saved in .tiff format.

Finally, a direct comparison was performed between the scans taken from before and after mechanical testing, this was to ensure no fractures had been missed or otherwise wrongly attributed. This step prompted for the datasets from before and after mechanical testing of one of the piglets (piglet 4) to be inspected using Avizo. This involved selecting threshold

values suitable for the bone of the ribs to enable a 3D rendering, which subsequently allowed detailed inspection of the posterior of the ribs, and suitable images were taken.

3.7 Rib Bone Mechanical Behaviour

The purpose of the work within this section was to allow comparison between tissue, individual rib, and whole rib cage bone behaviour. This would later inform and aid in finite element modelling of increasingly more complicated bone mechanical behaviour by beginning with modelling bone tissue, then full bones, and ultimately the modelling of full rib cages.

Due to the limited amount of rib material available this work was done in partnership with undergraduate student Maryam Shokouhinejad and masters student Thomas Howard.

3.7.1 Mature Pig Ribs

3.7.1.1 Specimens

Bone used in this study was obtained from fully mature porcine ribs. Mature rib was chosen as it has a comparable architecture to immature bone, but being fully mineralised it has less material variability. Further to this, rib bone from adult pigs has been characterised within the existing literature, allowing comparison of the material properties measured using nanoindentation.

The ribs were sourced from a local butchers, and kept refrigerated at 4-6°C until use. The ribs were removed of all soft tissue, including the periosteum, and repeatedly washed in distilled water to leach out blood from the internal trabecular regions. The ribs were then left for a period of one week to dry out.

Five 5 mm transverse sections were from a single rib using a wet abrasive cutting machine (ATM Brillant 221). Specimens were sanded with fine silica paper to ensure the cut faces were parallel.

Following CT scanning, one of these 5mm sections was further prepared for nanoindentation. This involved embedding the section in a non-infiltrating cold set polymer resin, then the specimen was first ground with silicon carbide papers of increasing grades of fineness, and then polished on soft cloths embedded with 1 μm and 0.25 μm diamond paste.

3.7.1.2 Mature Rib Tomography & Reconstruction

All five 5mm bone sections were imaged in a single CT scan by the author using a 225/320-kV custom lab-based x-ray microtomography system from Nikon Metrology. Proprietary software (CT-Pro and CT-Agent) that utilises the filtered back-projection reconstruction algorithm was used to reconstruct data, and the volumes were exported as a stack of tiff images. The voxel size was 0.0248 mm.

3.7.1.3 Mature Rib Mechanical Testing

A simple compression test on one of the 5mm sections was performed on a materials testing machine (Instron® 5569). The load was applied perpendicular to the cut surfaces of the specimen. The recorded load-displacement data was corrected to account for the compliance within the testing machine.

3.7.1.4 Nanoindentation

The nanoindentation tests were conducted with guidance by the experimental officer responsible for the equipment (Andrew Forrest), with standard protocols being followed.

3.7.2 Immature Piglet Ribs

3.7.2.1 Specimens

Five pigs (sus scrofa domestica) aged 16-20 weeks were harvested humanely by a 10cc injection of phenytoin from the University of Manchester Biological Support Facility, UK. The pigs were primarily harvested for cardiac research leaving the right rib cage available. They were bred for human consumption and were not administered anything that might adversely effect their bone quality.

3.7.2.2 Sample Preparation

Each rib bone was freed from the spine and costal cartilage, soft tissue was dissected away leaving only the periosteum. The ribs were immersed in 0.9% phosphate buffered saline (PBS) and kept in a fridge at 4°C or frozen until required for use as is recommended (Turner & Burr, 1993). Twenty-six dissected rib bones were taken from the prepared stock of 16-20 week piglets.

3.7.2.3 5mm Sections for Compression Tests

5mm sections were cut firstly by hacksaw and then ground and polished using increasingly finer grades of silicon carbide paper. Machining 5mm sections was deemed unsatisfactory for two reasons. Firstly, due to the curvature of ribs, it was difficult to clamp the ribs in a position that was reliably square to the cutting blade. Secondly, gripping ribs in the vice needed to be near the cutting line causing unacceptable damage to the bone.

3.7.2.4 Full Ribs for Anterior-Posterior Loading

No further sample preparation was undertaken for these samples.

3.7.2.5 Immature Rib Tomography & Reconstruction

All prepared samples were CT scanned prior to material property determination and mechanical testing. The same x-ray machine and reconstruction software used for mature rib samples was used for the immature rib samples.

3.7.2.6 Nanoindentation

Six samples were selected for nanoindentation, and were prepared and tested. Due to the wet testing cell being out of commission, testing was performed on dried bone samples. Between 25 and 45 indents were performed per sample. Overall, roughly half the indents were aimed on trabecular bone, and the other half on cortical bone. Ten indents were performed on resin to aid dismissing indents that failed to hit bone. Analysis of results was performed with assistance from the experimental officer (Andrew Forrest).

3.7.2.7 Mechanical Testing

5mm Section Compression Tests

Compression tests on a series of the bone sections were performed using an Inston® 5569. Samples were kept hydrated in a saline solution prior to testing. The load was applied perpendicular to the cut surfaces of the specimen, with the load-displacement data recorded to the control PC of the testing machine.

Full Ribs for Anterior-Posterior Loading

Compressive tests representative of anterior-posterior loading on whole immature ribs were performed. The ribs were kept in place using a pair of grips purpose built for the Instron® 5569 materials testing machine (Figure 32). The load-displacement data was recorded to the Instron® control PC, and the raw data saved to Microsoft Excel files.

Figure 32. Immature rib whilst in test rig (picture courtesy of Tom Howard)

3.8 FE Modelling

Finite element analysis provides an alternative research technique to investigate structures that cannot be tested directly, such as the human infant thorax. A crucial aspect of FE analysis is validating models against physical tests. As suitable human infant data for such tests is not available, the human model can be based on an FE model of a suitable surrogate validated against physical tests. By studying the effects on the surrogate model, it is possible to increase our confidence in the results of human FE models without having to conduct direct physical testing on human infants. This section details the development of FE models for sections of rib, and whole individual ribs.

A mature rib section was modelled first as it had a comparable architecture to immature bone, but being fully mineralised has a more consistent tissue behaviour than the developing immature bone of piglets. This section also documents attempts to model immature bone, specifically rib sections and full ribs sourced from piglet material. The experimental data collected from techniques described in section 3.7 was used as to generate the finite element meshes, as input for elastic modulus, and as a method of validating the resultant analyses.

3.8.1 Mature Pig Rib

3.8.1.1 FE Model Generation

The height of the sample was measured as 6.2mm. Scan data was resampled to 25% of the original resolution to speed up computational time. The resultant geometry of the rib section constructed from high resolution CT scanning had a voxel size of 0.0992 mm.

Following import to Simpleware software an automatic segmentation was applied using a threshold range suitable for the mature bone. Nodal surface sets were generated for the upper and lower faces of the bone section to aid constraining the model in the analysis step. Use of the automated tetrahedral meshing algorithm allowed the mesh to represent the trabecular and cortical morphology of the entire bone section. The FE model was generated and exported from Simpleware in .inp file format.

3.8.1.2 FE Analysis

Using Nanoindentation data as input

Following import of the model to the finite element analysis solver Abaqus, a simple compression test was set up, in which the bottom surface nodes were locked, and the top surface nodes were allowed to be displaced in the vertical direction only. FE simulations of the mature rib section were first run using Young's modulus values obtained from nanoindentation (12 GPa), and a Poisson's ratio of 0.3 was assumed. Elastic material

behaviour was assumed. Displacements were calculated from the samples height of 6.2mm to cause % strains of 0.5, 1.0, and 2.0. Reaction forces were measured nodally on the upper most surface of the rib section and summed for the whole surface.

Using Calculated Modulus

Young's moduli for test samples with a regular cross-section can be calculated automatically by the Bluehill software that is used to operate the Instron testing machine. The initial linear slope of the force-displacement graph is converted to a stress-strain plot, and the materials modulus is then calculated by dividing the stress by the strain.

$$E = \frac{stress(\sigma)}{strain(\varepsilon)} = \frac{(Force / Area)}{(Extension / Original\ length)}$$

$$Where\ E = Young's\ modulus$$

The irregular cross-section geometry and porous nature of the bone specimen meant that automated stress-strain plots could not be produced using the Instron software. In order to find the stress value through a plane in the middle of sample, the cross sectional area was calculated by using statistical information measured from a CT scan of the sample before it was tested using the computer program ScanIP.

A cross-sectional volume 1 voxel in height was selected at approximately midway down the sample (Figure 33). Statistics from ScanIP revealed this volume measured 5.04mm^3, and dividing this by the height of 1 voxel (0.0992mm) gave a cross-sectional area of 50.81mm^2. Dividing the experimentally measured force values by this cross-sectional area resulted in an approximate stress value through the midplane section (Table 3).

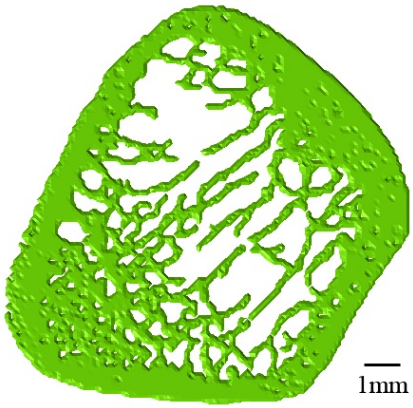

Figure 33. Selected cross-sectional volume from mature rib section

Force (N)	*Displacement (mm)*	*Stress (MPa)*	*Strain (%)*	*Strain (ratio)*
0	0	0	0	0
2840	0.062	55.89	1	0.01
5410	0.124	106.47	2	0.02

Table 3. Calculated stress-strain values for mature rib section

Plotting this stress-strain produces a graph (Figure 34) representing the linear elastic behaviour of the rib section. The slope of this graph represents the Young's modulus of the mature bone material, and measures 5.32 GPa.

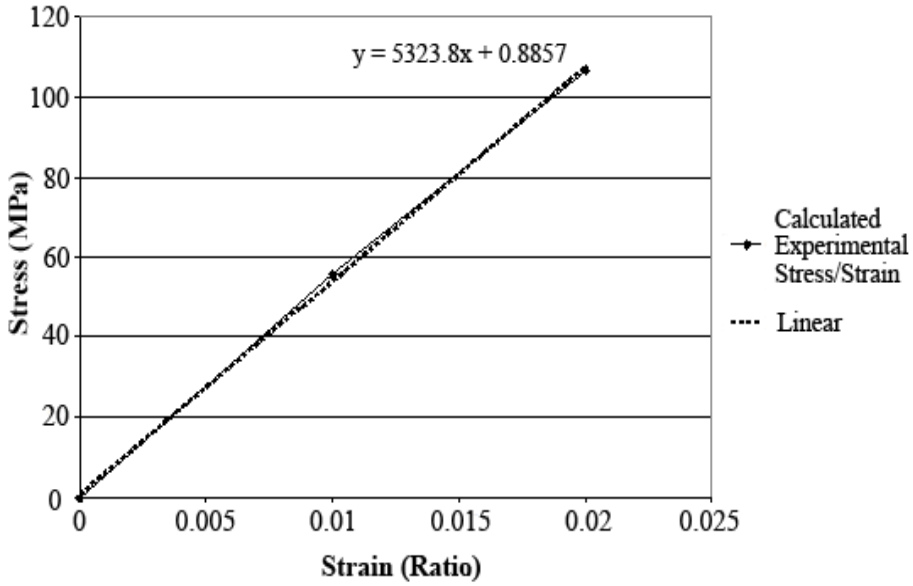

Figure 34. Calculated linear-elastic (stress-strain) behaviour of mature rib section

FE simulations using the calculated modulus of 5.32 GPa and a Poisson's ratio value of 0.3 were run to predict the bone sections elastic behaviour at the following strain percentages, 0.5, 0.75, 1.0, 1.5, 2.0.

3.8.1.3 Sensitivity Analysis of Model to Meshing

A series of simulations were run to investigate the effect of increasing the FE model resolution on reaction force and stress measurements. The same mature pig rib section image data was used to create several series of FE models with increasing resolution. The 100% image data was downsampled within ScanIP to create a series of lower resolution data sets, and within each of the new data sets the thresholding tool was utilised to create a mask for the bone.

The **+FE Grid** meshing method was used for the first model series, using the 1x1x1 setting to create all tetrahedral meshes in which every side of the element is the same length, and is based on the voxel size of the data set i.e. more heavily downsampled datasets will have larger voxel sizes, and therefore fewer, larger elements.

Subsequent model series were created using the **+FE Free** meshing method set at 0 and -50 compound coarseness (cc) to produce fully tetrahedral meshes. At the zero setting the surfaces are not remeshed but simply taken from the **+FE Grid** mesh and the interior volume filled using the free-meshing approach; this increases the size of elements within the bulk volume. At -50cc the extracted **+FE Grid** mesh is remeshed using the +FE Free meshing algorithm. This typically keeps/creates small elements at small features, but decimates the triangular mesh away from these regions. The remeshed surfaces are then filled with tetrahedral elements, and the interior volumes filled using the free-meshing approach.

The FE model series were all run with the same boundary and loading conditions as before, but only for 1% strain values. The final series was run with a modulus of 11 GPa, rather than 12 GPa, so that the effect on the results could be assessed.

3.8.2 Immature Piglet Rib

3.8.2.1 FE model generation

5mm Section Compression Tests

First, a CT scan of one of the 5 mm immature bone sections was imported into Simpleware software. The data was downsampled to 10% to ease manipulation of the data on the workstation used, and to speed up subsequent simulation times. A threshold selection was performed to generate a mask of the bone, and a pair of platens were painted in using Simpleware image editing tools. Node surface sets were generated for the upper surface of the top platen, and the lower surface of the bottom platen. Contact pairing were stipulated between the nodes of the bone touching either platen before the model was then meshed using **+FE Grid** and exported in .inp format.

Full Ribs for Anterior-Posterior Loading

The corresponding CT scan for one of the whole ribs to be tested was imported to Simpleware software and downsampled to 10%. Threshold selection created a mask for the entire rib, and this was meshed using the **+FE Grid** meshing algorithm applying the 1x1x1 setting to create a fully tetrahedral mesh in which all the elements were the same size. The data was exported in .inp format.

3.8.2.2 FE analysis

5mm Section Compression Tests

Input properties for bone were informed from nanoindentation (3.7.2). Elastic material behaviour was assumed. Displacements were applied to the upper most platen to produce strains of 1% and 2% within the bone section. The node set of the lower platen was fixed in all directions and all rotations. Reaction forces were measured and summed within Abaqus.

Full Ribs for Anterior-Posterior Loading

The bone properties were again taken from the recorded nanoindentation values. Surface node sets for upper and lower rib constraints were manually selected within Abaqus. The bottom node set was assigned constraints so that it was fixed in all directions and rotations. A nominal displacement was prescribed to the upper node set as this was merely a feasibility check that firstly a whole rib could be modelled, secondly that a solution was reached, and finally that the simulation ran with the broadly expected gross behaviour.

CHAPTER FOUR

4 Results of the Experiments

4.1 Load Testing Results of Piglet Thoracic Cages

Presented in this section are the load and displacement data recorded during the mechanical tests of full pig rib cages for both CPR and abusive simulations.

4.1.1 CPR Scenario

Mechanically simulated CPR was successfully carried out on three pig thoraxes and the force-displacement data detailing the thoraxes response over the duration of the full ninety compressions was recorded. This data is now presented below in graph form along with photographs displaying relevant injuries and damage to the ribs observed during the testing.

Pig 4

Figure 35 presents the force-displacement curves for the first five compressions delivered to the thorax of pig 4. The displacement value is the relative position of the artificial thumbs, 0 mm being an absolute value corresponding to the thumbs just touching the sternum of the thorax before the first compression, and the maximum displacement being the point at which the thorax is compressed by 1/3 the original anterior-posterior diameter. The force measured corresponds to the reaction force provided to the artificial thumbs by the thorax. For each compression the loading portion is the top curve and the unloading region is the bottom curve.

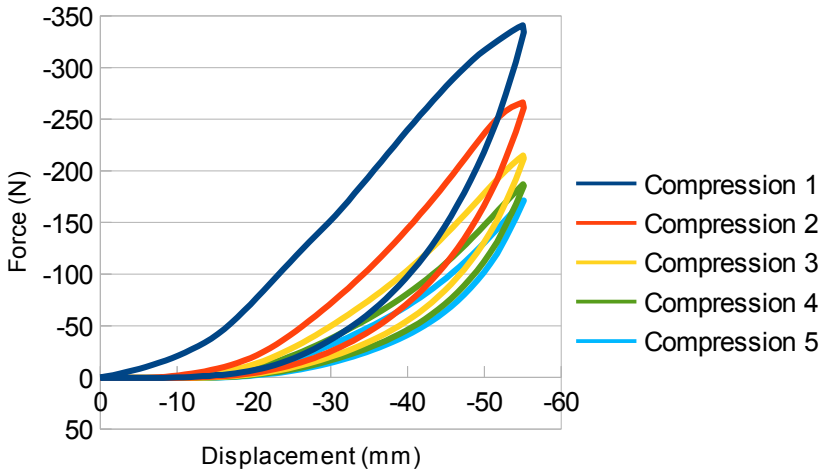

Figure 35. Graph of force-displacement curves for first 5 compressions during CPR simulation on Pig 4

The loading and unloading curves form a series of hysteresis loops, with the loading phase of the thorax consuming more energy compared to the unloading phase, characteristic of viscoelastic behaviour. The first compression required the largest force to displace the

sternum to the target depth, and the hysteresis loop was the largest of all the compressions. As the thorax continued through its loading and unloading the amount of energy lost per cycle decreased, and the amount of force needed to reach the target displacement decreased. After the fifth cycle the peak force and hysteresis continued to decrease but not as dramatically making it hard to pick out the different compressions because they overlapped (they are not displayed in Figure 35 for this reason). Figure 36 shows how the peak force per compression decreased with increasing cycles, tending towards an equilibrium value of close to 100 N. The difference in reaction force from the first to the last compression was 238.9 N (341.2 N – 102.3 N), with each compression taking 12.95 seconds.

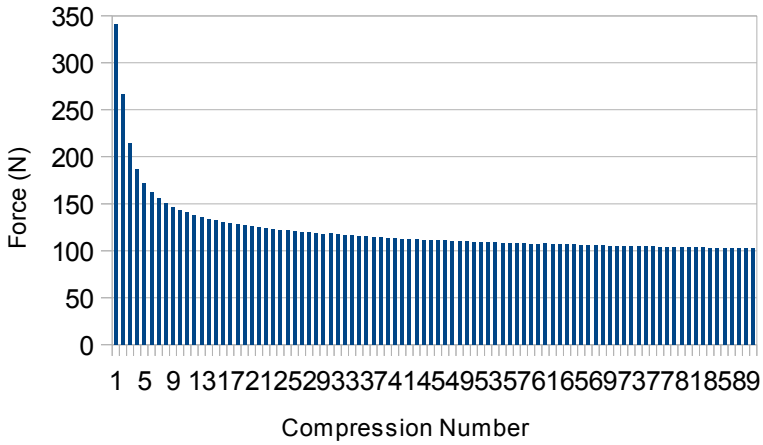

Figure 36. Graph of peak force during each compression throughout CPR simulation for Pig 4

Following the 5 second pauses in which compressions were withheld to simulate a rescuer delivering breaths during CPR, the thirty-first and sixty-first compressions required marginally higher peak forces (+0.6 N) than their respective preceding compressions, indicating some recovery took place during this period.

Pig 5

The force-displacement curves for the first five compressions delivered to the thorax of pig 5 are presented in Figure 37. Loading and unloading took a total time of 12.48 seconds for each compression. The peak force throughout the entire test was recorded in compression 1, measuring 295.96 N and occurring at maximum displacement of the thorax.

The loading and unloading curves formed a series of hysteresis loops similar to those seen in pig 4. The loading curve for compression 1 whilst initially smooth exhibits a degree of disruption beginning at 23 mm, before returning to a smooth profile. The loading curve for compression 2 also displays some noise before taking on a smooth appearance. As with pig

2 the hysteresis loops closed up as more compressions were applied, showing the amount of energy lost per compression decreased as the test progressed. This is coupled with a decrease in the force required to attain the target displacement of 53 mm for successive compressions.

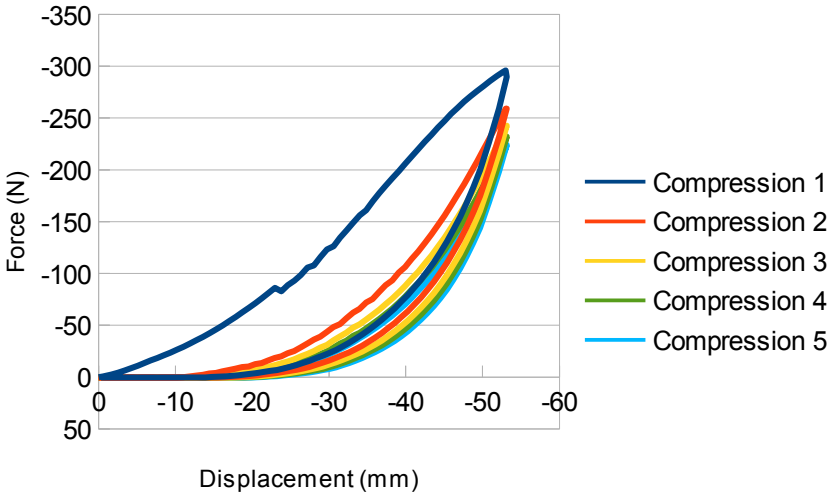

Figure 37. Graph of force-displacement curves for first 5 compressions during CPR simulation on Pig 5

Figure 38 displays the overall decrease in peak force recorded during the 90 compressions, with the greatest drop off exhibited in initial compressions and then tending towards an equilibrium value close to 150 N. The difference in peak force between compression 1 and compression 90 was 142.2 N (296 N – 153.8 N). As with pig 2, the thirty-first and sixty-first compressions showed a slight increase in force compared to their preceding compressions (0.5 N and 1.0 N respectively), indicating time dependent recovery of the thorax.

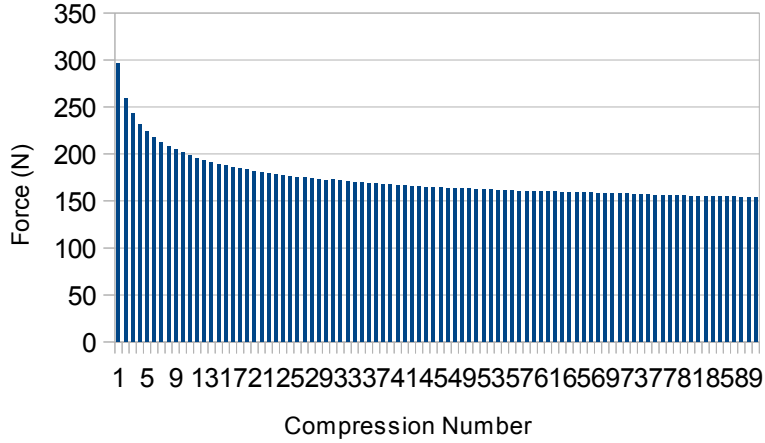

Figure 38. Graph of maximum force during each compression during CPR simulation for Pig 5

The photographs in Figure 39 were taken during the testing and show damage that was visible with the naked eye. Figure 39a shows evidence of a lateral fracture to the left rib 4

as indicated by the red arrowhead, as well as a fracture or damage to the sternal end of left rib 5. Figure 39b and Figure 39c show bleeding that was visible externally in the region of sternal rib extremities and sternal cartilage interfaces of left rib 5 and right ribs 4 and 5.

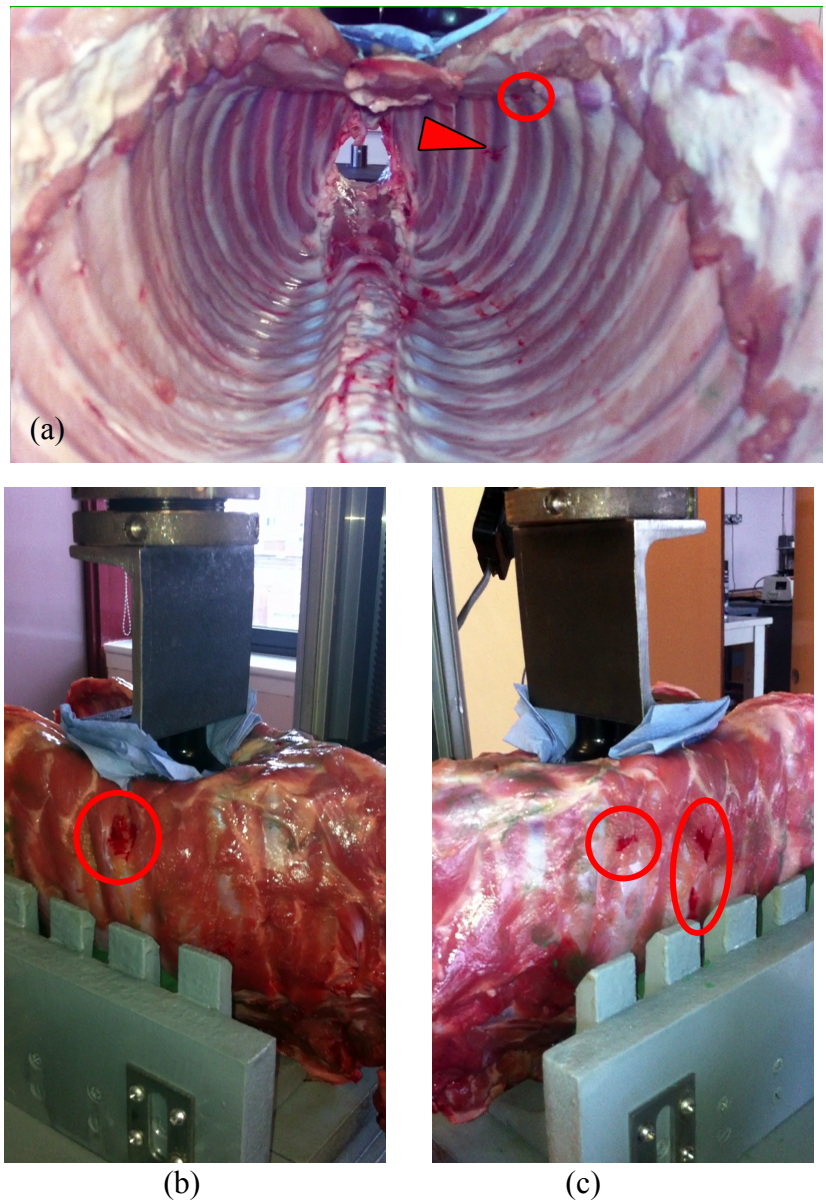

Figure 39. Photographs of Pig 5 thorax during CPR scenario mechanical test (a) internal view with spine inferior to sternum: red arrowhead indicating fracture to left rib 4, left circle damage to sternal end of left rib 5 (b) exterior view: red circle denotes a bleed from left rib 5 (c) exterior view: red circle highlighting bleed to right rib 4, red oval indicating two bleeds eminating from right rib 5

Pig 6

Force-displacement curves for the initial five compressions performed on pig 6 are shown in Figure 40. Compressions took between 12.0 and 12.1 seconds throughout the entire test. The peak force for the whole test was measured during compression 1 (305.84 N at 47.6 mm). The loading curve for compression 1 rises in a smooth non-linear fashion until a displacement of 46 mm, at which point the curve flattens, with no further significant increase in reaction force until the target displacement of 51.5 mm is reached.

Apart from the first compression, all hysteresis loops throughout the test had smooth non-linear loading and unloading components. The hysteresis was greatest for the loading and unloading curve of compression 1, with the subsequent four hysteresis curves tightening up and beginning to overlap.

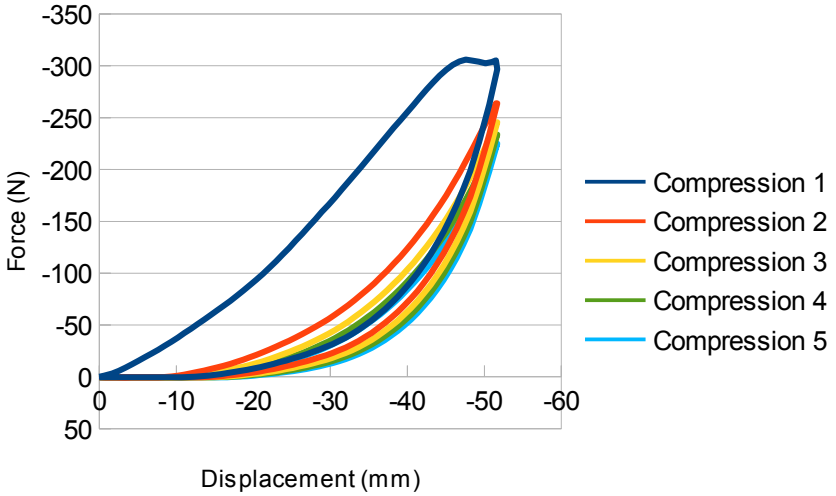

Figure 40. Graph of force-displacement curves for first 5 compressions during CPR simulation on Pig 6

As with the previous two thoraxes, the force required to reach the target displacement decreased non-linearly over time (Figure 41), tending towards an equilibrium value of around 150 N, the greatest drop-offs being seen in the initial compressions. The difference in peak force between compression 1 and compression 90 was equal to a drop of 153.25 N (305.84 N – 152.59 N). Following the 5 second pauses in which loads were withheld, the forces required for the thirty-first and sixty-first compressions were respectively 0.5 N and 0.9 N higher than their preceding compressions.

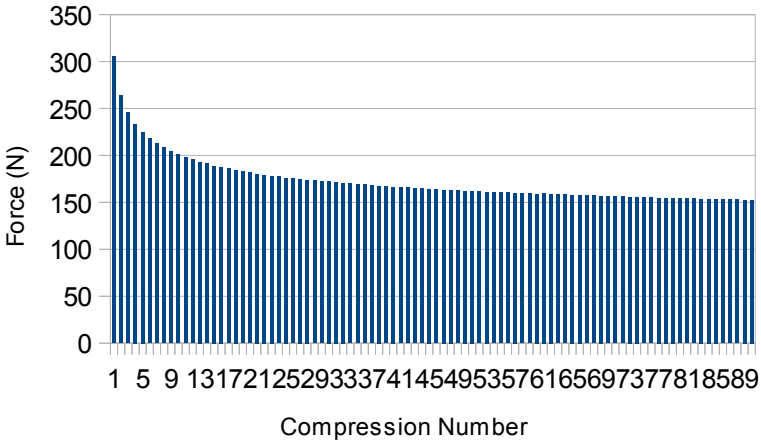

Figure 41. Graph of maximum force during each compression during CPR simulation for Pig 6

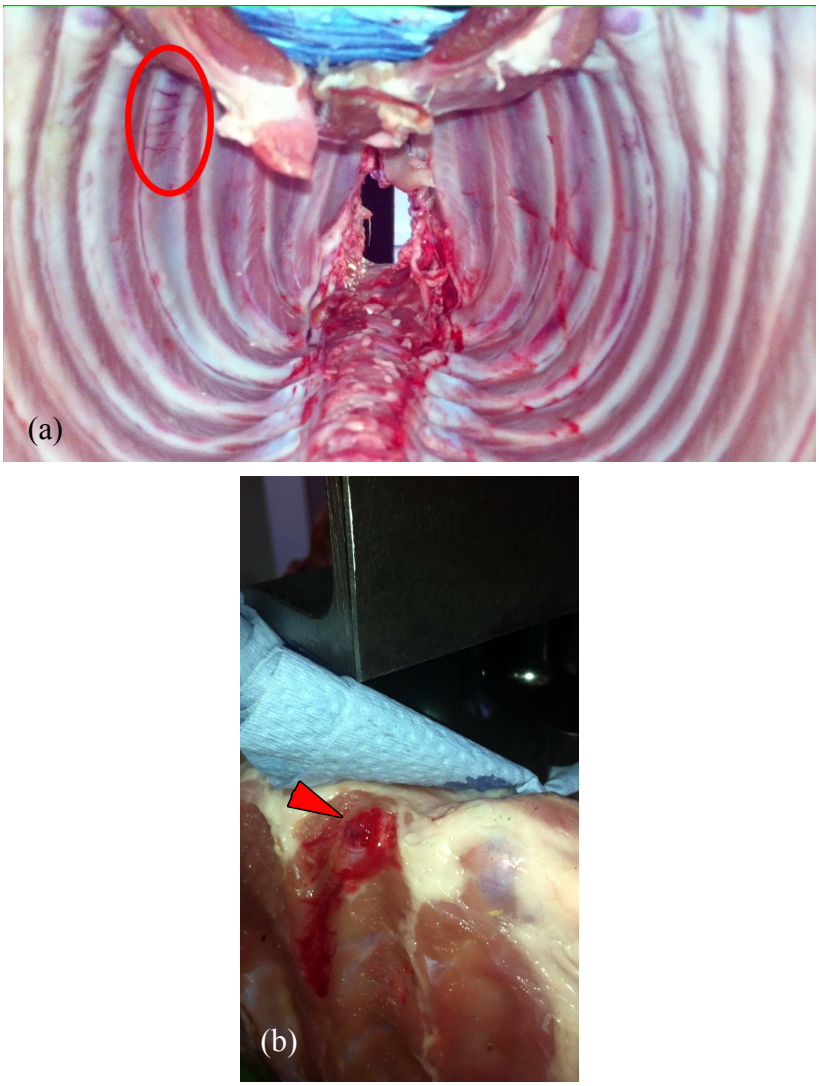

Figure 42. Photographs of Pig 6 thorax during CPR scenario mechanical test (a) internal view with spine inferior to sternum: red oval indicating multiple lateral fractures to sternal end of right rib 4 (b) external view: red arrowhead highlighting costochondral failure to left rib 5

The red oval in Figure 42a highlights the crushing damage seen in the sternal end region of right rib 4 of pig 6, exhibited as a series of roughly parallel fracture lines running transverse to the long axis of the rib. The red arrowhead in Figure 42b points to the partial failure of the costochondral joint for left rib 5.

4.1.2 Summary of CPR Mechanical Tests on Piglets

Figure 35, Figure 37, and Figure 40 are force-displacement curves for the first five compressions recorded on pigs 4, 5, and 6 respectively. A general trend true for each of these is that the first compression requires the greatest force to reach 1/3 AP diameter, following which each subsequent compression requires less force than the previous one, with the difference between subsequent compressions reducing as the tests went on. Initial compression for pig 4 exhibits a smooth curve, whereas by comparison pig 5 has some noise between -20 and -30mm of displacement, and pig 6 has a plateau in the force prior to reaching the displacement of 1/3 AP diameter. Table 4 summarises the peak forces measured during mechanical CPR simulations.

Pig	*Peak force (N)*	*Displacement at peak force (mm)*
4	341.20	55.00
5	296.00	53.00
6	305.10	51.50

Table 4. Peak forces and displacements for mechanical CPR simulations on pig rib cages 4-6

4.1.3 Abusive Scenario

Of the six rib cages prepared for testing with the abusive scenario, five were successfully tested. The first rib cage was used to calibrate the loading rig and the results were not comparable with the other rib cages. Force-displacement curves are now presented along with photographs displaying relevant damage or fractures to the ribs of each pig thorax.

Pig 2

Figure 43 presents the force-displacement profile for the abusive simulation imparted on pig 2. The loading curve initially has a rising non-linear profile, followed by a rising linear region, before levelling off in a non-linear fashion until the target displacement was reached. The peak load recorded throughout the entire test protocol was 334.52 N and was measured as the displacement reached its maximum (46.75 mm).

Throughout the holding portion of the test the sternum is held stationary, depressed by 1/3 its anterior-posterior diameter (46.75 mm) for a period of 1 minute. The reaction force at the end of the hold was 156.92 N, meaning the resultant drop off in load over duration of the hold was 177.6 N. Subsequent to this, the unloading curve followed a falling non-linear path.

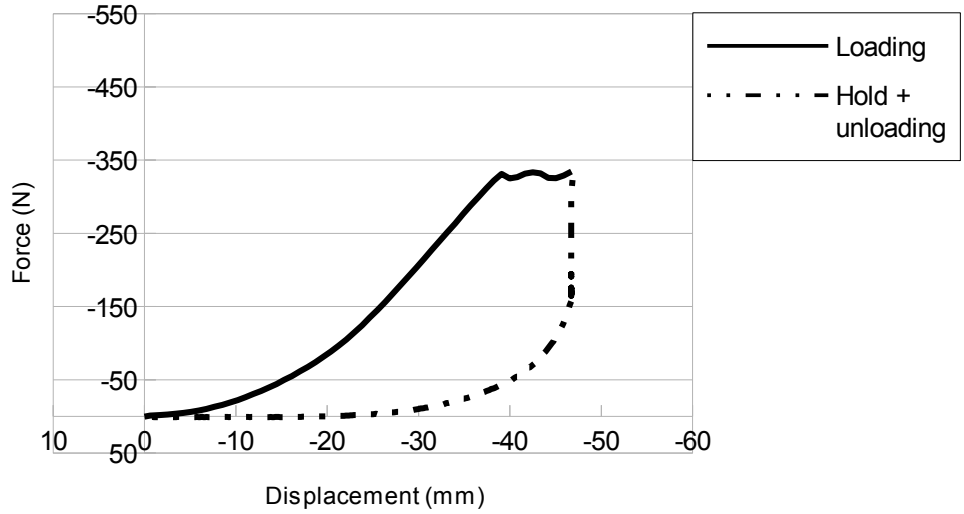

Figure 43: Load against displacement graph for mechanical test on Pig 2

Figure 44 highlights the costochondral joint failure to right rib 5 which remained displaced following mechanical testing.

Figure 44. Photograph of external of Pig 2 thorax following abusive scenario mechanical test: red circle indicating costochondral failure to right rib 5

Pig 3

The force-displacement profile for the abusive scenario carried out on pig 3 is presented in Figure 45. The loading curve initially rises in a non-linear to linear fashion until reaching a maximum reaction force of 497.94 N at 44.20 mm, before then falling progressively by 129.84 N until the target displacement of 56.50 mm was reached. The sternum was then held at this displacement for a duration of 5 minutes. At the start of the holding phase the reaction force was 368.1 N, falling to 113.73 N at the end of the hold, giving a resultant drop off of 254.37 N (368.1 - 113.73).

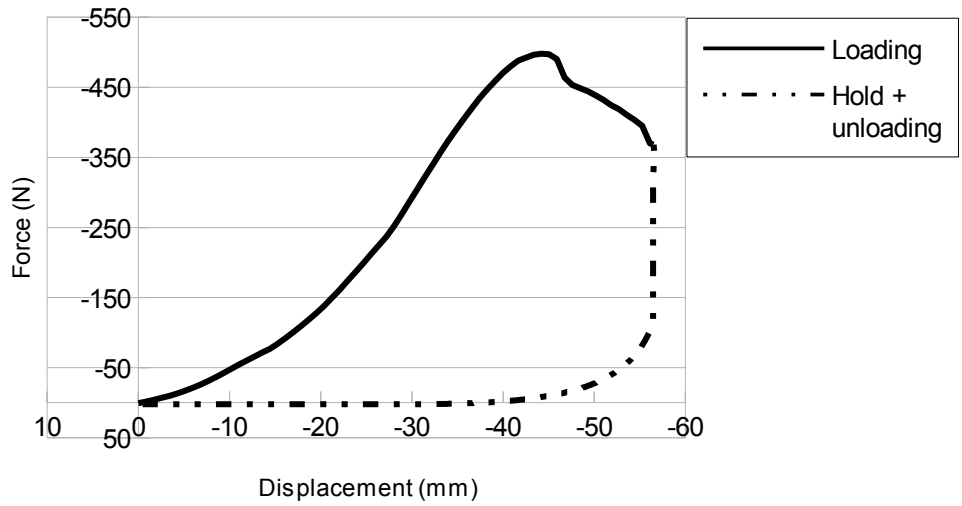

Figure 45: Load against displacement graph for mechanical test on Pig 3

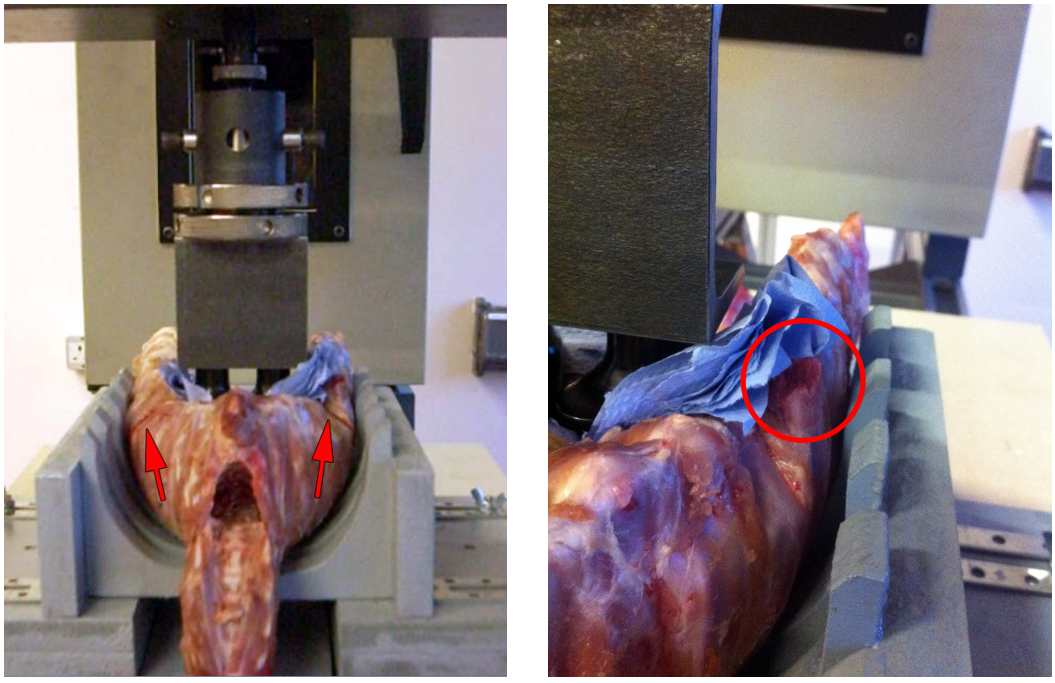

(a) (b)

Figure 46. Photographs of Pig 3 thorax during abusive scenario mechanical test (a) external view with spine inferior to sternum: red arrows indicating bleeds from anterior rib fractures (b) external view: red circle highlighting complete rib fracture to right rib 6

The red arrows in Figure 46a indicate bleeding that emanated from the anterior of both left and right rib 5 signifying trauma in the costochondral regions of these ribs. The circle in Figure 46b contains the displaced compound fracture to right rib 6, occurring just posterior to sternal end of the rib.

Pig 7

The loading curve for pig 7 (Figure 47) rises non-linearly with an increasing gradient before beginning to level off just prior to reaching the maximum displacement. The peak load measured at 1/3 anterior-posterior displacement of the thorax was 314.33 N.

The thorax was held compressed at 2/3 its original anterior-posterior diameter for a duration of 5 minutes, throughout which the force dropped by 212.78 N (314.33 – 101.55). Upon unloading, the reaction force fell non-linearly reaching zero at a displacement of approximately 40 mm.

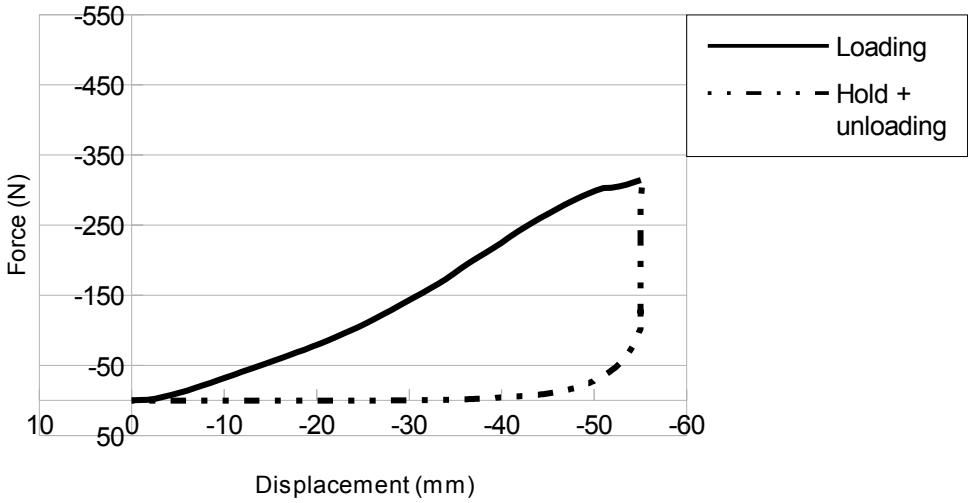

Figure 47: Load against displacement graph for mechanical test on Pig 7

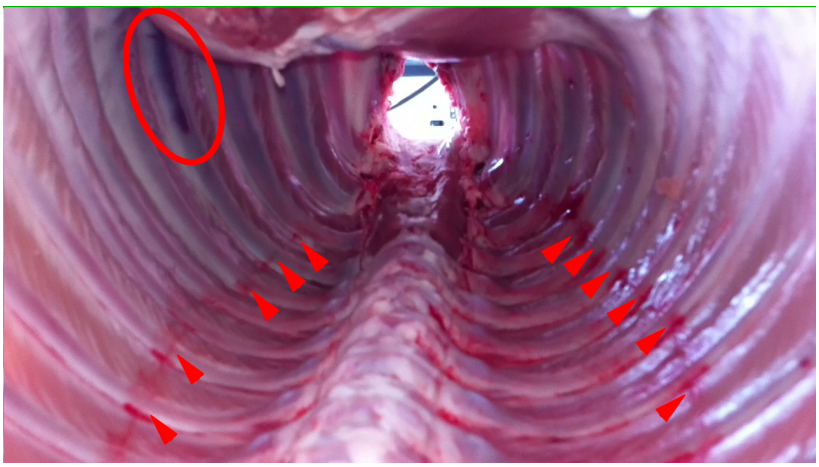

Figure 48. Photograph of internal of Pig 7 thorax during abusive scenario mechanical test (red arrowheads indicate bleeds from posterior rib fractures, red oval highlighting damage to right rib 5)

The arrowheads in Figure 48 indicate apparent posterior/lateral fractures below the periosteum on multiple ribs. The red circle highlights a region spanning from the anterior of right rib 5 towards its lateral body in which it is heavily discoloured underneath the periosteum, indicating damage or a bleed of some kind.

Pig 8

The force-displacement profile resultant from imparting the abusive scenario on pig 8 is presented in Figure 49. Initially the loading curve exhibits a non-linear rise in force against displacement, followed by a small linear rising portion, it then continues to rise non-linearly with an increasingly shallower gradient. At a displacement of 46 mm the gradient then increases again, but immediately begins to level out again, at which point the maximum displacement of 53.04 mm is reached, corresponding to the peak load of 358.13 N.

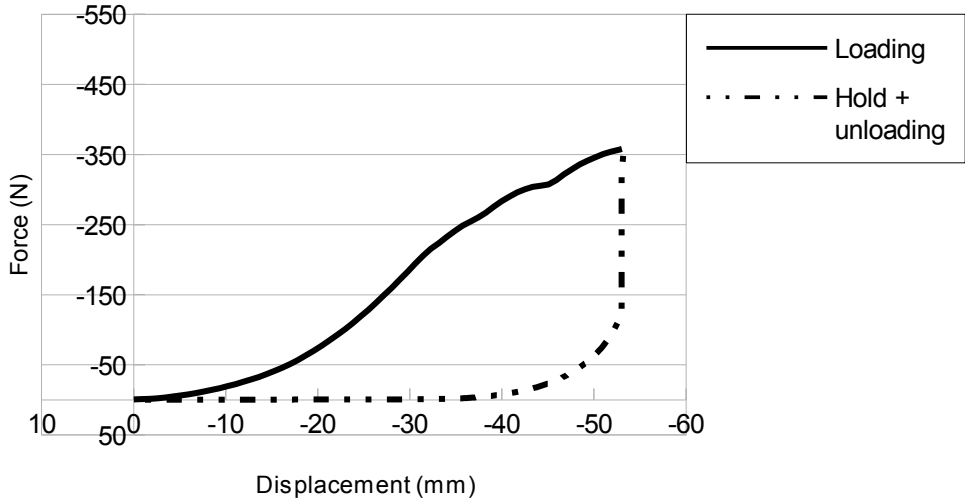

Figure 49: Load against displacement graph for mechanical test on Pig 8

The drop off in load over the duration of the 5 minute hold was 235.3 N (358.13 – 122.83). The curve for unloading decreases non-linearly, reaching zero force at approximately 35 mm displacement, this being the point at which the thumbs no longer engaged with the thorax.

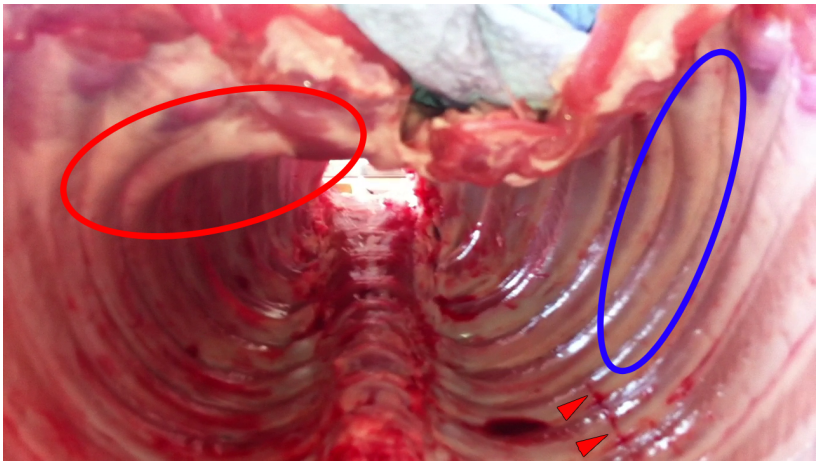

Figure 50. Photograph of internal of Pig 8 thorax during abusive scenario mechanical test (red arrowheads indicating apparent fractures to posterior of left ribs 7 and 8, red oval highlighting heavily distorted right rib 5, and blue oval indicating left rib 6)

During the mechanical test the the fifth right rib (red oval) became heavily distorted, whilst its left counterpart and adjacent sixth left rib (blue oval) did not appear to (see Figure 50). The two red arrowheads indicate bleeding from apparent transverse fractures to the posterior of ribs seven and eight.

Pig 9

Figure 51 shows the loading curve for pig 9 rising in a non-linear fashion before beginning to level off. At the point at which the thorax had been compressed to 2/3 its original size the peak load of 341.09 N for the entire scenario was measured.

At the end of the 5 minute holding period the reaction force was measured at 94.24 N, giving a total drop off in load of 246.85 N (341.09 - 94.24). The unloading curve reaches zero in the region of 35 mm displacement after following a non-linear path.

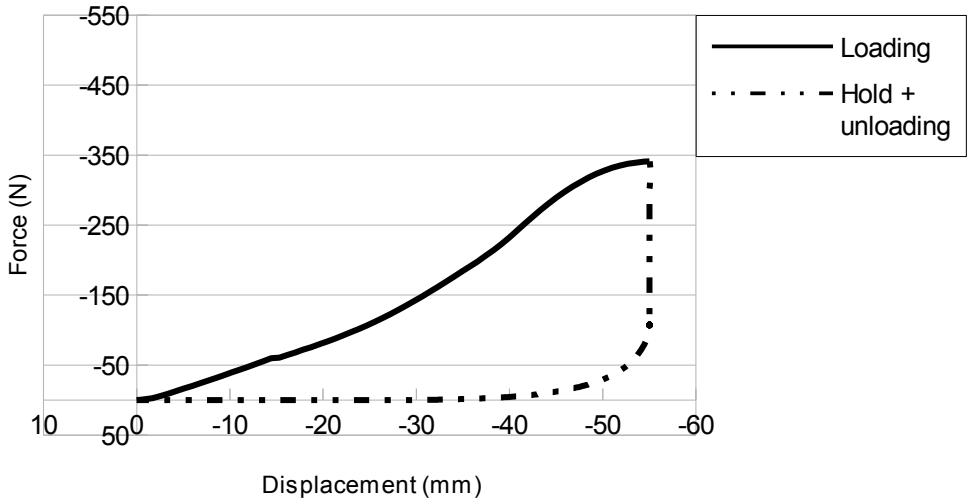

Figure 51: Load against displacement graph for mechanical test on Pig 9

The red arrowheads in Figure 52 indicate transverse fractures to anterior areas of the third and fourth right ribs, as well as the fourth and fifth left ribs. These anterior fractures did not penetrate the periosteum of the respective ribs, appearing to be the result of crushing to areas just posterior of the sternal rib ends. The thorax of pig 9 had an absence of posterior fractures visible by eye.

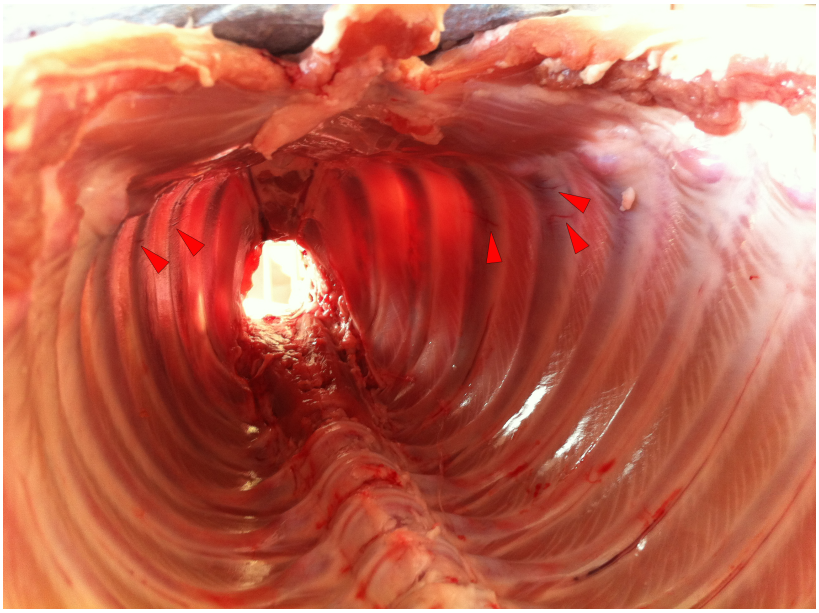

Figure 52. Photograph of internal of Pig 9 during abusive scenario mechanical test (red arrows indicate bleeds from anterior rib fractures)

4.1.4 Summary of Abusive Mechanical Tests on Piglets

Load-displacement curves for pigs 2, 7, 8, and 9 had a similar profile whereby the reaction force measured by the load cell increased non-linearly in relation to the applied

displacement until the holding period. The reaction force exerted on the load cell decreased markedly during the period the thorax was held depressed at 1/3 total AP diameter:

During the mechanical tests simulating abusive squeezing all the samples except for the third piglet recorded the peak force when the maximum displacement (i.e. 1/3 anterior-posterior depth) was reached. The average peak force was 369.20N, and 337.02N with sample 3 included and excluded respectively. The peak forces, forces at hold, and respective decreases in force over the duration of the hold are summarised in Table 5. Whilst the sterna of the rib cages were held depressed by 1/3 anterior-posterior chest depth, the reaction force measured by the load cell decreased by an average of 225.38N.

Pig	***Peak force (N)***	***Displacement at peak force (mm)***	***Force at hold (F_0) (N)***	***Displacement at F_0 (mm)***	***Force at end of hold (F_1) (N)***	***Displacement at F_1 (mm)***	***F_0-F_1 (N)***
1	Sample voided						
2	334.52	46.75	334.52	46.75	156.92	46.70	177.6
3	497.94	44.20	368.1	56.50	113.73	56.46	254.37
7	314.33	55.05	314.33	55.05	101.55	55.00	212.78
8	358.13	53.04	358.13	53.04	122.83	53.00	235.3
9	341.09	55.02	341.09	55.02	94.24	55.00	246.85

Table 5. Summary of abusive scenario mechanical tests

4.2 Classification of Fractures Using X-ray Radiography and Tomography

Radiographs and CT scans of each pigs thoracic cage were taken prior to and following the mechanical tests in order to identify and catalogue the damage specifically caused during compression of their thorax. This section presents the findings.

4.2.1 Summary of CPR Related Fractures Identified with Radiography

The table below details locations of fractures identified with radiography before and after CPR simulation.

Rib Cage	Rib	Before or after test	Anterior	Lateral	Posterior
4	Left 5	Before	N	N	N
		After	N	N	N
	Right 5	Before	N	N	N
		After	N	N	N
	Left 6	Before	N	N	N
		After	N	N	N
	Right 6	Before	N	N	N
		After	Y	N	N
5	Left 5	Before	N	N	N
		After	P	N	N
	Right 5	Before	N	N	N
		After	N	N	N
	Left 6	Before	N	N	N
		After	N	N	N
	Right 6	Before	N	N	N
		After	N	N	N
6	Left 5	Before	N	N	N
		After	Y	N	N
	Right 5	Before	N	N	N
		After	Y	N	N
	Left 6	Before	N	N	N
		After	N	N	N
	Right 6	Before	N	N	N
		After	N	N	N

Table 6. Summary of CPR Fractures (N= no fracture; Y=fracture; P= possible fracture

4.2.2 CT Scan Assessment Following CPR Scenario Pig 4

Figure 53a shows a CT-slice through the transverse plane of pig 4 taken at the level of the sternal ends of rib pair 6. The red arrowhead indicates a fracture to the sternal end of right rib 6, whilst the red circle highlights possible damage to the sternal end of left rib 6.

Figure 53b is CT slice along the coronal plane of pig 4, the white box encloses the sternal end of right rib 6 and the red arrowhead marks a fracture.

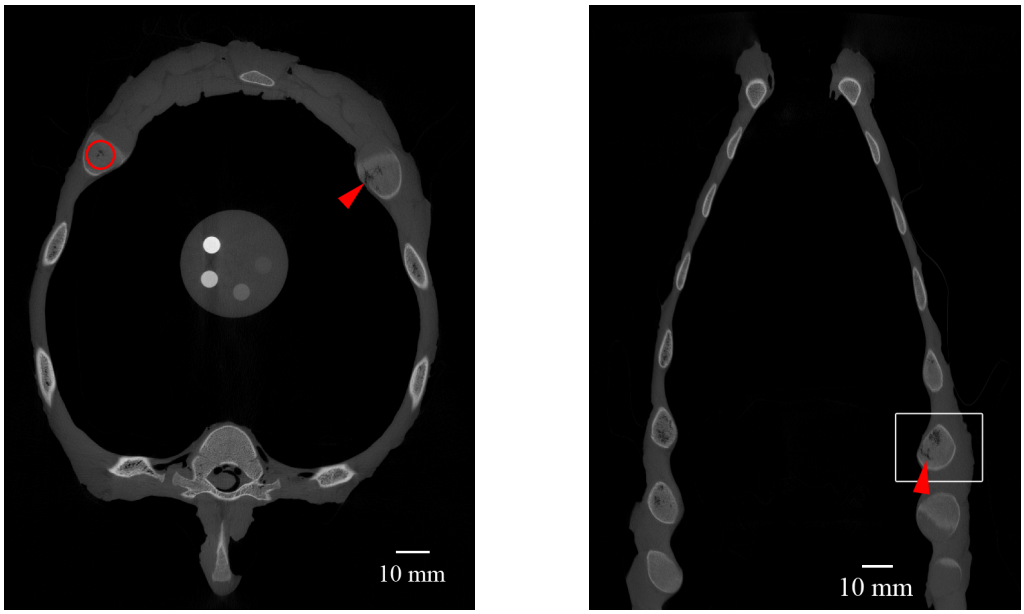

(a) (b)

Figure 53. CT slices through transverse and coronal planes of Pig 4 following CPR scenario mechanical test. See text for annotation detail.

Figure 54 highlights what appear to be fractures within the posteriors of the 6th ribs, with the blue and red arrowheads denoting possible posterior fracture to left rib 6 and right rib 6 respectively.

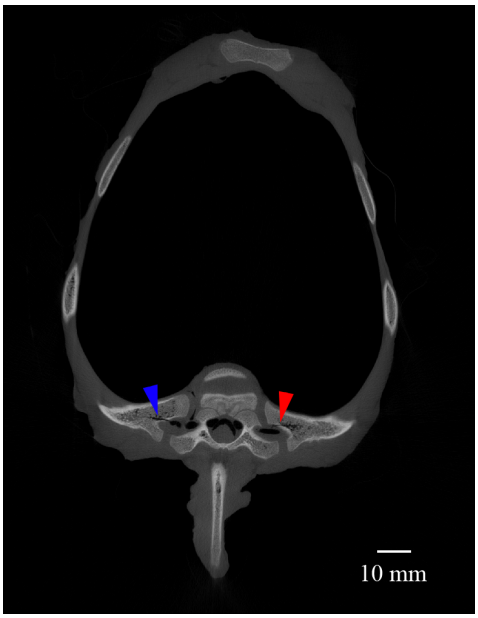

Figure 54. CT slice through transverse plane of Pig 4 at level of the posterior of the 6th ribs following CPR scenario mechanical test. Annotation detail within accompanying text

Pig 5

Figure 55a shows a fracture to the sternal end of right rib 5 in pig 5 (red arrowhead). Also evident is a fracture and disruption to the sternal end of left rib 5 highlighted by the red circle.

Figure 55b highlight fractures to the sternal ends of left rib 5 (blue arrowhead) and left rib 6 (red arrowhead) of pig 5.

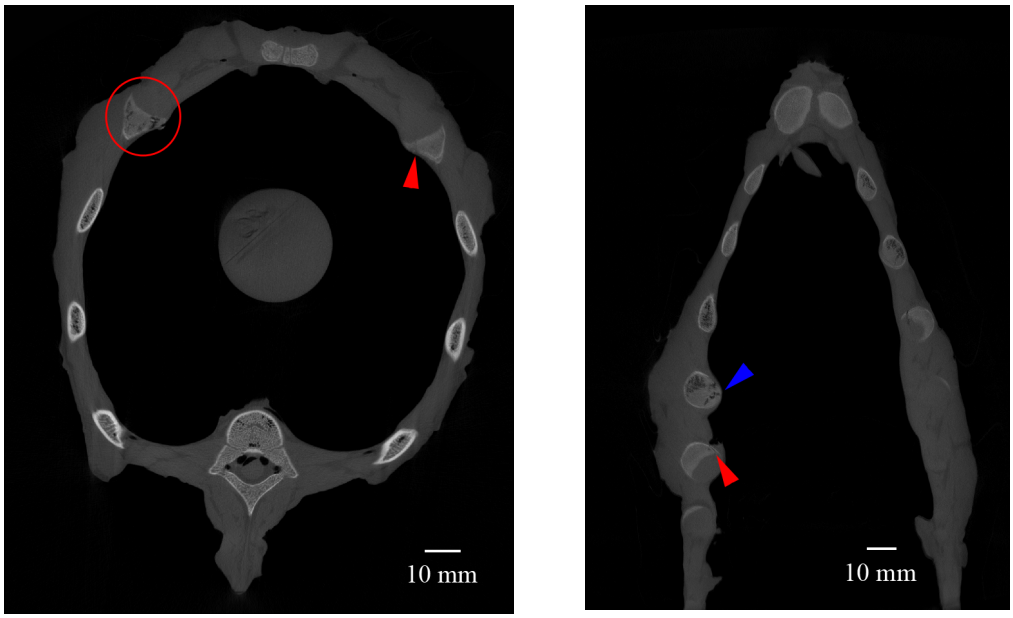

(a) (b)

Figure 55. CT slices of Pig 5 following CPR scenario mechanical test (a) transverse plane (b) coronal plane. Explanation of annotations within text.

The red and blue arrowheads within Figure 56 highlight possible posterior fractures to the right and left fifth ribs of pig 5 respectively. These were seen after simulated CPR.

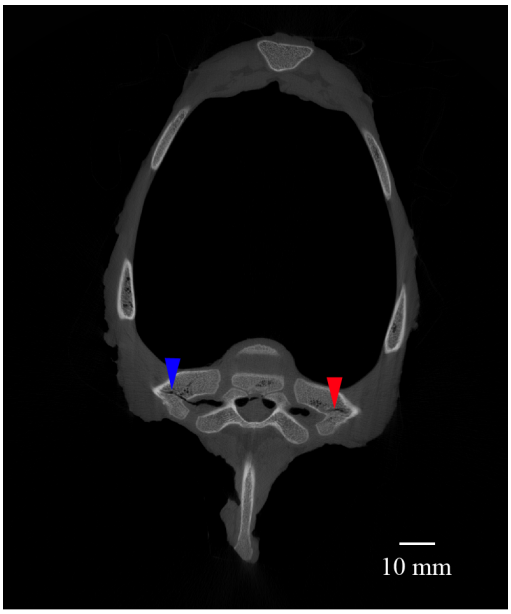

Figure 56. CT slice through transverse plane of Pig 5 at the posterior level of the 5th rib pair following CPR scenario mechanical test. Annotation detail within text.

Pig 6

The blue arrowhead shown in Figure 57a indicates a fracture to sternal end of left rib 5, whilst within the same figure the red arrowhead denotes a fracture to the sternal end of right rib 5.

Figure 57b is a CT slice taken through the coronal plane of pig 6, level with the sternal ends of the ribs. The red, blue, and green arrowheads indicating fractures to the sternal ends of right rib 5, left rib 5, and left rib 6 respectively.

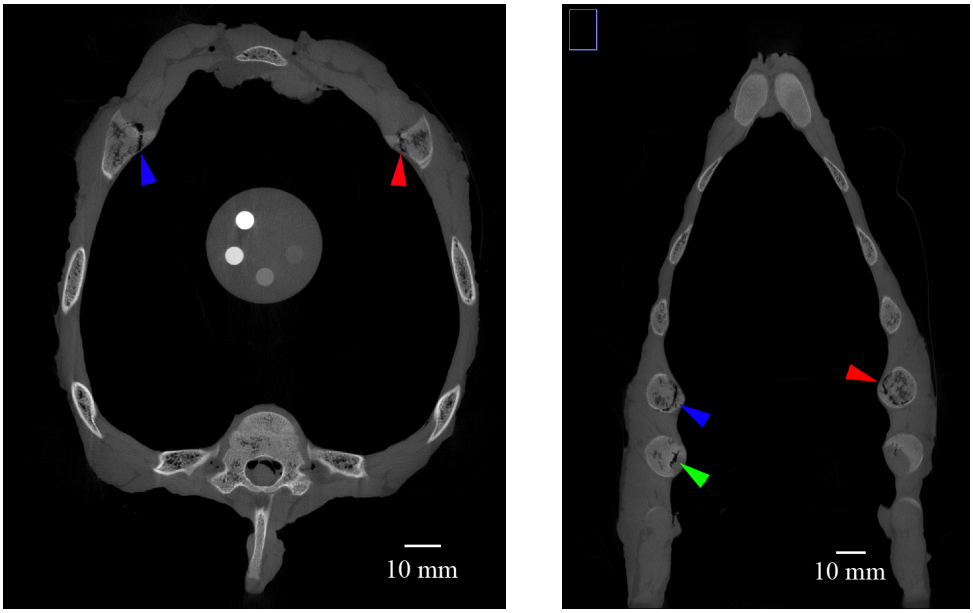

(a) (b)

Figure 57. CT slices of Pig 6 following CPR scenario mechanical test (a) transverse plane (b) coronal plane. See text for annotation details.

4.2.3 Summary of CPR Related Fractures Identified with CT scans

The table below details locations of fractures identified with X-ray CT before and after CPR simulation.

Rib Cage	Rib	Before or after test	Anterior	Lateral	Posterior
4	Left 5	Before	N	N	P
		After	N	N	P
	Right 5	Before	N	N	P
		After	N	N	P
	Left 6	Before	N	N	P
		After	P	N	P
	Right 6	Before	N	N	P
		After	Y	N	P
5	Left 5	Before	P	N	P
		After	Y	N	P
	Right 5	Before	N	N	P
		After	Y	N	P
	Left 6	Before	N	N	P
		After	Y	N	P
	Right 6	Before	N	N	P
		After	Y	N	P
6	Left 5	Before	N	N	P
		After	Y	N	P
	Right 5	Before	N	N	P
		After	Y	N	P
	Left 6	Before	N	N	P
		After	Y	N	P
	Right 6	Before	N	N	P
		After	Y	N	P

Table 7. Summary of CPR Fractures (N= no fracture; Y=fracture; P= possible fracture)

4.2.4 Summary of Abuse Related Fractures Identified with Radiography

The table below details locations of fractures identified with radiography before and after abusive squeezing simulation.

Rib Cage	Rib	Before or after test	Anterior	Lateral	Posterior
2	Left 5	Before	N	N	N
		After	N	N	N
	Right 5	Before	N	N	N
		After	Y	N	N
	Left 6	Before	N	N	N
		After	P	N	N
	Right 6	Before	N	N	N
		After	P	N	N
3	Left 5	Before	N	N	N
		After	N	P	N
	Right 5	Before	N	N	N
		After	Y	Y	N
	Left 6	Before	N	N	N
		After	P	Y	N
	Right 6	Before	N	N	N
		After	Y	N	N
7	Left 5	Before	N	N	N
		After	N	N	N
	Right 5	Before	N	N	N
		After	N	N	N
	Left 6	Before	N	N	N
		After	N	N	N
	Right 6	Before	N	N	N
		After	N	N	N
8	Left 5	Before	N	N	N
		After	N	N	N
	Right 5	Before	N	N	N
		After	N	N	N
	Left 6	Before	N	N	N
		After	N	N	N
	Right 6	Before	N	N	N
		After	N	N	N
9	Left 5	Before	N	N	N
		After	N	N	N
	Right 5	Before	N	N	N
		After	N	N	N
	Left 6	Before	N	N	N
		After	N	N	N
	Right 6	Before	N	N	N
		After	N	N	N

Table 8. Summary of abusive fractures identified using radiography (N= no fracture; Y=fracture; P= possible fracture)

4.2.5 CT Scan Assessment Following Abusive Scenario Pig 2

The red arrowhead within Figure 58a indicates a fracture to the medial sternal end of the fifth right rib within pig 2 following simulated abusive squeezing. The fracture extends through the bone and apparently run along the costochondral junction leaving the rib displaced.

Figure 58b shows fractures to the sternal ends of right rib 5, right rib 6, and left rib 6, respectively denoted by red, blue, and green arrowheads.

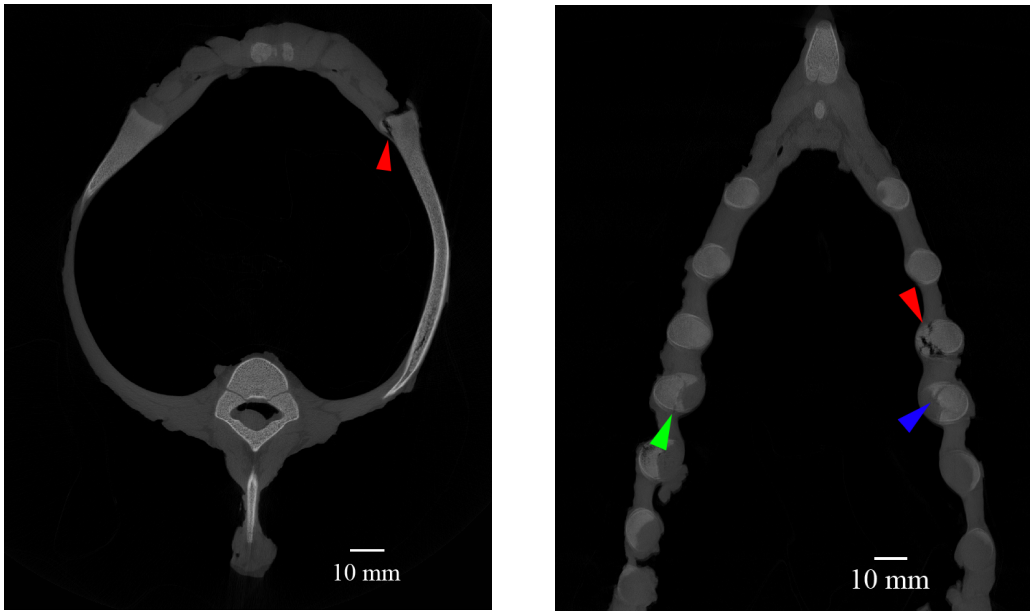

(a) (b)

Figure 58. CT slices of Pig 2 following abusive scenario mechanical test (a) transverse plane (b) coronal plane. Annotation detail within text.

Within Figure 59 the red and blue arrowheads indicate possible fractures to the posterior of left rib 6, whilst the green arrowhead points to a likely fracture of posterior right rib 5.

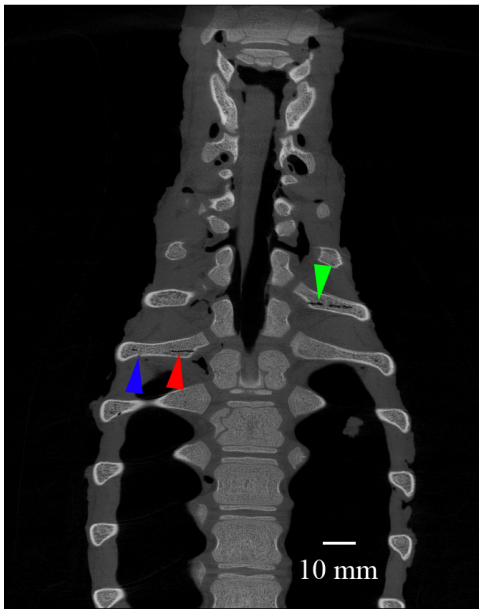

Figure 59. Coronal plane CT slice of Pig 2 taken through posterior of ribs subsequent to abusive scenario mechanical test. See text for annotation detail.

Pig 3

A displaced compound fracture to the anterior of right rib 6 is indicated by the red oval within Figure 60a. Figure 60b provides an alternative view of this fracture, with the red oval indicating the displaced sternal end of right rib 6, the red arrowhead pointing to the remainder of right rib 6, and the blue arrowhead identifying a separate fracture to the sternal end of left rib 6.

(a) (b)

Figure 60. CT slices of Pig 3 following abusive scenario mechanical test (a) transverse plane (b) coronal plane. Annotation detail within text.

Figure 61a highlights lateral fractures located at the medial sides of left rib 5 and right rib 5. The blue arrowhead indicates the fracture to left rib 5, whilst the red arrowhead identifies the fracture to right rib. Figure 61b give an alternative view of the lateral fracture to right rib 5 (blue arrowhead), whilst also highlighting a lateral fracture to left rib 6 (blue arrowhead).

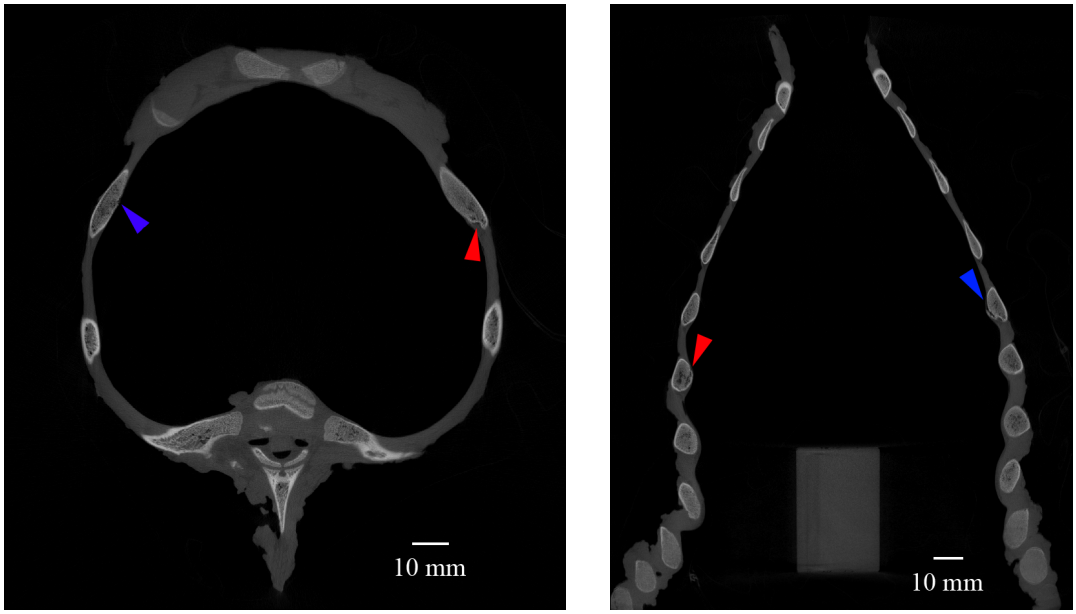

Figure 61. CT slices detailing lateral fractures following abusive scenario mechanical test on Pig 3 (a) transverse plane (b) coronal plane. Annotation detail within main body text.

Pig 7

Figure 62a shows a fracture (red arrowhead) and damage to the costochondral joint of right rib 6 within pig 7. An alternative view of this fracture can be seen in Figure 62b and is highlighted by a red arrowhead.

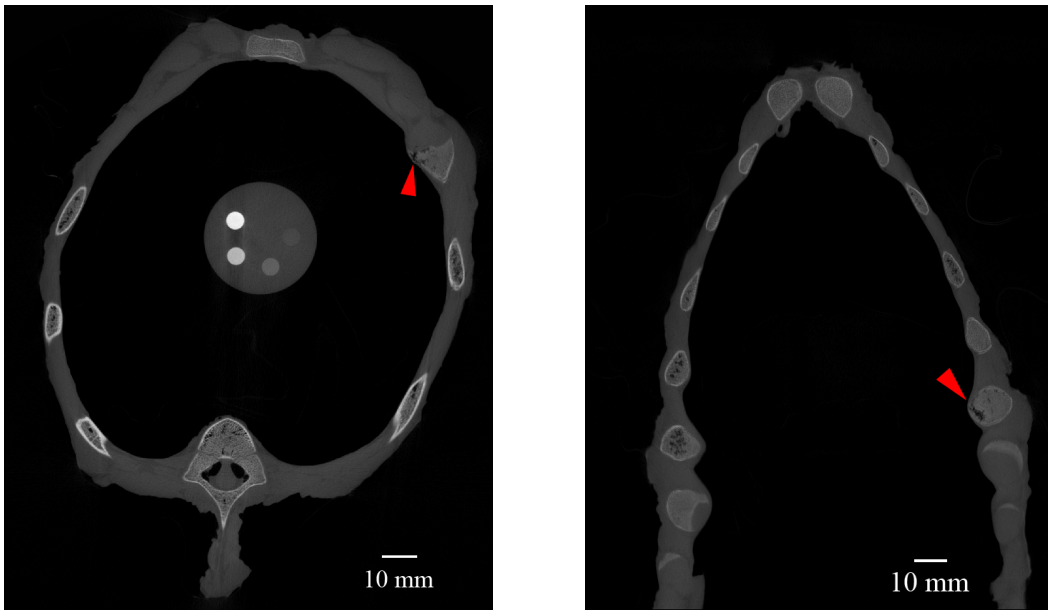

Figure 62. CT slices of Pig 7 following abusive scenario mechanical test (a) transverse plane (b) coronal plane. See text for annotation detail.

The red arrowhead shown within Figure 63a points to a possible fracture within the posterior region of right rib 6. Further possible posterior fractures within pig 7 are indicated in Figure 63b being located in right rib 5 (red arrowhead) and left rib 6 (blue arrowhead).

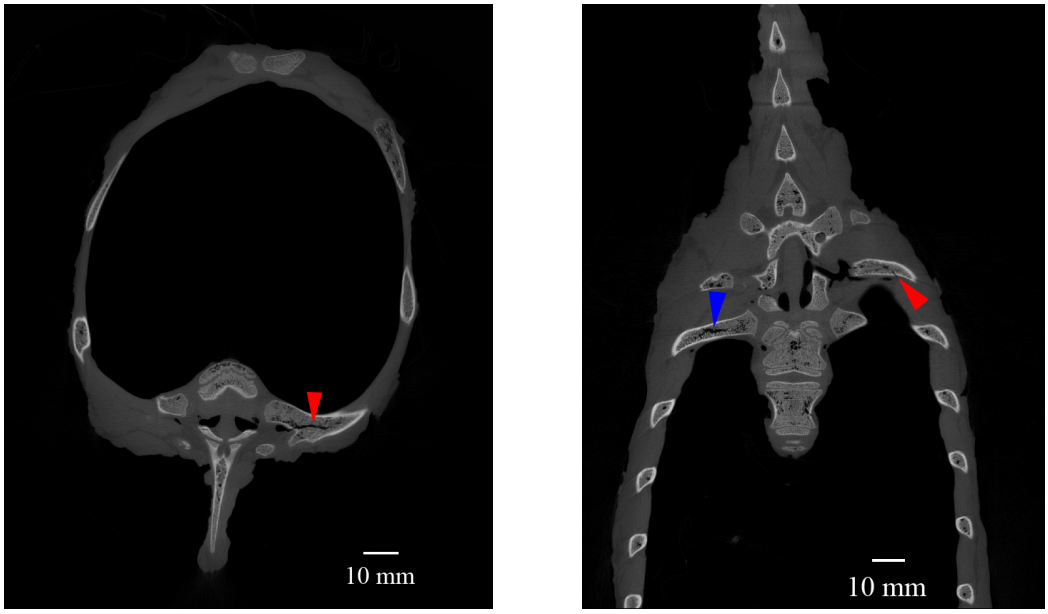

(a) (b)

Figure 63. CT slices of Pig 7 following abusive scenario mechanical test (a) transverse plane (b) coronal plane. Annotation detail within text.

Pig 8

The red arrowhead shown in Figure 64a indicates a fracture to the sternal end of left rib 5, and associated damage to the costochondral junction. Figure 64b highlights a possible fracture or damage to the bone within the sternal end of right rib 6.

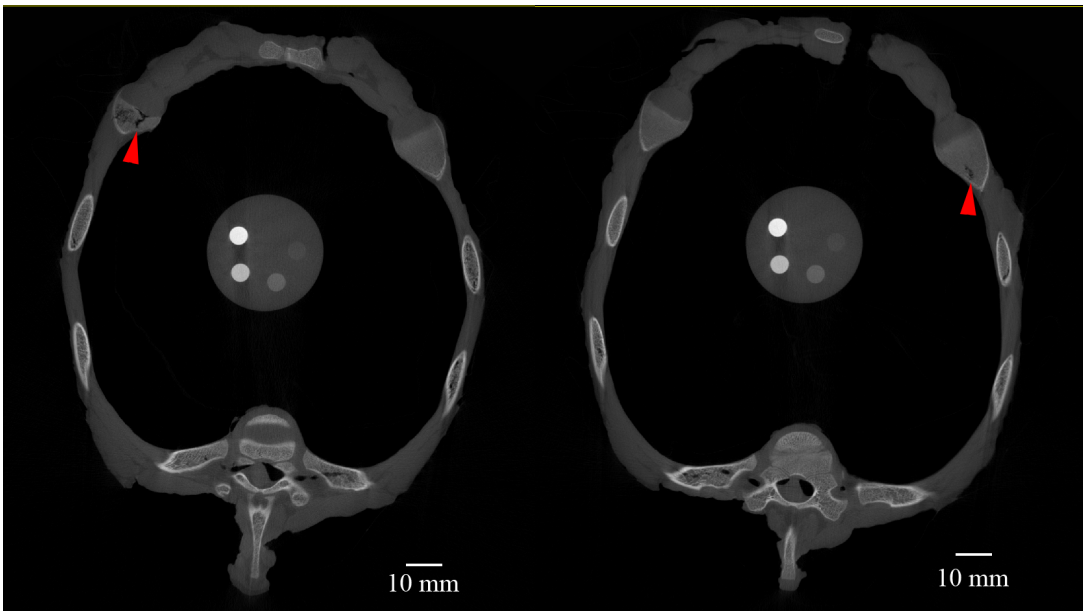

(a) (b)

Figure 64. CT slices through transverse plane of Pig 8 following abusive scenario mechanical test (a) taken level with anterior of 5th rib pair (b) taken level with anterior of 6th rib pair. Annotation details within text.

Pig 9

A fracture to sternal end of right rib 5 is highlighted in Figure 65a and is shown in an alternative plane within Figure 65b.

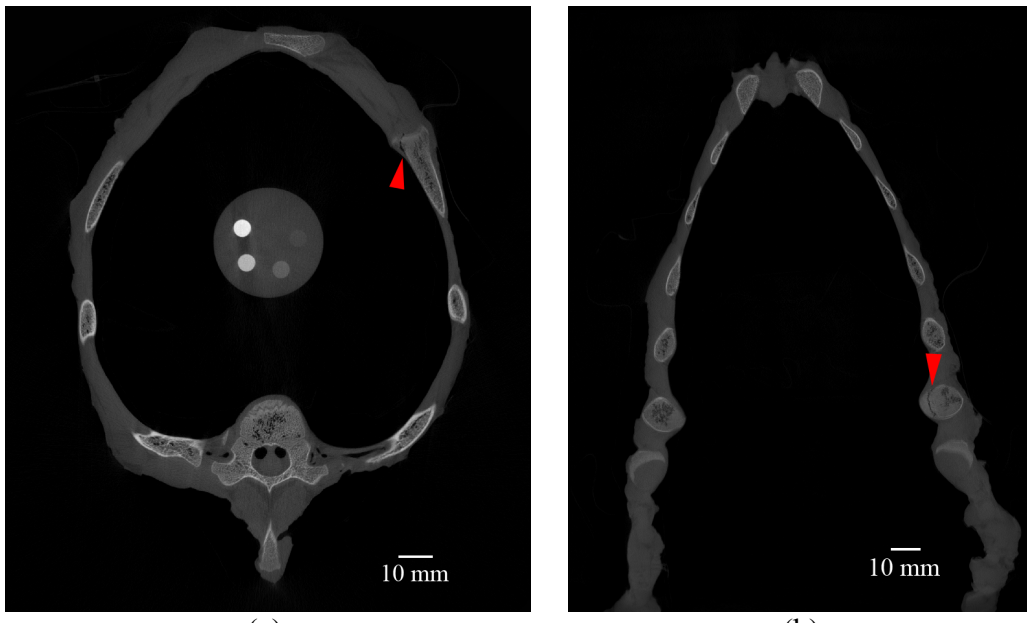

(a) (b)

Figure 65. CT slices of Pig 9 following abusive scenario mechanical test (a) transverse plane (b) coronal plane. See text for annotation details.

The blue arrowhead in Figure 66 points to the beginning of a possible fracture to the posterior region of left rib 6 of pig 9, with the red arrowhead appearing to show where it terminates.

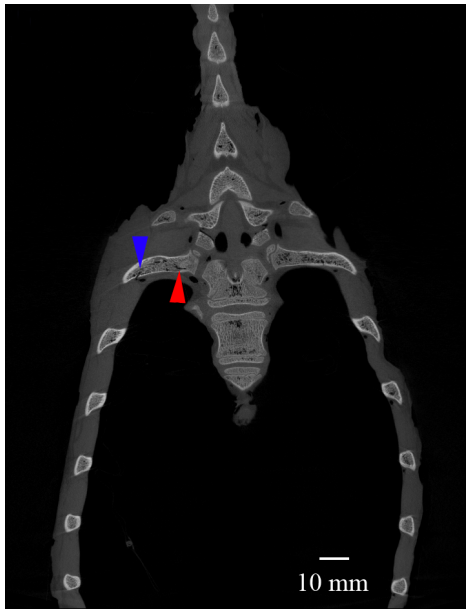

Figure 66. CT slice through coronal plane of Pig 9 following abusive scenario mechanical test. Annotation detail within accompanying text.

4.2.6 Summary of Abuse Related Fractures Identified with CT scans

Fracture locations identified with X-ray CT before and after abusive simulation are detailed in the table below.

Rib Cage	Rib	Before or after test	Anterior	Lateral	Posterior
2	Left 5	Before	N	N	P
		After	N	N	P
	Right 5	Before	N	N	P
		After	Y	N	P
	Left 6	Before	N	N	P
		After	Y	N	P
	Right 6	Before	N	N	P
		After	Y	N	P
3	Left 5	Before	P	N	P
		After	Y	Y	P
	Right 5	Before	P	N	P
		After	Y	Y	P
	Left 6	Before	N	N	P
		After	Y	Y	P
	Right 6	Before	N	N	P
		After	Y	N	P
7	Left 5	Before	N	N	P
		After	P	N	P
	Right 5	Before	N	N	P
		After	Y	N	P
	Left 6	Before	N	N	P
		After	N	N	P
	Right 6	Before	N	N	P
		After	Y	N	P
8	Left 5	Before	Y	N	P
		After	Y	N	P
	Right 5	Before	N	N	P
		After	N	N	P
	Left 6	Before	N	N	P
		After	N	N	P
	Right 6	Before	P	N	P
		After	P	N	P
9	Left 5	Before	N	N	P
		After	P	N	P
	Right 5	Before	N	N	P
		After	Y	N	P
	Left 6	Before	N	N	P
		After	N	N	P
	Right 6	Before	N	N	P
		After	Y	N	P

Table 9. Summary of Abusive Fractures (N= no fracture; Y=fracture; P= possible fracture)

4.2.7 3D Visualisation of Ribs From CT Scan Data

The visualisations presented in Figure 67 show the anterior region of a typical immature pig rib in different orientations prior to any physical testing. Figure 67a indicates an area of the rib that routinely, across all immature samples, has a more disorganised and less mineralised bone tissue structure.

The highlighted region in Figure 67b is a dense bony collar that encapsulates the costochondral junction. This structure is seen across all immature pig ribs imaged.

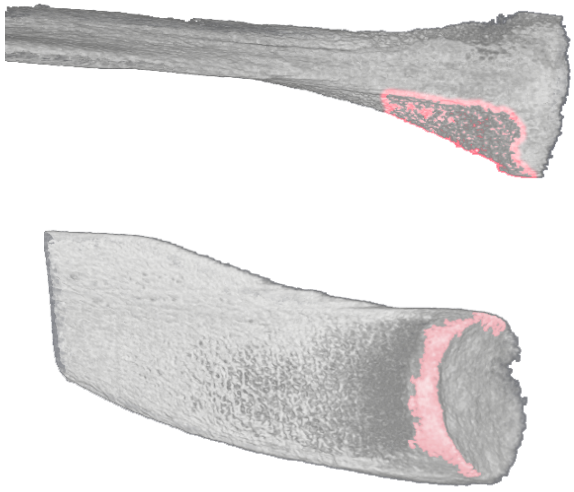

Figure 67. Anterior region of characteristic piglet rib before mechanical testing (a) superior view of sternal end of rib (area of lower density bone highlighted) (b) oblique view of sternal end of rib (pink highlights bone collar)

Figure 68 shows a fracture to the anterior of a rib following testing under the CPR testing regime. The red oval indicates the medial portion of the bony collar that had broken away from the rib. This specimen is characteristic of fractures in the costochondral junction area for both CPR and abusive testing scenarios.

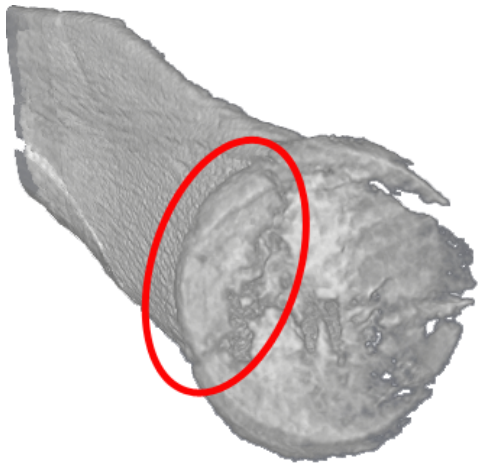

Figure 68. 3D visualisation from CT data of a characteristic costochondral junction fracture (red oval highlights the separated rim of rib bone)

N.B. Costal cartilage not shown

Features that appeared to be posterior rib fractures on X-ray CT slice inspection (e.g. see Figure 54, Figure 56, Figure 59, Figure 63, and Figure 66), can be seen to in actual fact be a foramen in the bone of the rib. Figure 35 shows a 3D visualisation of CT data from a pig rib before testing was performed. This foramen was seen in all ribs, across all piglet specimens.

Figure 69. 3D rendering from CT data of a characteristic rib showing posterior foramen.

N.B. Right rib shown

4.3 Rib Bone Mechanical Behaviour

4.3.1 Mature Pig Ribs

4.3.1.1 Tomography

X-ray tomography produced a 3D dataset of the mature rib section with a voxel size of 0.0248mm^3. Inspection of the scan data (Figure 70) revealed the sample to be free from damage or abnormalities and that it was suitable for mechanical testing. This dataset was suitable for creating an image-based finite element model.

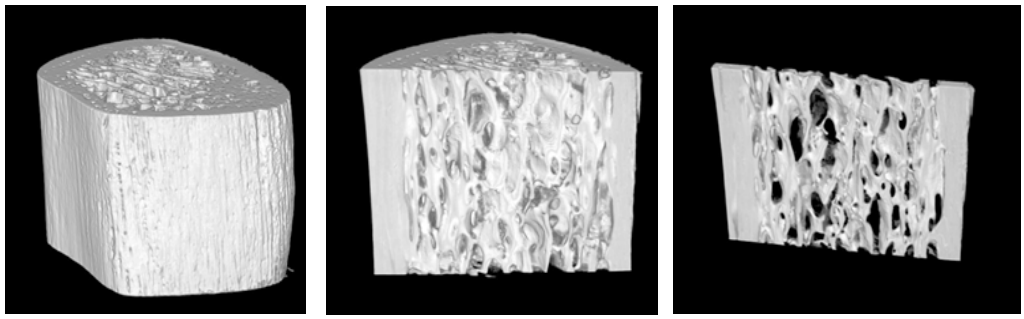

Figure 70. ***3D rendering from X-ray Tomography scan of mature rib rib section taken before mechanical testing.***

4.3.1.2 Mechanical Testing

Due to sample availability and time constraints, only one section of mature rib was subject to mechanical compression. The data for this test represents the failure behaviour of only that particular rib sample, which due to difficulty cutting the sample precisely, in fact measured 6.2mm in height.

The loading test characterised the mechanical behaviour of the sample under compressive conditions. The recorded load-displacement data was corrected to account for the compliance within the testing machine. Figure 71 presents the load-displacement data before (pink) and after (blue) compliance correction.

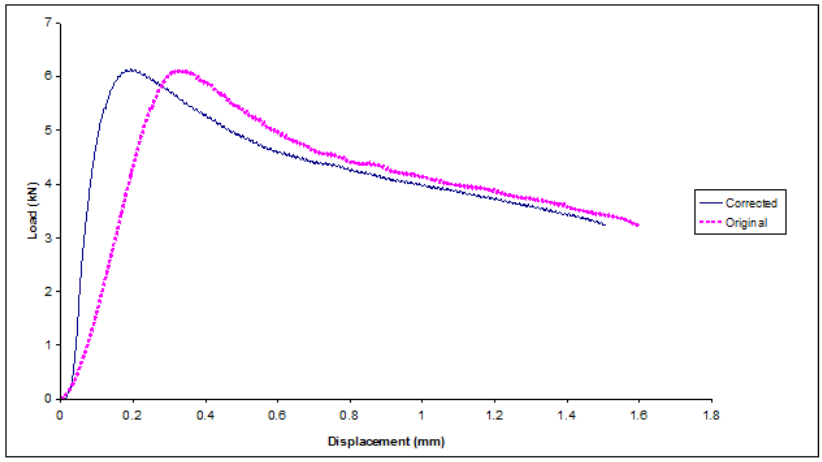

Figure 71. Load-displacement curve for 6.2 mm section of mature rib under compression.

During the experiment the specimen yielded at approximately 6kN, after which it began to spread out laterally as it was crushed/plastically deformed for the remainder of the test (see Figure 72). Selected load-displacement values from the initial slope, i.e. plastic region, are presented in Table 7, along with their corresponding stain percentages.

Figure 72. Mature rib section under compression

Load (kN)	*Displacement (mm)*	*Strain (%)*
0.00	0.00	0.0
0.37	0.03	0.5
2.84	0.06	1.0
5.41	0.12	2.0

Table 10. Force measured from experimental work within the elastic region

4.3.1.3 Nanoindentation

The load-displacement curve shown in Figure 73 is representative of those acquired by nanoindentation for mature rib samples. The average elastic modulus and hardness values were taken from the unloading curve and were found to be 11.64GPa and 0.3 respectively. Average values for elastic modulus (E) and hardness of mature pig rib are summarised in Table 8. It is once again noted that these tests were performed on dry bone samples, and the implications of this will covered in the discussion section of this document.

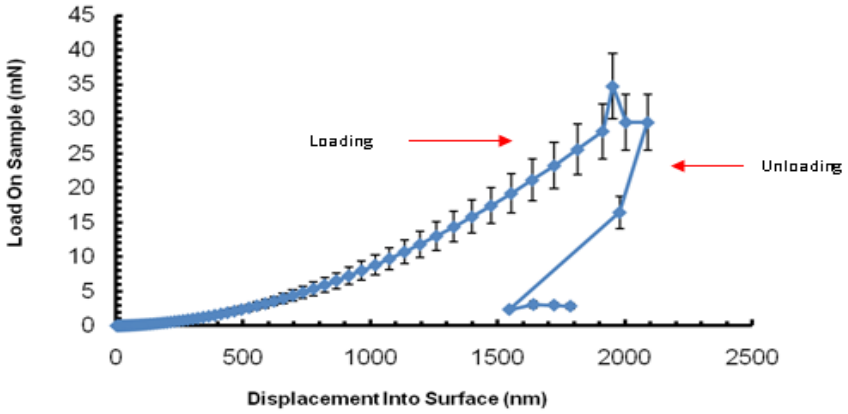

Figure 73. Load-displacement curve for a nanoindentation test on mature porcine rib

	E average over defined range (GPa)	*Hardness average over defined range*	*E from unload (GPa)*	*Hardness from unload*
Mean	12.63	0.37	11.64	0.30
Std. Dev.	1.75	0.07	1.42	0.02
% COV	13.87	18.22	12.17	14.90

Table 11. Young's modulus and hardness obtained from nanoindentation tests on mature porcine rib

4.3.2 Immature Piglet Ribs

4.3.2.1 Tomography

5 mm sections and full intact ribs from immature ribs were CT scanned before mechanical testing. The scans were then inspected for signs of damage Figure 74, with the specimens deemed suitable for mechanical testing and the 3D datasets suitable for FE modelling.

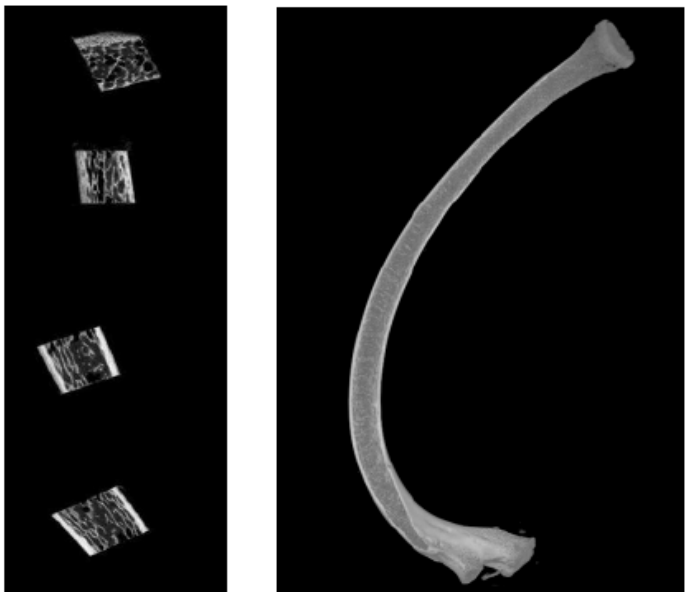

(a) (b)

Figure 74. Microtomography reconstructions of immature bone mechanical assessment samples; (a) 5mm sections, (b) entire rib

4.3.2.2 Mechanical Testing

5mm sections

Compression tests were performed on a series of immature bone sections ~5mm in height. These sections were kept hydrated, Figure 75 shows plots of force-deformation curves for these samples.

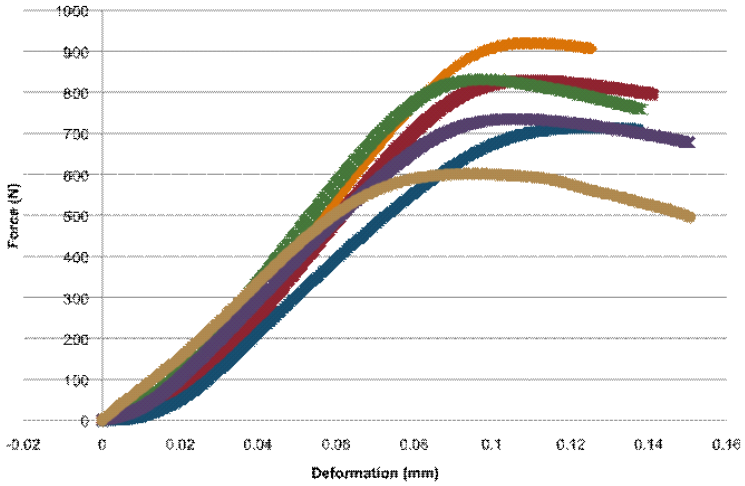

Figure 75. Force-displacement curves for immature rib sections

Individual ribs

The application of load in a manner representative of anteroposterior compression caused the ribs to generally fail by buckling just below the sternal end of the rib (Figure 69), and the average load to failure of whole ribs was 29.9 N.

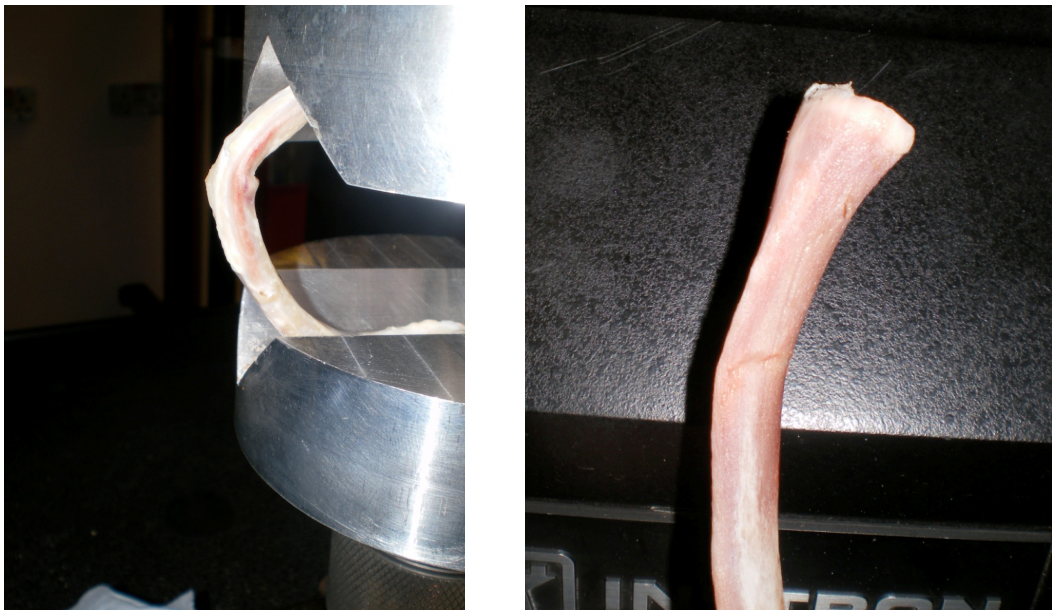

(a) (b)

Figure 76. (a) Immature rib whilst in test rig, just after buckling (b) permanent deformation of rib after compression test

4.3.2.3 Nanoindentation

Nanoindentation of immature ribs produced an overall value of 13.8 GPa from 136 indents for the modulus of elasticity. There was no significant difference between trabecular or cortical bone, or the orientation of the indent with respect to the longitudinal axis of the bone.

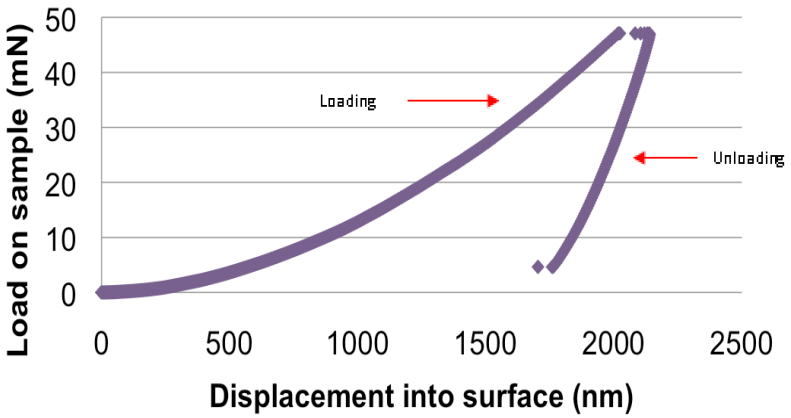

Figure 77. Typical load-displacement curve from nanoindentation of immature porcine rib

Figure 77 shows the typical loading and unloading curves for nanoindentation of an immature porcine rib sample. Depth of indent is on the x-axis (mm) and the load on the sample on the y-axis (mN). The area enclosed by the two curves is equivalent to the energy dissipated during the test.

4.3.2.4 Radiography Following Mechanical Testing

For those full ribs that failed due to buckling, radiography following mechanical testing showed gross deformation (Figure 78a), but no obvious fractures were visible (Figure 78b).

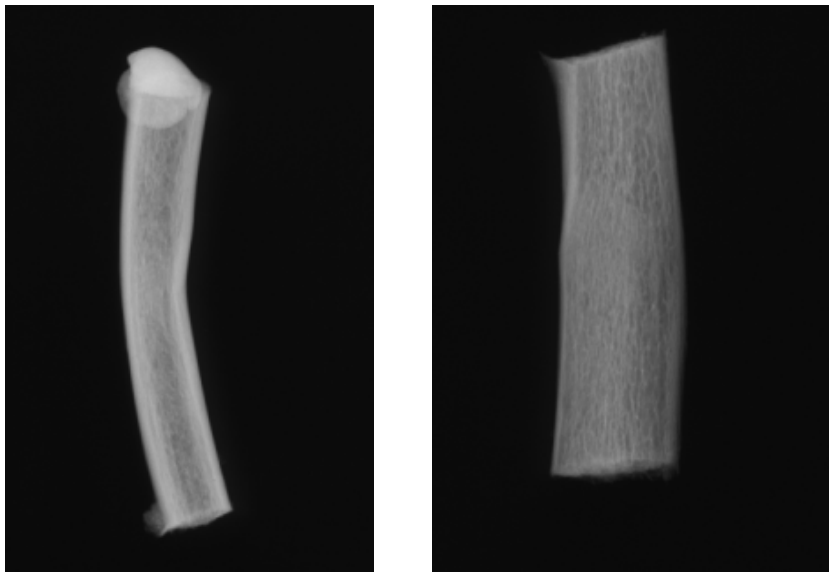

(a) (b)

Figure 78. Radiographs of immature full rib bones following mechanical testing (a) cropped region at sight of buckling, posterior to sternal end of rib (b) same region viewed at 90 degrees to first radiograph

4.4 FE Modelling

4.4.1 Mature Pig Ribs

4.4.1.1 Finite Element mesh for mature bone section

The resultant geometry of the rib section constructed from high resolution CT scanning had a voxel size of 0.0248 mm^3. Use of automated tetrahedral meshing allowed the mesh to represent the trabecular and cortical morphology of entire bone section (Figure 79).

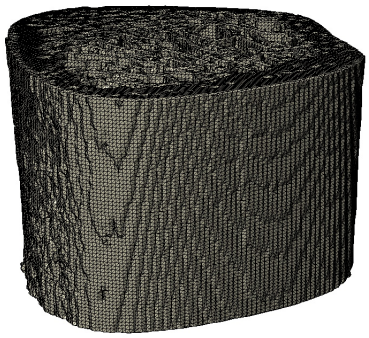

Figure 79. 25% resolution mesh of mature rib section

4.4.1.2 Finite Element simulations for mature bone section

FE simulations of the mature rib section were first run using Young's modulus values obtained from nanoindentation (12GPa), and a Poisson's ratio of 0.3 was assumed. Results from these simulations gave forces double those observed experimentally at given displacements.

Load (kN)	*Displacement (mm)*	*Strain (%)*
0.00	0	0.0
3.41	0.031	0.5
6.80	0.062	1.0
15.6	0.124	2.0

Table 12. Loads calculated from finite element with Young's modulus of 12 GPa

The simulation was rerun with a Young's modulus of 5.3 GPa and Poisson's ratio of 0.3.

Load (kN)	*Displacement (mm)*	*Strain (%)*
0.00	0.0000	0.0
1.54	0.0310	0.5
2.31	0.0465	0.75
3.05	0.0620	1.0
4.59	0.0930	1.5
6.1	0.1240	2.0

Table 13. Loads calculated from finite element with Young's modulus of 5.3 GPa

Figure 80 shows the load-displacement curves for mechanical experimental data and FE simulation data with Young's modulus of 12 GPa and 5.3 GPa. The finite element model with Young's modulus of 12 GPa has a steeper curve compared to others. However, the reaction force for experimental and finite element simulation with 5.3 GPa have almost the same slope. It can be seen from FE with 12 GPa that at a displacement of 0.124mm, the force obtained is 15.6 kN (Table 9), which is three times bigger than the force obtained from physical experimentation. If we compare forces obtained from experimental with those obtained from FE using a Young's modulus of 5.3GPa, it can be seen that at a displacement of 0.124mm the force is 6.1 kN (Table 10), which is closer to the physical experimental value (Table 7).

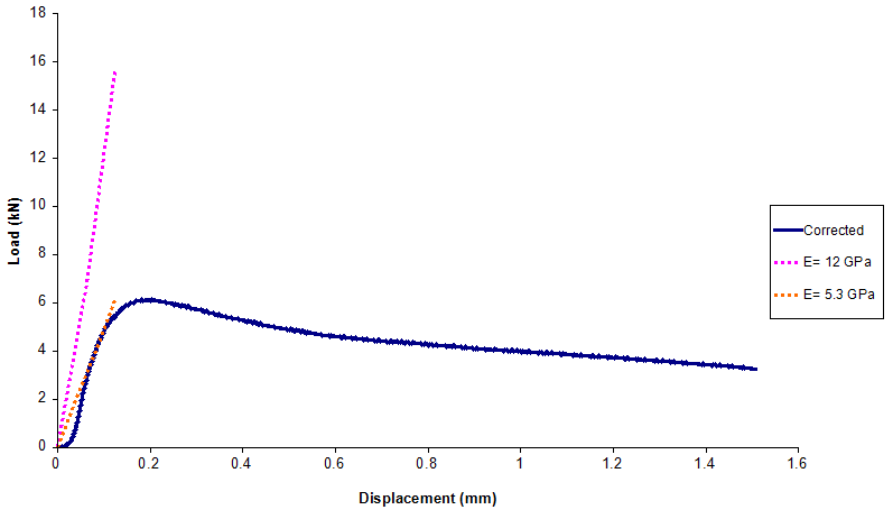

Figure 80. Force displacement curve with mechanical experimental data and FE simulation data for mature rib section

Figure 81 shows a longitudinal cross-section through the mature rib section for the 20% resolution model detailing the predicted stress profile throughout the trabecular and cortical bone.

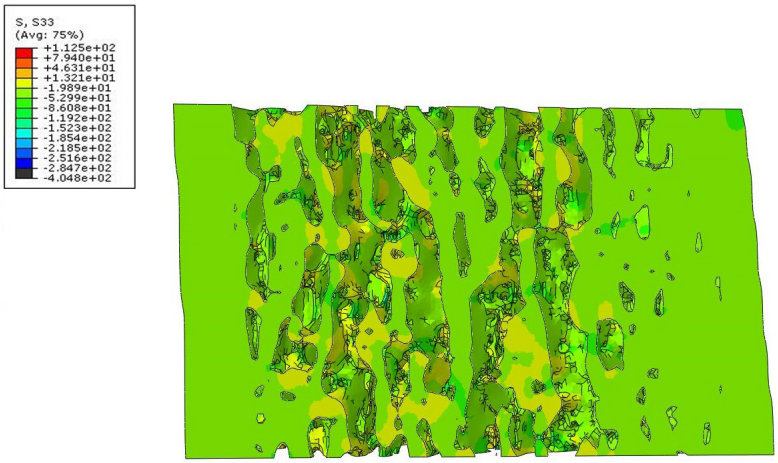

Figure 81. Longitudinal section through simulated stress distribution for mature rib section at 0.75 percent strain with Young's modulus of 5.3 GPa

4.4.2 Meshing Sensitivity Analysis for Mature Bone Section

A series of simulations were run to investigate the effect of model resolution on reaction force and stress measurement. The results presented in Table 11,Table 12,Table 13, and Table 14 are for analyses equivalent to a compressive strain of 1%, i.e. 0.062 mm.

Figure 82 shows the segmentation for a single slice of the 100% resolution CT image data. Threshold values were used that maintained connectivity of trabecular within the cancellous regions of the bone. However, this caused fine porous features within the cortical bone regions to be lost.

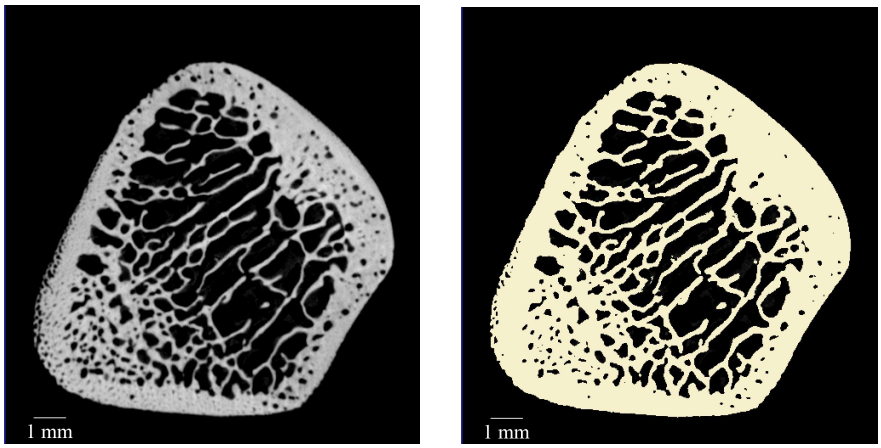

(a) (b)

Figure 82 Transverse cross-section through mature rib section (a) X-ray CT image data (b) applied segmentation of the model mask

All tetrahedra + FE Grid Meshing (1x1x1), E=12GPa

Resolution (%)	*Elements*	*Nodes*	*Reaction Force (kN)*	*Stress (MPa)*
10	184,258	45,890	6.47	101.5
20	1,464,479	331,522	6.82	103
25	2,742,396	599,211	6.24	104
30	4,367,860	961,801	Sim Fail	-
40	9,325,867	2,045,751	Sim Fail	-
50	17,068,869	3,718,996	Sim Fail	-
60	28,133,522	6,084,987	Sim Fail	-
70	43,160,803	9,275,246	Sim Fail	-
80	63,141,674	13,493,509	Sim Fail	-
90	88,235,863	18,761,575	Sim Fail	-
100	Unable to mesh	-	-	-

Table 14 Details of mature bone simulations run with all tetrahedra +FE Grid mesh (1x1x1), and Young's modulus of 12 GPa

All tetrahedra +FE Free (Adaptive Meshing +0cc), E=12GPa

Resolution (%)	*Elements*	*Nodes*	*Reaction Force (kN)*	*Stress (MPa)*
10	261,229	58,349	-	-
15	Unable to mesh	-	-	-
20	2,364,596	451,507	6.48	106.17
25	1,965,058	433,597	6.83	103.86
30	2,711,084	618,453	6.25	100.33
40	5,282,445	1,199,899	5.84	103.35
50	7,683,039	1,816,797	Sim fail	-
60-100	Unable to mesh	-	-	-

Table 15 Details of mature bone simulations run with all tetrahedra adaptive meshing 0cc, and Young's modulus of 12 GPa

All tetrahedra +FE Free (Adaptive Meshing -50cc), E=12GPa

Resolution (%)	*Elements*	*Nodes*	*Reaction Force (kN)*	*Stress (MPa)*
10	Unable to mesh	-	-	-
20	1,209,742	244,721	6.50	106.97
25	1,585,625	317,322	6.87	108.38
30	1,724,845	352,529	6.31	106.97
40	2,389,071	495,959	5.91	104.27
50	3,206,614	671,907	5.69	102.88
60	4,010,517	846,843	5.55	103.18
70	4,866,068	1,033,089	5.45	102.24
75	5,263,591	1,122,308	5.41	103.67
100	7,008,687	1,508,750	5.30	102.16

Table 16 Details of mature bone simulations run with all tetrahedra adaptive meshing -50cc, and Young's modulus of 12 GPa

Figure 83 displays the element count in millions against the resolution of image data used when generating models with Simpleware +FE Free adaptive meshing using a -50 compound coarseness setting. The relationship between element count and model resolution is close to linear.

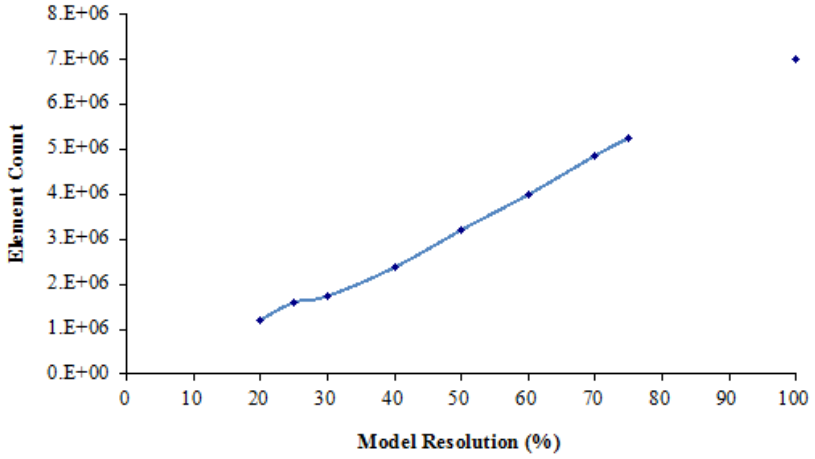

Figure 83. Graph of model element count against model resolution for All tetrahedra Adaptive Meshing -50cc

The graph in Figure 84 shows the reaction force calculations for models with varying resolution generated with Simpleware +FE Free adaptive meshing using a -50 compound coarseness setting. The measured reaction force appears to exponentially decay with increasing model resolution, tending towards an equilibrium value of 5.30 kN.

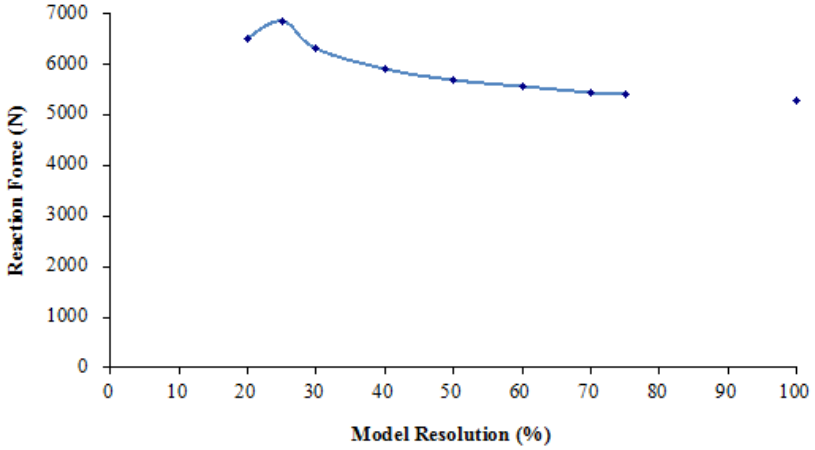

Figure 84. Graph of reaction force against model resolution for simulations using All tetrahedra Adaptive Meshing -50cc, Young's modulus = 12 GPa

All tetrahedra +FE Free (Adaptive Meshing -50cc), E=11GPa

Resolution (%)	*Elements*	*Nodes*	*Reaction Force (kN)*	*Stress (MPa)*
20	1,209,742	244,721	Sim not run	-
100	7,008,687	1,508,750	4.85	93.64

Table 17 Details of mature bone simulations run with all tetrahedra adaptive meshing -50cc, and Young's modulus of 11 GPa

Reducing the input modulus from 12 to 11 GPa gave a 0.45 kN drop for the analysis of 100% resolution data meshed with all tetrahedra, and adaptive meshing at -50cc.

4.4.3 Immature Piglet Ribs

Finite Element simulations for immature bone section and whole rib

FE simulations on an all tetrahedra 10% resolution model of an immature rib sections have yielded reaction force results for a given displacement that are a factor of 10 higher compared with those observed in mechanical testing. Figure 85a presents the predicted stress distribution at a longitudinal section midway through the 5 mm sample.

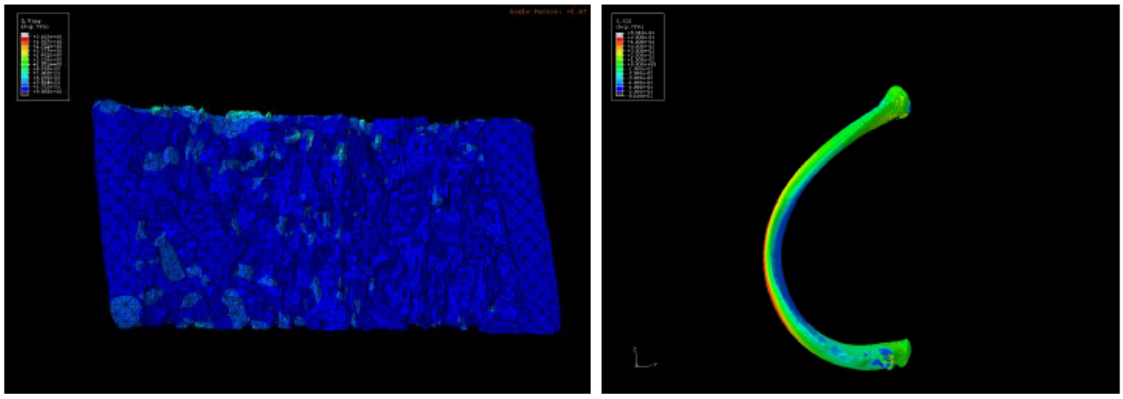

(a) (b)

Figure 85. FE simulations of mechanical assessment tests for immature ribs (a) 5mm section (b) entire rib

Proof of concept for loading individual ribs anterior-posteriorly with suitable boundary conditions was achieved (Figure 85b). However, this was done on a heavily downsampled mesh in order to speed up computational time, and as such this model requires further development.

CHAPTER FIVE

5 Discussion

A discussion of the results of experimental programme and their implications for human infant rib biomechanics is the subject of this chapter.

This thesis covers topics pertinent towards ultimately validating a human infant thorax model to investigate the effect on the ribs due to different loading conditions. To do this it was necessary to establish the mechanical behaviour of immature ribs when within the thorax. Of specific interest is the damage/fracture mechanisms of immature bone in simulated scenarios.

The primary objective for experiments contained within this thesis was to examine the biomechanical behaviour of juvenile ribs in an experimental animal when under conditions that mimic both abusive squeezing and two-thumb CPR. A pig model was selected as a surrogate for human infants based on information within the literature.

5.1 Thorax Tests

The mechanical tests on the piglets were designed to record structural behaviour for the whole thorax when under two well constrained, but differing testing scenarios. Of specific interest was the load-displacement response of the thorax, along with detailed examination of any damage and/or fractures within the ribs as a result of the tests.

5.1.1 CPR

5.1.1.1 Individual Assessment of Thoraxes Receiving Simulated CPR

The load-displacement curves for pig 4 have a smooth non-linear appearance. This indicates that there was no catastrophic failure to the thorax or any of the elements within it during the test. This was further confirmed by the absence of any damage visible to the naked eye. Radiography revealed damage within the anterior region of right rib 6. This damage was assured with CT images, revealing damage spanning from the medial surface in to the the middle of the sternal end of right rib 6. No damage was noted to the costochondral joint of right rib 6. Possible damage to left rib 6 was identified, being located behind the costochondral interface, within the middle of the sternal end of the rib.

A discontinuity can be seen in the rising part of the force-displacement curve detailing the first compression for pig 5 (Figure 35). This could caused by damage to the thorax, or due to slippage in the rig. Damage was observed visually during the test as evidenced in the photographs of Figure 39. Damage being seen to left rib 4, the sternal end of left rib 5, as well as the sternal ends of right ribs 4 and 5.

Radiography failed to positively identify damage to the 5^{th} and 6^{th} rib pairs of pig 5, although it did show there was possibly damage to the anterior of left rib 5. This is in contrast to analysis of the X-ray CT for this specimen, which revealed bilateral fractures to the 5^{th} and 6^{th} rib pairs of piglet 5. Disruption to the ribs was shown to be in the form of fractures through the medial sternal ends, directly adjacent to the costochondral joints.

Although the damage seen in pig 5 was shown to be as a direct result of the simulated CPR testing, it is not possible to conclusively know when the damage occurred. It is likely that the damage was the result of the initial few compressions in which discontinuities were seen within the load-displacement curve. However, it may be the result of cumulative damage over the full series of compressions.

The load-displacement curve for the initial compression to the thorax of pig 6 rises in a smooth non-linear fashion until a displacement of 46 mm. After this point the force stays roughly constant with increasing displacement of the thorax. Subsequent compression curves have a smooth profile, making it likely that damage occurred within this initial

compression. Photographs taken during the testing show a costochondral failure to left rib 5. Multiple transverse fractures were also seen to the medial surface of the anterior region of right rib 4, exhibiting a damage pattern characteristic of a crushing or buckling type injury.

Radiography of pig 6 showed fractures to anterior regions of the left and right 5th ribs, with no other fractures seen. X-ray CT revealed further damage, with disturbance being seen to all anterior regions of rib pairs 5 and 6. This sternal end damage was consistent with that seen in pig 5, however the damage also extended into the costochondral joint interfaces.

5.1.1.2 Collective Assessment of Thoraxes Receiving Simulated CPR

Collective assessment of those thoraxes tested under CPR conditions reveals general trends regarding the behaviour of the rib cage and the typical damage exhibited.

The two-thumb CPR scenario on this infant swine model yielded maximum force values of 296.00-341.20 N (mean = 314.1 N). All three thoraxes tested showed a decrease in their mechanical resistance with increasing number of compressions. The drop off in the force value from the first to last compression was in the range of 142.2-238.9 N (mean = 177.87 N).

For this piglet model (≈ 7 kg) the mean average force values for 90 simulated CPR compressions were 121.77 N, 173.33 N, and 173.03 N, for thoraxes 4, 5, and 6 respectively. Worn and Jones (2007) calculated from data in an earlier study (Houri *et al*., 1997) that the compressive forces during manually delivered 2-thumb CPR on ≈ 10 kg immature swine was in the range of 223–251.6 N, showing that the forces applied were representative.

During the first compression of the thoraxes the unloading curve follows a different path to the loading curve, reaching zero force before returning to 0 mm displacement. Subsequent curves require greater displacement before a load response from the thorax is recorded. This is due to a permanent offset of the thorax. In addition progressively reduced loads were required to achieve the target thorax displacement, indicating permanent damage.

The force-displacement graphs for the first 5 compressions of all samples show that the initial compression has the largest hysteresis loop, and with successive compressions the hysteresis loops tighten. This indicates that the thoraxes experienced a reduction in anterior-posterior diameter as the tests progressed, and the elastic response of the system decreased.

This “flattening” of the thorax after CPR has also been observed in a study of CPR on adults using a pig surrogate (≈ 30 kg). Liao *et al*. (2010) reported anterior-posterior

diameter decreases of 25± 2 mm in their manual CPR group, and 20 ± 2 mm in their mechanically performed CPR.

The force-displacement curves for CPR in this pig model indicate that the entire thorax structure exhibits viscoelastic material behaviour. Viscoelastic materials exhibit both viscous and elastic characteristics when undergoing deformation. Repeated cyclic loading of viscoelastic materials causes a reduction in the force needed to displace the material with more cycles, ultimately tending towards an equilibrium value. This is due to the viscous part of the material response being dissipated, leaving the elastic portion as the only remaining response. This preconditioning response is evident in CPR experiments on the piglet thorax.

A further characteristic viscoelastic response can be seen after the pauses within the loading protocol. These pauses were to simulate the delivery of breaths during CPR. However, they reveal that the thorax experiences some viscoelastic recovery. This being exhibited as an increase in the force required for the compression following the pause in relation to the preceding compression. This is an important effect and implications when modelling CPR.

With regards to piglets tested with simulated CPR, neither radiography or CT gave any sign of fractures or damage being present within the posterior or lateral regions of the 5th and 6th rib pairs. Damage and fractures to the ribs of the simulated CPR piglets was exclusively seen in the anterior area of ribs, and was observed in all piglets. Both imaging modalities indicated anterior damage and fractures. However, CT was able to confirm its presence in nine of the twelve ribs analysed, as opposed to only three using radiography. Two of the piglets exhibited bilateral fractures to the 5th and 6th ribs, whilst the other piglet had damage to right 6th rib, and potentially to the left 6th rib.

The frequency of fractures in children following CPR has been described as almost negligible (Bedell and Fulton, 1986; Feldman and Brewer, 1984; Krischer *et al.*, 1987; Spevak *et al.*, 1994). A systematic review of 923 children undergoing CPR found anterior rib fractures in only three children (Maguire *et al*., 2006). Their review concluded that fractures due to CPR in children are a rare complication, and when they are seen they are likely to be anterior.

The findings of this study are in agreement with the literature that posterior and lateral rib fractures are not seen following CPR, with only anterior fractures seen. However, the relative frequency of anterior fractures is much higher than the literature would suggest. This increase in frequency of anterior fractures might be down to depressing the sternum

by exactly 1/3 the anterior-posterior diameter. Rescuers in a real life situation are not likely to go as deep due to fear of harming the infant.

X-ray CT of the anterior fractures resultant from the CPR scenario had a characteristic appearance. The fractures occurred to the medial portion of the bony collar found at the sternal end of the rib. The bone in this area was broken away appearing as a separate rim of bone adjacent to the costochondral junction. Severe damage to the anterior of the rib was exhibited by a breakdown along the interface of the costochondral junction.

5.1.1.3 Conclusions from Thoraxes Receiving Simulated CPR

The peak forces recorded during simulated abusive squeezing were 296.00-341.20 N (mean = 314.1 N). Force-displacement curves for all piglets showed viscoelastic preconditioning behaviour to the rib cage in response to repeated cyclical loading. This preconditioning of the thorax resulted in less force being required to achieve the target CPR compression depth as the test progressed and the rib cage became more compliant. A decrease in the anteroposterior diameter was also evident.

The thorax also exhibited other force-deformation behaviour consistent with viscoelastic recovery behaviour. Following pauses in compressions, the thorax had a stiffer response than the preceeding compression, before continuing to fail with successive compressions. This is an important observation in the context of modelling CPR.

The only rib fractures seen were exclusively within the anterior region of the rib. These had an appearance analogous to classic metaphyseal lesions of the longbones, displayed by a separated rim of bone adjacent to the costochondral end of the rib. In some cases these fractures extended to and along the line of the costochondral junction. These fractures were frequently under recorded with radiographic inspection, but were evident with X-ray CT.

5.1.2 Abuse

5.1.2.1 Individual Assessment of Abusively Squeezed Thoraxes

Pig 2

The force-displacement curve for pig 2 rises non-linearly, before then levelling until the required thorax displacement is reached. The force-displacement behaviour during the loading phase of the test shows that the thorax is maintaining its load-bearing capability whilst providing no evidence of catastrophic failure. This could be explained by permanent damage to the thorax, in which the ribs are plastically deformed, but crucially do not fracture through the main body of the rib bone. An alternative, but less likely explanation is that the thorax experienced slippage within the testing rig at this point, but this was not evident to the naked eye during testing.

During the holding phase the thorax shows a dramatic decrease in its ability to bear load. This is evidence of time-dependant damage and deformation to the thorax structure. The reaction force applied from the thorax to the plastic "thumbs" reaches zero well before the "thumbs" return to their original position in the unloading region of the curve. This permanent offset is evidence that enduring deformation of the thorax has taken place. This was visually apparent at the time of testing as there was an obvious costochondral failure at the sternal end of right rib 6, which remained displaced even after testing.

This damage to the anterior of right rib 5 was apparent when inspecting radiographs, whilst possible damage to the anterior regions of rib pair 6 was visible. X-ray CT provided a clearer view of the damage, making evident fractures to the anteriors of ribs right 5, left 6, and right 6. These fractures extended through the interior surface of sternal ends of the ribs towards the costochondral joints. The anterior costal cartilage of right rib 5 was clearly shown to be detached as a result of permanent damage to the costochondral joint.

Pig 3

Within the loading portion of the force-displacement graph for pig 3, the thorax shows a sudden decrease in its ability to bear load, characteristic of a catastrophic failure to an element within it. However, the structure as a whole is still able to bear load. Progressive failure within the thorax is then exhibited by the continued reduction in the level of force it is able to bear.

Throughout the holding phase, the thorax of pig 3 shows a continued reduction in its capacity to bear load. During the unloading of the rib cage a permanent reduction in its anterior-posterior diameter. This is evidenced by the reaction force exerted on the "thumbs" reaching zero well before they return to their original position.

The catastrophic damage noted in the loading portion of the force-displacement curve was confirmed by visual inspection, with a complete transverse fracture through the anterior of right rib 6 being seen.

Radiography identified anterior fracture to the fifth and sixth right ribs, whilst possible damage or fracture to the anterior of the sixth left rib was also seen. A possible lateral fracture was seen within the fifth left rib, whilst lateral fractures to the right fifth and left sixth ribs were positively identified. CT positively identified fractures within the anterior regions of the fifth and six rib pairs. The compound fracture to the sixth right rib was clearly evident, exhibited as a complete transverse fracture through the bone of the anterior region of the rib.

Inspection of the CT scan taken prior to mechanical testing showed possible damage to the sternal ends of the fifth rib pair. The presence of this damage before the test may well have contributed to the catastrophic failure of the sixth right rib. With the fifth rib pair having a reduced capacity to bear load, excessive force would have been placed on the sixth right rib. This would cause it to have been heavily loaded, likely resulting in failure. Compound fracture of the rib required a significantly higher amount of force, peaking at close to 500 N.

The displaced nature of the fracture to the sixth right rib would have compromised the overall integrity of the thorax. Without the load-bearing ability of this rib, the sternal elements of the thorax was significantly distorted. Ribs cephalad are likely to have been pulled downward by their sternal cartilage, causing them to be significantly distorted. This type of loading could well have been the cause of the lateral fractures seen to the 5th rib pair. The force-displacement curve for this specimen supports this theory of two-stage failure.

Pig 7

The force-displacement curve for pig 7 shows a non-linear rise with increasing gradient, until evidence it is beginning to level off just prior to reaching the target displacement depth. The reduction in the reaction force the thorax exerted on the “thumbs” during the holding phase shows that the thoraxes load-bearing capability reduces over time. This indicates a time dependent structural response.

The reaction force imparted on to the “thumbs” returns to zero well before they return to their initial position. This load offset indicates permanent deformation has taken place, with the thoraxes anterior-posterior diameter being reduced.

Discolouration caused by bleeding underneath the periosteum was seen to the anterolateral region of the fifth right rib in pig 7. This is interpreted as evidence of crushing damage, in which the medial surface of the rib is loaded in compression. The thorax of pig 7 also exhibits bleeds underneath the periosteum in the posterior regions of multiple ribs. Their appearance is consistent with transverse fractures, however they appear relatively distant from the posterior rib articulations with the spine.

Radiography of piglet 7 failed to show any rib fractures. However, X-ray CT was able to reveal fractures in anterior regions of right rib 5 and right rib 6. These fractures were shown to run between the internal medial side of the sternal end of the ribs, and the anterior end of the ribs. No disruption was seen to the interfaces of the costochondral joints in these ribs. A possible fracture or microdamage was seen within the bone of left rib 5, being contained to the anterior region of the rib, just back from costochondral junction.

Pig 8

The curve of the force-displacement reaction of the thorax of pig 8 continued to rise throughout the loading phase of the test. This shows it maintained its load-bearing capacity and did not exhibit any catastrophic failure. The curve does contain a slight discontinuity just prior to reaching the target displacement, this is evidence that the thorax experienced damage, or alternatively that it shifted within the rig.

The reaction force provided by the thorax of pig 8 to the “thumbs” had a significant drop during the holding phase. This drop-off shows a decrease in the load-bearing capability of the thorax, and is evidence of time-dependant behaviour within the elements of the thorax.

During unloading the reaction force from the thorax returns to zero well before the “thumbs” return to the original anterior-posterior diameter. This permanent offset strongly indicates permanent damage to the thorax.

From visual inspection the fifth right rib of pig 8 was heavily distorted during testing, unlike its counterpart on the left hand side. This apparent asymmetrical loading could be due to damage to the thorax or its becoming misaligned within the test rig during testing. Left ribs 7 and 8 had the appearance of transverse fractures through their posterior regions, but these did not disrupt the periosteum.

Inspection of radiographs did not reveal any rib fractures to the fifth and six ribs of pig 8. CT analysis showed damage to the anterior region of left rib 5, with a fracture running between the medial surface of the sternal end and the costochondral joint. Disruption to the costochondral joint can also be seen. On reinspection, damage could be seen in this area of the rib on the CT scan taken before mechanical testing. This could offer an explanation as

to the asymmetric response of the thorax during loading, the fifth right rib having to support a greater proportion of the load as its counterpart was already weakened. A possible fracture or microdamage was seen in the sixth right rib, just back from the costochondral joint. This was evident before and after testing, and although there was no disruption to the costochondral joint it is possible this damage further increased the load being born on right rib 5.

As only the fifth and sixth rib pairs underwent assessment with radiography and X-ray CT, the extent and nature of the posterior fractures to left ribs 7 and 8 was not analysed. This should be the subject of further analysis.

Pig 9

The force-displacement curve for pig 9 exhibits a smooth non-linear rising profile, before just beginning to level off when reaching the target displacement. Through the holding phase the thorax underwent a reduction in its ability to bear load. Whilst during the unloading phase the reaction force provided to the "thumbs" from the thorax reached zero well before the "thumbs" reached the original anterior-posterior diameter. This permanent offset is evidence of permanent damage and deformation to the thorax.

Visual inspection of pig 9 identified likely transverse fractures to the medial side of several ribs within their anterior regions. These were only identified due to the presence of blood underneath the periosteum, with the damage appearing to be consistent with a crushing injury.

Assessment with radiography failed to identify any damage or fractures to the ribs. X-ray CT showed fractures in the anterior regions of right ribs 5 and 6, extending between the medial surface of the the rib and the costochondral joint. There was no apparent damage to the interfaces between the ribs and costal cartilages at these costochondral joints. In addition, possible disruption was seen to the anterior region of left rib 5, but no damage to the costochondral joint was seen.

5.1.2.2 Collective Assessment of Abusively Squeezed Thoraxes

The thoraxes tested under abusive squeezing conditions reveal general trends regarding the rib cage behaviour and typical damage exhibited when assessed collectively.

Within this infant swine model the peak force values yielded during the abusive scenario ranged from 314.33-497.94 N (mean = 369.20 N). Four of the five thoraxes recorded this peak force only when 1/3 anterior-posterior diameter compression was reached. All five piglets exhibited a decrease in mechanical resistance during the holding phase. The range of this decrease was 177.6-254.37 N (mean = 225.38 N). This drop-off in reaction force in

response to applying a constant displacement is a classic stress relaxation phenomenon observed within viscoelastic materials. This would indicate that the thorax as a whole behaves viscoelastically due to the biological materials within it.

All thoraxes displayed permanent "flattening" in response to the anterior-posterior loading, evidenced by the permanent offset recorded during the unloading phase of the tests.

Fractures resultant from the abusive squeezing scenario identified with X-ray CT were principally located within the anterior of the thoraxes. Anterior fractures or damage was seen in all specimens. These anterior rib fractures have a very characteristic appearance displaying a separate rim of bone adjacent to the costochondral end. These have an appearance analogous to classic metaphyseal lesions of the longbones. When damage at the costochondral end of the rib is severe the cartilage and sternal end of the rib separate along the interface of the costochondral junction. This type of fracture has been noted in cases of child abuse by Ng and Hall (1998), they considered them to be consistent with a mechanism of injury that involves a compressive force on the sternum i.e. antero-posterior squeezing of the chest.

Generally no damage or fractures were seen in lateral or posterior areas of the ribs when viewed with CT and radiography. The lateral fractures identified with these characterisation techniques were contained exclusively within one specimen, and were likely subsequent to the catastrophic failure of one of the ribs within the thorax.

Visual inspection did reveal evidence of posterior fractures in two specimens, but these did not propagate beyond the medial surface of the rib and were therefore not apparent on X-ray CT inspection.

Several studies have stated that posterior rib fractures were the predominant abusive fracture (Al-mahroos *et al.*, 2011; Bulloch *et al.,* 2000; Feldman and Brewer, 1984; Smith *et al.*, 1980; Thomas, 1977). The abusive scenario within this study involved anteroposterior squeezing of the thorax with the spine being unsupported. These conditions are likely to facilitate the necessary mechanics to cause posterior rib fractures. However, there did not appear to be sufficient levering of the rib head over the transverse process, possible reasons for this are discussed later within this chapter.

5.1.2.3 Conclusions from Abusively Squeezed Thoraxes

The peak forces recorded during simulated abusive squeezing were 314.33-497.94 N (mean = 369.20 N). Force-displacement curves for all piglets showed a viscoelastic response to loading, with all the rib cages undergoing a "flattening" in the anteroposterior diameter in response to the testing.

Stress-relaxation behaviour characteristic of a viscoelastic structure was seen during the holding phase of the tests. The force to hold the thorax in this static configuration decreased over time.

Anterior rib fractures were principally seen, and were characterised by a separated rim of bone adjacent to the costochondral end. Their appearance was analogous to classic metaphyseal lesions of the longbones.

Severe trauma lead to separation of the rib and cartilage along the line of the costochondral junction. This type of costochondral junction fracture was frequently under recorded with radiographic inspection, but was evident with X-ray CT.

A significant observation was the absence of any posterior rib fractures within the abusive cohort. Explanation for reasons behind this are discussed in a critical review of the testing methods found at the end of this chapter.

5.1.3 Comparison between CPR and abusive squeezing scenarios

Both the CPR and abusive squeezing forces compressed the thoraxes by 1/3 their original anteroposterior diameter. Despite the distinct difference in the posterior support provided by the two testing scenarios, no significant difference in the force-displacement responses could be seen.

The anterior rib fractures reported for both scenarios had the same characteristic appearance when inspected with X-ray CT, specifically a separated rim of bone adjacent to the costochondral end. With no evidence of a difference in the observed damage it is not possible to distinguish whether fractures of this type are resultant from CPR or abusive squeezing when using X-ray CT. There may however be a difference within the associated soft tissue damage allowing for differentiation, but this was not investigated within this study.

It is likely that the anterior rib fractures in the two scenarios are caused by the same fracture mechanism. This is whereby the displacement of the sternum pulls on the sternal cartilages of the ribs causing the anterior ends of the ribs to be pulled inwards. This places the lateral portion of the costochondral joint under tension, and causes the medial portion to be put under compression.

The sternal end of the rib is surrounded by a bony collar which extends over the distal end of the cartilage. On the medial side of the rib, immediately adjacent to this bony collar is an area of bone that is more disorganised and of apparent lower density to the bone surrounding it. Compression on the medial portion of the bony collar causes the weaker area of bone to fracture and ultimately a rim of bone breaks away. This portion of bone includes the medial portion of the bony collar.

Whilst the lateral side of the costochondral junction is still maintained, any further compression acts to pull the rib medially. This movement is resisted by the curvature and strength of the rib as it tries to return to its natural position. The fracture then extends along the interface of the costochondral junction until it breaks down completely and the bowed rib springs back to its original position.

5.2 Rib Bone Mechanical Behaviour

5.2.1 Cross sectional pieces

Testing was performed on bone sections excised from the rib bones of mature and immature pigs. The objective of these tests was to characterise the difference in mechanical behaviour between the two. This data would also provide a suitable means of validation for image-based FE models replicating the experimentally recorded behaviour. Finally it allows assessment of the suitability of nanoindentation data recorded from bone for materials input into FE models.

Load-displacement responses were measured for compression tests of mature rib bone when dry, and immature bone when wet. Simple compression tests were chosen as testing conditions are well constrained; these can be accurately defined and replicated within FE models.

Testing the mature rib dry provided structural response data for a rib sample that was not subject to the effects of water. Characterisation of the tissue behaviour from nanoindentation tests performed dry was then directly applicable for FE models. Mature rib was tested first as it has a similar architecture to immature rib, but crucially it has a lower variability in tissue mineralisation. Tissue properties should therefore be more homogeneous and allow for simplification to isotropic material property behaviour within FE models.

The load-displacement curve for mature ribs recorded a yield force of close to 6 kN at a displacement of 0.175 mm. Whilst immature samples yielded at forces ranging from 0.55-0.9 kN at displacements of 0.06-0.1 mm.

The higher yield force recorded for the mature sample can be explained by the tissue having a higher degree of mineralisation and the fact it was dried out. Dehydration acts to increase the tissues stiffness, and has been shown to cause a 17% increase in the modulus of elasticity of bone (Evans and Lebow, 1951). The higher proportion of mineral within the bone tissue further increases its stiffness relative to the immature bone.

Care should be taken when directly comparing load-displacement curves for mature and immature samples due to variations in sample dimensions. The mature rib section had a slightly greater height and cross-section than those from immature ribs. Clearly the mature rib sample inherently has a greater volume of bone material, and as such will be able to withstand a greater load before yield.

Nanoindentation measurements resulted in average Young's modulus values of 11.64 GPa and 13.8 GPa for mature and immature rib bone tissue respectively. This result is somewhat surprising as it would be usual to expect the more mineralised tissue to have a greater stiffness. This could potentially be explained by the fact only one mature rib sample was used for nanoindentation. As such this average could be susceptible to sample and testing anomalies.

The modulus value recorded from nanoindentation for immature bone had been intended to be recorded on hydrated samples. However, the wet sample stage was out of commission at the time of testing. It would be reasonable to expect the recorded modulus would have been lower if immature rib samples were tested wet.

5.2.2 Individual rib tests

Tests of immature pig whole ribs were undertaken to characterise their structural behaviour when under loading representative of anteroposterior compression. The ribs had been dissected out from the pig thoraxes so the failure behaviour of an isolated rib could be compared to that of ribs within the thorax.

Characterisation of the ribs isolated from the biomechanical system of the thorax allows the constraints on the individual ribs to be more rigorously characterised. This affords better understanding of the fracture mechanics when the bone is in bending. This would aid in developing FE model of individual ribs, giving more confidence when modelling the mechanical behaviour of ribs in whole thorax.

The main finding of these tests was that the average load to failure of isolated immature ribs was 29.9 N. The force-displacement response was accurately recorded for each specimen, however details concerning the precise fracture response for specific specimens were inadvertently misplaced and lost. This prevented detailed analysis as to the cause of the load-displacement responses for specific ribs and their associated fracture.

Generally the ribs failed by buckling in the anterior region of the rib, along the medial surface. The rib bones did not fail catastrophically, and the periosteum remained intact preventing the displacement of any bone fragments. Radiography failed to show any discernible fracture line, and permanent deformation was only evident on lateral radiographs. However, X-ray CT has shown this area of the developing rib to have a more disorganised bone structure with a lower relative mineralisation to other surrounding parts of the rib. This increases the likelihood of the rib buckling in this region.

As the ribs did not have any associated sternal cartilage there was no opportunity for the ribs to exhibit costochondral junction failures; this was the principal failure mechanism seen in thorax tests. This highlights a significant difference between the failure mechanisms of isolated ribs and ribs within the thorax.

The constraints within the isolated rib compression tests only load the uppermost surface of the bone i.e. the lateral anterior end of the rib. Tests within the thorax have shown the medial portion of the costochondral junction tends to fail first when the thorax is anteroposteriorly compressed.

For a rib to fail by buckling within the thorax it would have to be loaded in such a way that the costochondral junction is not compromised, and the rib can be significantly anteroposteriorly compressed.

5.3 FE Modelling

Due to the lack of suitable human infant data it was determined that FE modelling of the human infant thorax would be almost impossible to validate. As an alternative approach the biomechanical behaviour of the thorax in a suitable surrogate was investigated. The purpose of the surrogate study was to increase understanding of the key issues involved when modelling the biomechanics of the thorax. The ultimate intention being to use this knowledge to help inform models of the infant human thorax in future research.

The ribs are of significance interest when investigating suspected child abuse cases, and as such these were chosen as the principal focus for FE modelling. A step-wise programme of modelling pig rib sections, before moving to models of isolated individual pigs ribs was undertaken. The modelling sought to replicate well defined physical experimental data in order to validate the methodology.

5.3.1 Rib cross sections

Mature Pig Bone

FE modelling of the mature rib section was conducted first as being fully mineralised tissue it had a more homogeneous and consistent behaviour than the developing immature bone of piglets. The mature bone structure had a comparable architecture to immature bone.

Load-displacement data for a compressive test on a section of mature bone has been reported in the results section, and was used for comparison with the FE analyses performed. Whilst these analyses were completed successfully, it was found that computational models did not produce results in line with the mechanical data when using material properties recorded from nanoindentation.

Mechanical and computational reaction force levels (2.84 kN and 6.80 kN respectively) taken at 1% strain showed a large disparity. The computationally derived value being 239.44% greater than the physically measured value. This disparity increases to 288% when considering strains of 2% (mechanical= 5.41 kN; computational = 15.6 kN).

Altering the material behaviour to a Young's modulus calculated from the mechanical data rather than nanoindentation data resulted in a closer approximation of the physical experiment. The disparity between physical and computational measurements was reduced to 7.4% for 1% strain, and 11.3% for 2% strain.

Theoretically if the geometry of the specimen and the material behaviour it consists of is suitably characterised, then computational and mechanical compression tests should match

closely. They will not always match exactly due to microcracking behaviour in the physical sample, but at the low strain rates considered here the material should be constrained to its elastic region.

Linear perfectly-elastic material behaviour was used as a simplification for FE models, however the recorded mechanical data is clearly not linear. This can provide some explanation for the increase in disparity from 1 to 2% strain measurements. In addition, an isotropic material model was used for the entire bone section. Therefore no differentiation was made between trabecular and cortical bone regions.

Bones mechanical behaviour is not simply isotropic, and the complicated architecture of the trabecular region may well mean that these areas were not in pure compression. This likely caused individual trabeculae to be loaded in bending or shear. Modelling these areas with an isotropic material property is likely to have contributed to the entire structure having a stiffer response than the physical reality.

Another cause for error could be that the cut faces of the sample were not perfectly flat and perpendicular to one another. Within the mechanical test certain areas of the bone surface would therefore have been loaded before others as the platen compressed the sample. Within the simulation the displacement is distributed uniformly across the top surface of the sample instantaneously. This would result in certain areas of the bone being put under strain in the model at a lower displacement than they did in reality. The net effect of this would be to raise the reaction force for a given strain within the model.

The external and internal micro-architecture of the mature rib section mesh was generated from downsampled image data. To investigate the effect of this a series of meshes of the mature rib were generated from image data of differing resolution.

Initial models were run using a mesh generated from X-ray CT data that had been downsampled to 20% of the original resolution. This was done to speed up computational times with regards to mesh generation and computer solving time. One consequence of downsampling the image data is that small architectural features and imperfections within the bone will be lost. Removal of these microstructural features will decrease the porosity within the mesh, ultimately making the structure behave stiffer than it actually is.

Downsampling of the the image data to only 25% of the original reduced the measured reaction force within the model to 6.24 kN at 1% strain, reducing the disparity to 220%. Due to computer performance constraints it was not possible to complete simulations for 1x1x1 meshed models generated from image data greater that 25% of the original.

An alternative “adaptive meshing” algorithm from Simpleware™ was used, which allows elements to be of different dimensions, rather than all the same size i.e. 1x1x1. Using adaptive meshing with a 0cc setting on 20% resolution image data produced a mesh with 60% more elements than the mesh produced with the +FE Grid meshing algorithm. The effect of this was to reduce the disparity with physical experimental data at 1% strain to 228%, a 10% reduction on the +FE Grid produced mesh.

Further 0cc adaptive meshes generated from up to 40% resolution image data were successfully solved. The divergence from the physical test was reduced down to 205.6% at 1% strain for the 40% resolution model.

Adaptive meshing at its coarsest setting (-50cc) allowed for models generated from 100% image data to be successfully solved, thus reducing the disparity to the mechanical data for 1% applied strain to 186.6% (2.84 kN vs 5.30 kN). The graph of reaction force against model resolution for the coarsest adaptive meshing shows two things. Firstly, that the apparent stiffness response of the models decreases with increasing model resolution. Secondly, that the change in reaction force begins to level off, indicating the model is reaching a state of precision.

Altering the material modulus within the 100% -50cc adaptively meshed model to 11 GPa has a clear effect on altering the stiffness of the model and increasing its accuracy. This indicates mechanical properties from nanoindentation are not appropriate for models at this length scale.

In discussions with experts in other material experiments, it is clear that the mechanical properties of highly heterogeneous materials are potentially subject to a size effect. In other words, the properties measured at one length scale may not be appropriate to another length scale. The results of this sensitivity analysis would appear to confirm this phenomenon when modelling sections of rib bone with a high level of porosity. Nanoindentation captures material behaviour at the nanoscale. Using this data directly in low resolution models where the microarchitecture is not as faithfully represented results in a much stiffer structural response. Nanoindentation data could potentially be adjusted to take this into account.

Immature Pig Bone

Results for FE modelling of immature pig bone sections gave reaction forces a factor of 10 higher than those recorded in mechanical testing. Modulus measured directly from nanoindentation was used as material behaviour input for the model. As the mesh was

generated from 10% resolution image data it is likely that a substantial size effect is imparted on the results of the model.

Nanoindentation was performed on dry immature bone, whilst the mechanical tests were performed on hydrated immature bone. Several studies have demonstrated the important effect hydration has on the Young's modulus of bone; dry bone having a much higher Young's modulus than wet bone (Evans and Lebow, 1951; Brear *et al*., 1990; Nyman *et al*., 2005; Akhtar *et al*., 2008). Dehydration was shown to cause a 17% increase in the modulus of elasticity of bone by Evans and Lebow (1951). It is likely that using nanoindentation data measured on dried bone caused the FE model to exhibit a stiffer response than the physical test on wet bone.

Developing bone has varying levels of mineralisation throughout its tissue structure, and hence varying mechanical strength. An average was taken from a number of nanoindentation tests across the bone and used as a single material behaviour input for the bone. This simplification potentially have altered the mechanical behaviour of the structure.

5.3.2 Isolated individual ribs

Immature pig ribs

Image data for the isolated immature pig rib had to be significantly downsampled to produce a mesh that could be solved using Abaqus on a workstation. This was due to the larger physical size of an isolated rib compared to a section of rib. Although the outside surface of the model had a high fidelity to the rib tested, the low resolution data did not capture the complex internal architecture. Therefore, small intricate features were lost, causing the bone tissue to become relatively stiffer in areas of cortical bone. Fine scale architectural within the cancellous bone regions was heavily decimated, causing a loss of connectivity in these areas. Loss of trabecular would have an effect on the mechanical behaviour of the rib as a whole.

As with the rib sections, nanoindentation is not appropriate for these low resolution models. In addition, the loading of isolated ribs is more complicated than for the rib sections, inducing bending and shear forces within the bone material. Clearly the use of an isotropic material is a significant simplification to the anisotropic behaviour bone exhibits. Further study and model development is needed before whole rib modelling would provide results accurately representative of physical experiments.

5.4 Critical discussion of testing methods

A discussion of possible confounding factors now follows. Where appropriate, reference is made to how these may effect what can be inferred from tests with regards to human infant thorax behaviour.

5.4.1 Use of surrogate animal

Experimentation was performed on pigs. This animal was chosen, as of the available surrogates, it offered the closest match to the human infant thorax. Selection of the pig was based solely on information from the literature. To the best of the authors knowledge, detailed information on the exact nature of the articulations within the pig thorax were not evident.

Although broadly similar, the posterior articulation of the ribs with the spine have now been shown to have key differences to humans. Specifically, the profile of pigs ribs in the region of the head and neck of the ribs exhibits significantly less curvature. This alters the mechanical advantage offered by levering over the transverse process of spine in pigs. This reduces the propensity for the ribs to fracture in this manner.

Testing on the piglets was performed post-mortem. Although procedures were followed to keep the ribs hydrated, there will inevitably be a change in the bone behaviour after death.

Liao *et al*. (2010) noted that the shape of the adult pig thorax is different from the human thorax in the transverse plane. The human being wider in the lateral diameter compared with the anteroposterior diameter, and the pig being the reverse. Despite choosing pigs believed to be of an age of weight similar to 6 month old infants, the shape of the piglet thorax in this test was more tear-dropped in shape. This difference has to be considered when compare the piglet thoraxes with those of infants.

5.4.2 Testing method

The rate of the mechanically delivered CPR compressions was much slower than that recommended for manual delivery of compressions. This was due to the limitations of the testing equipment. With a slower strain rate, all the component materials within the thorax have longer to deform, allowing a more viscous material response. This has implications as it may cause an alteration in fracture mechanics. The same is true for the abusive squeezing scenario.

The most commonly described form of abuse is shaken baby syndrome. Although this has a squeezing component, it also involves vigorous shaking. Shaking would cause a repetitive acceleration and deceleration trauma, which may afford impose more torsional forces on the ribs, increasing the likelihood of failure. Mechanically simulating shaking is

difficult to achieve, and accurate recording of forces is difficult when under these conditions.

The position where the ribs broke in abusive mechanical tests of full rib cages was different to where it had been predicted. This may be due to the gripping of the rib cage not being exactly right in the posterior region. However it does provide a well characterised mechanical test validate a FE model against. Gripping could be altered within FEA simulations to study its effect.

5.4.3 Radiography and CT fracture characterisation

It is difficult to conclusively compare the sensitivity of radiology and CT without skeletonising the piglets as an osteological control in order to determine the true number of bone fractures.

The ribs increase in curvature from upper to lowermost in the thorax, as a result the orientation of a CT scan cannot allow for an in toto observation of every single rib. Inspection of the full rib allows for identification of subtle discrepancies in their curvature, this is important particularly in immature bone as it may not fracture.

Assessment was not performed by a trained medical radiographer. This could have potentially reduced the detection of occult fractures.

Finally, only the 5th and 6th rib pairs were assessed using radiography and X-ray CT as these are the ribs directly attaching to the area of the sternum being depressed. Assessment of all the bones in the thorax may reveal more information on the distribution of fractures following CPR and abusive squeezing.

CHAPTER SIX

6 Conclusions

This thesis sought to better understand the biomechanical response of the immature piglet thorax as a means to interpreting rib fractures associated with child abuse. Of specific interest was whether two-thumb CPR has the potential to cause similar rib fractures to those caused by anteroposterior squeezing of the thorax, a key component of shaken baby syndrome.

Physical experimentation did not show any significant difference in the response of the piglet thorax between abusive and CPR scenarios. The nature and distribution of the rib injuries observed were remarkably similar in both scenarios. This study has shown anterior fractures of the ribs resultant from two-thumb CPR, challenging the long held belief that CPR cannot produce rib fractures. The costochondral junction fractures observed are consistent with those seen by Ng and Hall (1998) when investigating child abuse cases. This challenges the concept of the causality of rib fractures in relation to child abuse cases when a "CPR defence" is offered, and as such may have far-reaching medico-legal implications.

Costochondral junction failures are the result of significant anteroposterior compression to the thorax. Detection of this type of fracture amongst infants when CPR has not been administered should be seen as strong indication of abusive squeezing.

Anterior rib fractures in the region of the costochondral junction were difficult to observe and frequently under-reported when using only radiography. X-ray CT offered a significant improvement on the ability to detect this type of injury. This would offer further support to the routine use of X-ray CT in post-mortem examinations of infants where the cause of death is unknown. This has the potential to offer differential diagnoses, especially in SUDI cases.

There was an apparent absence of posterior rib fractures characteristic of abuse following the abusive squeezing scenario. This is principally down to the use of a swine surrogate. Although the posterior articulations of the rib and spinal elements in pigs and humans are principally the same, there are important differences between the two. The profile of the neck and head areas within ribs of pigs is less curved, with the attachment to the spine being at a shallower angle than in humans. The increased curvature within the posterior region of human ribs causes the ribs to become more bowed when anteroposteriorly loaded. This causing greater levering over the transverse processes of the spine and offers a superior mechanical advantage for stress to be placed on the rib. This difference in

posterior articulations means inferring posterior rib damage in human infants from tests performed on a swine model must be done so with caution.

However, despite this, it is the authors opinion that two-thumb CPR is unlikely to cause posterior rib fractures within human infants. This is due to the increased constraint placed upon the posterior of the ribs when CPR is performed on a flat surface. This prevents excessive levering of the ribs over the transverse processes of the spine, reducing the likelihood of fracture. Nonetheless this topic warrants further investigation in order to provide further evidence for this hypothesis.

Finite element modelling shows promise as a tool to elucidate the mechanisms of rib fractures in abused infants. However, this study has highlighted significant issues that need to be addressed before modelling of the human infant thorax can provide meaningful results.

Accurately representing the architecture and organisation of bone tissue within the developing rib is of paramount importance. Modelling of mature ribs has shown the sensitivity of results to the resolution of image data used when capturing bone architecture. Models generated from low-resolution data lack the fine architectural detail needed to accurately model physical experimental data. This is especially evident when using mechanical data directly measured from nanoindentation.

Care should be taken when using material data obtained from nanoindentation as an input to FE models. Nanoindentation captures mechanical data on the material properties of the bone tissue itself. Coarse models will lack fine scale architectural detail causing a dramatic over-prediction of the stiffness behaviour of the bone if nanoindentation data is not suitably adjusted.

FE modelling of immature rib bone proves to be challenging. This is a due to the developing nature of the bone tissue which leads to areas of the bone having differing levels of mineralisation. Areas of higher mineral content will have a higher stiffness, altering the behaviour of the bone in these regions. Use of a single material property for bone would therefore seem wholly inadequate.

Finally, the material behaviour of bone is different when measured dry and wet due to the the effect water has on the composite behaviour of bone. The presence of water causes the bone to exhibit greater viscoelastic mechanical behaviour, altering the modulus of the material. Nanoindentation of immature bone performed on dried samples is not appropriate as a material behaviour input when modelling immature bone sections that were tested hydrated.

7 References

Aerssens, J., Boonen, S., Lowet, G., & Dequeker, J. (1998). Interspecies differences in bone composition, density, and quality: potential implications for in vivo bone research. *Endocrinology*, *139*(2): 663-670.

Akhtar, R., Daymond, M. R., Almer, J. D., & Mummery, P. M. (2008). Elastic strains in antler trabecular bone determined by synchrotron X-ray diffraction. *Acta Biomaterialia*, *4*(6), 1677–87. doi:10.1016/j.actbio.2008.05.008

Al-mahroos, F., Al-Amer, E. A., Umesh, N. J., & Alekri, A. I. (2011). Pattern of Skeletal Injuries in child physical abuse. *Bahrain Medical Bulletin*, *33*(2), 1–11.

An, Y. H., Friedman, R. J. (1999). Animal selections in orthopaedic research. In: Animal Models in Orthopaedic Research (An YH, Friedman RJ, eds) CRC Press LLC, Boca Raton, FL, pp 39-57

Ascenzi, a, Baschieri, P., & Benvenuti, a. (1990). The bending properties of single osteons. *Journal of Biomechanics*, *23*(8), 763–71. Retrieved from http://www.ncbi.nlm.nih.gov/pubmed/2384488

Babout, L. (2006). X-Ray Tomography Imaging: a Necessary Tool for Materials Science. *Automatyka*, Tom 10, Zeszyt 3.

Barsness, K. A., Cha, E.-S., Bensard, D. D., Calkins, C. M., Partrick, D. A., Karrer, F. M., and Strain, J. D. (2003). The Positive Predictive Value of Rib Fractures as an Indicator of Nonaccidental Trauma in Children. *The Journal of Trauma- Injury, Infection, and Critical Care. 54*: 1107-1110.

Bedell, S. E., & Fulton, E. J. (1986). Unexpected findings and complications at autopsy after cardiopulmonary resuscitation (CPR). *Archives of Internal Medicine*, *146*(9), 1725–8.

Betz, P., & Liebhardt, E. (1994). Rib fractures in children - resuscitation or child abuse? *International Journal of Legal Medicine*. *106*: 215-218.

Boal, D.K. (2008). Child abuse. In: Slovis, T.L. (Ed.), Caffey's Pediatric Diagnostic Imaging, 11th edition Mosby Elsevier, Philadelphia, pp. 2816–2830.

Brear, K., Currey, J. D., Pond, C. M., & Ramsay, M. a. (1990). The mechanical properties of the dentine and cement of the tusk of the narwhal Monodon monoceros compared with those of other mineralized tissues. *Archives of Oral Biology*, *35*(8), 615–21. Retrieved from http://www.ncbi.nlm.nih.gov/pubmed/2256815

Bulloch, B., Schubert, C. J., Brophy, P. D., Johnson, N., Reed, M. H., & Shapiro, R. a. (2000). Cause and Clinical Characteristics of Rib Fractures in Infants. *Pediatrics*, *105*(4), e48–e48. doi:10.1542/peds.105.4.e48

Buser, D., Schenk, R. K., Steinemann, S., Fiorellini, J. P., Fox, C. H., Stich, H. (1991) Influence of surface characteristics on bone integration of titanium implants. A histomorphometric study in miniature pigs. J Biomed Mater Res 25: 889-902.

Bush, C. M., Jones, J. S., Cohle, S. D., & Johnson, H. (1996). Pediatric injuries from cardiopulmonary resuscitation. *Annals of Emergency Medicine*, *28*(1), 40–44. Retrieved from http://www.ncbi.nlm.nih.gov/pubmed/16651909

Cadzow, S. P. and Armstrong, K. L. (2000). Rib fractures in infants: Red alert! *Journal of Paediatrics and Child Health*. *36*: 322-326.

Callister, Jr., W. D. (2003). *Materials Science and Engineering – An Introduction*. John Wiley and Sons, New York; p. 717.

Canavese, F., Dimeglio, A., Stebel, M., Galeotti, M., Canavese, B., & Cavalli, F. (2013). Thoracic cage plasticity in prepubertal New Zealand white rabbits submitted to T1–T12 dorsal arthrodesis: computed tomography evaluation, echocardiographic assessment and cardio-pulmonary measurements. *European Spine Journal*, *22*(5), 1101–1112.

Carter, D. R., Mikic, B., Padian, K. (1998). Epigenetic mechanical factors in the evolution of long bone epiphyses. *Zoo. J. Linn. Soc*. *123*: 163–78

Carty, H. M. L. (1993). Fractures caused by child abuse. *The Journal of Bone and Joint Surgery. 75*(6): 849–857.

Cattaneo, C., Marinelli, E., Giancamillo, A. D., Giancamillo, M. D., Travetti, O., Vigano, L., Poppa, P., Porta, D., Gentilomo, A., and Grandi, M. (2006). Sensitivity of autopsy and radiological examination in detecting bone fractures in an animal model : Implications for the assessment of fatal child physical abuse. *Forensic Science International*. *164*: 131-137.

Centres for Disease Control and Prevention. (2009). (http://www.cdc.gov/growthcharts/who_charts.htm)

Contributors and Reviewers for the Neonatal Resuscitation Guidelines Pediatrics. (2000). International Guidelines for Neonatal Resuscitation: An Excerpt From the Guidelines 2000 for Cardiopulmonary Resuscitation and Emergency Cardiovascular Care: International Consensus on Science. Pediatrics. 106(3): e29.

Cook, R. D., Malkus, D. S., Plesha, M. E., Witt, R. J. (2001). *Concepts and applications of finite-element analysis*, 4 ed. New York: John Wiley and Sons.

Currey, J. D. (2006). *Bones: Structure and Mechanics*. Princeton University Press.

Daegling, D. J., Warren, M. W., Hotzman, J. L., & Self, C. J. (2008). Structural analysis of human rib fracture and implications for forensic interpretation. *Journal of Forensic Sciences*, *53*(6), 1301–7. doi:10.1111/j.1556-4029.2008.00876.x

David, R. (1988). Closed Chest Cardiac Massage in the Newborn Infant. *Pediatrics*. *81*(4)*:* 552-554.

Davis, G. R., Wong, F. S. L. (1996). X-ray microtomography of bone and teeth. *Physiological Measurement*. *17*: 121-146.

Dent, C.E., and Stamp, T.C.B. (1977). Vitamin D, Rickets, and Osteomalacia. In Avioli, L.V., and Krane, S.M. (Eds.), *Metabolic Bone Disease, Volume 1*. New York: Academic Press.

Diab, T., & Vashishth, D. (2007). Morphology, Localization and Accumulation of in vivo Microdamage in Human Cortical Bone. *Bone*, *40*(3), 612–618.

Dolinak, D. (2007). Rib fractures in infants due to cardiopulmonary resuscitation efforts. *The American Journal of Forensic Medicine and Pathology*, *28*(2), 107–110. doi:10.1097/01.paf.0000257392.36528.b8

Evans, F. G., & Lebow, M. (1951). Regional differences in some physical properties of the human femur. *Journal of Applied Physiology*, *3*, 363–372.

Feldkamp, L. A., Davis, L. C., Kress, J. W. (1984). Practical cone-beam algorithm. *Journal of the Optical Society of America A*. *1*: 612-619.

Feldman, K. W., Brewer, D. K. (1984). Child abuse, cardiopulmonary resuscitation, and rib fractures. *Pediatrics*;73(3): 339-342.

Fischer-Cripps, A. C. (2002) Nanoindentation. New York Springer Press.

Freeman, M. D., & Kohles, S. S. (2010). Applications and limitations of Forensic Biomechanics: a Bayesian perspective. *Journal of Forensic and Legal Medicine*, *17*(2), 67–77. doi:10.1016/j.jflm.2009.09.006

Gahagan, S., and Rimsza, M.E. (1991). Child Abuse or Osteogenesis Imperfecta: how can we tell? *Pediatrics,* 88:987-992.

Grosland, N. M., Shivanna, K. H., Magnotta, V. A., Kallermeyn, N. A., Devries, N. A., Tadepalli, S. C., Lisle, C. (2009). IA-FEMesh: An open-source, interactive, multiblock approach to anatomic finite element model development. *Computer methods and programs in biomedicine*. *9(4)*: 96–107.

Hammer, J, Eber, E. (2005) The pecularities of infant respiratory physiology. Prog Respir Res Basel Karger 33:2-7.

Hart, R. T. (1989). The finite-element method. In: Cowin, S.C., editor. *Bone mechanics*. Boca Raton, FL: CRC Press. P 53–74.

Hayes, W. C., Erickson, M. S., & Power, E. D. (2007). Forensic injury biomechanics. *Annual Review of Biomedical Engineering*, *9*, 55–86. doi:10.1146/annurev.bioeng.9.060906.151946

Hoke, R. S., & Chamberlain, D. (2004). Skeletal chest injuries secondary to cardiopulmonary resuscitation. *Resuscitation*. *63*(3): 327-38.

Hong, T. S., Reyes, J. A., Moineddin, R., Chiasson, D. A., Berdon, W. E., & Babyn, P. S. (2011). Value of postmortem thoracic CT over radiography in imaging of pediatric rib fractures. *Pediatric Radiology*, *41*(6), 736–748. doi:10.1007/s00247-010-1953-7

Houri, P. K., Frank, L. R., Menegazzi, J. J., & Taylor, R. (1997). A randomized, controlled trial of two-thumb vs two-finger chest compression in a swine infant model of cardiac arrest. *Prehospital Emergency Care*, *1*(2), 65–7.

Huelke, D. F., Nusholtz, G. S., & Kaiker, P. S. (1986). Use of quadruped models in thoraco-abdominal biomechanics research. J. Biomechanics, 19(12), 969–977.

Idris, A. H., Becker, L. B., Ornato, J. P., et al. Utstein-style guidelines for uniform reporting of laboratory CPR research. Resuscitation 1996;33:69-84.

Kak, A. C., Slaney, M. (1987). *Principles of computerized tomographic imaging*. New York: IEEE Press.

Kemp, A. M., Dunstan, F., Harrison, S., Morris, S., Mann, M., Rolfe, K., … Maguire, S. (2008). Patterns of skeletal fractures in child abuse: systematic review. *British Medical Journal*, *337*. doi:10.1136/bmj.a1518

Kennedy, H. (Ed.). (2004). Sudden unexpected death in infancy. A multi-agency protocol for care and investigation. *The report of a working group convened by The Royal College of Pathologists and The Royal College of Paediatrics and Child Health*. London.

Key, L.L. Jr. and Ries, W.L. (2002). Osteopetrosis. In Bilezikian, J.P., Raisz, L.G., and Rodan, G.A (Eds.), *Principles of Bone Biology, vol. 2.* (pp 1217-1227). California: Academic Press.

Khurana, J.S., and Fitzpatrick, L.A. (2009). Osteoperosis and Metabolic Bone Disease. In Khurana, J.A. (Ed.) *Bone Pathology,* 2nd Edition. (pp 217-237) London: Human Press.

Kieser, J. A., Tahere, J., Agnew, K., Kieser, D., Duncan, W., Swain, M. V., et al. (2011). Morphoscopic analysis of experimentally produced bony wounds from low- velocity ballistic impact. Forensic Sci Med Pathol;7:322–32

Kleinman, P. K. (1990). Review Article: Diagnostic Imaging in Infant Abuse. *American Journal of Roentgenology. 155*: 703–712.

Kleinman, P. K. (1998). Diagnostic Imaging of Child Abuse. Second Edition. Mosby.

Kleinman, P. K., Blackbourne, B. D., Marks, S. C., Karellas, A., Belanger, P. L. (1989). Radiologic contribution to the investigation and prosecution of cases of fatal infant abuse. *The New England Journal of Medicine*. *320*: 507–11.

Kleinman, P. K., Marks, S. C., Adams, V. I., & Blackbourne, B. D. (1988). Factors affecting visualization of posterior rib fractures in abused infants. *American Journal of Roentgenology. 150*(3): 635–8.

Kleinman, P. K., Marks Jr., S. C., Richmond, J. M., & Blackbourne, B. D. (1995). Inflicted Skeletal Injury : A Postmortem Radiologic-Histopathologic Study in 31 Infants. *American Journal of Roentgenology. 165:* 647–650.

Kleinman, P. K., Marks, S. C., Spevak, M. R., & Richmond, J. M. (1992). Fractures of the Rib Head in Abused Infants. *Radiology*, *185*(1), 119–123.

Kleinman, P. K., & Schlesinger, A. E. (1997). Mechanical factors associated with posterior rib fractures: laboratory and case studies. *Pediatric Radiology*, *27*(1), 87–91. Retrieved from http://www.ncbi.nlm.nih.gov/pubmed/r8995179

Krischer, J. P., Fine, E. G., Davis, J. H., & Nagel, E. L. (1987). Complications of cardiac resuscitation. *Chest*, *92*, 287–291.

Leventhal, J. M., Thomas, S. A., Rosenfield, N. S., Markowitz, R. I. (1993). Fractures in young children: distinguishing child abuse from unintentional injuries. *American Journal of Diseases of Children*. *147*: 87–92.

Liao, Q., Sjöberg, T., Paskevicius, A., Wohlfart, B., & Steen, S. (2010). Manual versus mechanical cardiopulmonary resuscitation. An experimental study in pigs. *BMC Cardiovascular Disorders*, *10*(1), 53. doi:10.1186/1471-2261-10-53

Linde, F., & Sorensen, H. C. F. (1993). Technical note: The effect of different storage methods on the mechanical properties of trabecular bone. *Journal of Biomechanics*. *26*(10): 1249-1252.

Lonergan, G.J., Baker, A.M., Morey, M.K., Boos, S.C. (2003). From the archives of the AFIP. Child abuse: radiologic–pathologic correlation. Radiographics 4, 811–845

Lynn, K. S., Fairgrieve, S. I. (2009). Macroscopic analysis of axe and hatchet trauma in fleshed and defleshed mammalian long bones. J Forensic Sci; 54:786–97.

Maguire, S. (2010). Which injuries may indicate child abuse? *Archives of disease in childhood. Education and practice edition*. *95* (6): 170-177.

Maguire, S., Mann, M., John, N., Ellaway, B., Sibert, J. R., & Kemp, A. M. (2006). Does cardiopulmonary resuscitation cause rib fractures in children? A systematic review. *Child Abuse & Neglect*, *30*(7), 739–51. doi:10.1016/j.chiabu.2005.12.007

Malone, S. A. (1986). Rib response and breakage due to anteroposterior loads. *Medical and Biological Engineering and Computing*, *24*(6), 569–576. doi:10.1007/BF02446258

Marrow, T. J., Buffiere, J.-Y., Withers, P. J., Johnson, G., Engelberg, D. (2004). High resolution X-ray tomography of short fatigue crack nucleation in austempered ductile cast iron. *International Journal of Fatigue*. *26*: 717–725.

Martin, R. B. and Burr, D. B. (1989) Structure, Function and Adaptation of Compact Bone. Raven Press, New York.

Matshes, E. W., & Lew, E. O. (2010). Do resuscitation-related injuries kill infants and children? *The American Journal of Forensic Medicine and Pathology*, *31*(2), 178–85. doi:10.1097/PAF.0b013e3181df62ee

Mcgraw, E. P., Pless, J. E., Pennington, D. J., & White, S. J. (2002). Unexpected Death in Neonates , Infants , and Children : Should Imaging Be Routine ? *Pediatric Radiology*, (June), 1517–1521.

Menegazzi, J. J., Auble, T. E., Nicklas, K. A., Hosack, G. M., Rack, L., & Goode, J. S. (1993). Two-thumb versus two-finger chest compression during CRP in a swine infant model of cardiac arrest. *Annals of emergency medicine*. *22*(2): 240-243.

Merten, D. F., Radkowski, M. A., Leonidas, J. C. (1983). The abused child: A radiological reappraisal. *Radiology. 146*: 377–81.

Morgan, E. F., Barnes, G. L., Einhorn, T. A. (2008). Chapter 1 - The Bone Organ System: Form and Function, In: Robert Marcus, David Feldman, Dorothy A. Nelson and Clifford J. Rosen, Editor(s), Osteoporosis (Third Edition), Academic Press, San Diego. p3-25. ISBN 9780123705440

Mosekilde, L., Kragstrup, J., Richards, A. (1987) Compressive strength, ash weight, and volume of vertebral trabecular bone in experimental fluorosis in pigs. Calcif Tissue Int 40: 318-322.

Nayak, K., Spencer, N., Shenoy, M., Rubithon, J., Coad, N., and Logan, S. (2006). How useful is the presence of petechiae in distinguishing non-accidental from accidental injury? *Child Abuse Negl*. *30*(5): 549–55.

Ng, C. S., & Hall, C. M. (1998). Costochondral junction fractures and intra-abdominal trauma in non-accidental injury (child abuse). *Pediatric Radiology*, *28*(9), 671–6.

Nyman, J. S., Gorochow, L. E., Adam Horch, R., Uppuganti, S., Zein-Sabatto, A., Manhard, M. K., & Does, M. D. (2013). Partial removal of pore and loosely bound water by low-energy drying decreases cortical bone toughness in young and old donors. *Journal of the Mechanical Behavior of Biomedical Materials*, *22*, 136–45. doi:10.1016/j.jmbbm.2012.08.013

Ogden, J. A. (2000). *Skeletal Injury in the Child*. (3rd Ed.) New York: Springer.

Ojima, K., Matsumoto, H., Hayase, T., and Fukui, Y. (1994). An autopsy case of osteogenesis imperfecta initially suspected as child absue. *Forensic Science International,* 65: 97-104.

Oliver, W. C., & Pharr, G. M. (1992). An improved technique for determining hardness and elastic modulus using load and displacement sensing indentation experiments. *Journal of Materials Research*, *7*(6), 1564–1583.

Part 9: Pediatric Basic Life Support. (2000). *Circulation*, *102* (suppl 1), I–253–I–290. doi:10.1161/01.CIR.102.suppl_1.I-253

Plunkett, J. (2006). Resuscitation injuries complicating the interpretation of premortem trauma and natural disease in children. *Journal of Forensic Sciences*, *51*(1), 127–30. doi:10.1111/j.1556-4029.2005.00027.x

Rauch, F., Glorieux, F.H. (2004). "Osteogenesis imperfecta".Lancet 363 (9418): 1377–85.

Rayfield, E. J. (2004). Cranial mechanics and feeding in *Tyrannosaurus rex*. *Proc. R. Soc. London B*. *271*:1451–59.

Rayfield, E. J. (2005a). Aspects of comparative cranial mechanics in the theropod dinosaurs *Coelophysis*, *Allosaurus* and *Tyrannosaurus*. *Zoo. J. Linn. Soc. 144*: 309–16.

Rayfield, E. J. (2007). Finite Element Analysis and Understanding the Biomechanics and Evolution of Living and Fossil Organisms. *Annu. Rev. Earth Planet. Sci. 35*: 541–76.

Reece, R.M., (1993). Child Abuse: Medical Diagnosis and Management. Lea & Febiger, Philadelphia.

Reece, R.M., (2002). What the literature tells us about rib fractures in infancy. In: National Conference on Shaken Baby Syndrome, SBS Quarterly, Fall

Rendas, a, Branthwaite, M., & Reid, L. (1978). Growth of pulmonary circulation in normal pig--structural analysis and cardiopulmonary function. *Journal of Applied Physiology: Respiratory, Environmental and Exercise Physiology*, *45*(5), 806–17. Retrieved from http://www.ncbi.nlm.nih.gov/pubmed/730578

Renton, J., Kincaid, S., & Ehrlich, P. F. (2003). Should helical CT scanning of the thoracic cavity replace the conventional chest x-ray as a primary assessment tool in pediatric trauma? An efficacy and cost analysis. *Journal of Pediatric Surgery*, *38*(5), 793–7. doi:10.1016/jpsu.2003.50169

Reyes, J. a, Somers, G. R., Taylor, G. P., & Chiasson, D. a. (2011). Increased incidence of CPR-related rib fractures in infants--is it related to changes in CPR technique? *Resuscitation*, *82*(5), 545–8. doi:10.1016/j.resuscitation.2010.12.024

Richardson, L. F. (1910). The approximate arithmetical solution by finite differences of physical problems. *Trans*. *R*. *Soc*. *London A*. *210*: 307–57.

Richmond, B., Wright, B., Grosse, I., Dechow, P., Ross, C., Spencer, M. and Strait, D. (2005). Finite Element Analysis in Functional Morphology. *Anat*. *Rec*. *Prt*. *A. 283A*: 259-274.

Ritchie, R. O., Buehler, M. J., & Hansma, P. (2009). Plasticity and toughness in bone. *Physics Today*, 62: 41-47.

Saternus, K. S., Oehmichen, M. (1985). Kardiopulmonale Reanimation bei Säuglingen (cardiopulmonary resuscitation in infants). Der Notarzt. *1*: 77-81.

Scheuer, L., Black, S. (2000) Development Juvenile Osteology. Academic Press. ISBN: 978-0-12-624000-9

Schultz, A. B., Benson, D. R., and Hirsch, C. (1974). Force-deformation properties of human ribs. *J. Biomechanics*, *7*, 303–309.

Smith, F. W., Gilday, D. L., Ash, J. M., & Green, M. D. (1980). Unsuspected costo-vertebral fractures demonstrated by bone scanning in the child abuse syndrome. *Pediatric Radiology*, *10*(2), 103–106. doi:10.1007/BF01001749

Spevak, M. R., Kleinman, P. K., Belanger, P. L., Primack, C., & Richmond, J. M. (1994). Cardiopulmonary Resuscitation and Rib Fractures in Infants: A Postmortem Radiologic-Pathologic Study. *Journal of the American Medical Association*, *272*(8), 617–618.

Steen, S., Liao, Q., Pierre, L., Paskevicius, A., & Sjöberg, T. (2002). Evaluation of LUCAS, a new device for automatic mechanical compression and active decompression resuscitation. Resuscitation, 55, 285–299.

Sun, C., Huang, G., Christensen, F. B., Dalstra, M., Overgaard, S., Bunger, C. (1999) Mechanical and histological analysis of bone-pedicle screw interface in vivo: titanium versus stainless steel. Chin Med J (Engl) 112: 456-460.

Swanson, K. S., Mazur, M. J., Vashisht, K., Rund, L. A., Beever, J. E., Counter, C. M., & Schook, L. B. (2004). Experimental Biology and Medicine Genomics and Clinical Medicine : Rationale for Creating and Effectively Evaluating Animal Models.

Teo, J. C. M., Si-Hoe, K. M., Keh, J. E. L., & Teoh, S. H. (2006). Relationship between CT intensity, micro-architecture and mechanical properties of porcine vertebral cancellous bone. *Clinical Biomechanics*, *21*(3), 235–44. doi:10.1016/j.clinbiomech.2005.11.001

Thomas, P. S. (1977). Rib fracture in infancy. *Annales de Radiologie*, *20*(1), 115–122.

Thorwarth, M., Schultze-Mosgau, S., Kessler, P., Wiltfang, J., Schlegel, K. A. (2005) Bone regeneration in osseous defects using a resorbable nanoparticular hydroxyapatite. J Oral Maxillofac Surg 63: 1626-1633.

Turner, C. H., & Burr, D. B. (1993). Basic Biomechanical Measurements of Bone : A Tutorial. *Bone*, *14*, 595–608.

Turner, M. J., Clough, R. W., Martin, H. C., Topp, L. J. (1956). Stiffness and deflection analysis of complex structures. *J*. *Aero*. *Sci*. *23*: 805–23.

van Rietbergen, B., Weinans, H., Huiskes, R., Odgaard, A. (1995). A new method to determine trabecular bone elastic properties and loading using micromechanical finite element models. *J. Biomech*. *28*: 69–81.

Weber, M. a, Risdon, R. A., Offiah, A. C., Malone, M., & Sebire, N. J. (2009). Rib fractures identified at post-mortem examination in sudden unexpected deaths in infancy (SUDI). *Forensic Science International*, *189*(1-3), 75–81. doi:10.1016/j.forsciint.2009.04.015

Weller, S. E. (2012). *Structural Analysis of Porcine Rib Fractures*. (Masters Thesis), University of Otago.

Wootton-Gorges, S. L., Stein-Wexler, R., Walton, J. W., Rosas, A. J., Coulter, K. P., & Rogers, K. K. (2008). Comparison of computed tomography and chest radiography in the detection of rib fractures in abused infants. *Child Abuse & Neglect*, *32*(6), 659–663. doi:10.1016/j.chiabu.2007.06.011

Worlock, P., Stower, M., Barbor, P. (1986). Patterns of Fractures in Accidental and Non-accidental Injury in Children: A Comparative Study. *British Medical Journal (Clinical Research Edition)*. *293* (6539): 100-2.

Worn, M. J., & Jones, M. D. (2007). Rib fractures in infancy: establishing the mechanisms of cause from the injuries--a literature review. *Medicine, Science, and the Law*, *47*(3), 200–12.

Yaszemski, M. J., Payne, R. G., Hayes, W. C., Langer, R., & Mikos, a G. (1996). Evolution of bone transplantation: molecular, cellular and tissue strategies to engineer human bone. *Biomaterials*, *17*(2), 175–85. Retrieved from http://www.ncbi.nlm.nih.gov/pubmed/8624394

Zienkiewicz, O. C., Taylor, R. L., Zhu, J. Z. (2005). *The Finite Element Method: Its Basis and Fundamentals*. 6th Ed. Amsterdam: Elsevier Butterworth-Heinemann.